Modélisation des propriétés physico-chimiques des aérosols atmosphériques à haute altitude

Aurelia Lupascu

No d'Ordre: D.U. 2325

UNIVERSITE BLAISE PASCAL

GRADUATE SCHOOL OF FUNDAMENTAL SCIENCES

No 738

PhD. Thesis

in partial fulfillment of the requirements for the degree of
Doctor of Philosophy

Speciality: Atmospheric Physics

Submitted and presented by

Aurelia Lupascu

Modeling of physico-chemical properties of atmospheric aerosols at high altitude

defended the 18th of December 2012

PhD. Committee:

Chair: Dr. Nadine CHAUMERLIAC, LaMP CNRS, Clermont-Ferrand
PhD. Examinators: Dr. Matthias BEEKMAN, LISA CNRS, Paris
Pr. Dr. Sabina STEFAN, University of Bucharest, Bucharest
PhD. Reviewers: Dr. Edouard DEBRY, INERIS, Paris
PhD. Supervisors: Dr. Karine SELLEGRI, LaMP CNRS, Clermont-Ferrand
Pr. Dr. Wolfram WOBROCK, LaMP CNRS, Clermont-Ferrand

Acknowledgments

I am happy to take this opportunity to acknowledge and thank all those people who have helped me to reach this stage of my career. I would like to firstly thank my advisors Pr. Dr. Wolfram Wobrock and Dr. Karine Sellegri for allowing me to pursue this research and for being wonderful advisors. With their extreme patience, broad knowledge and understanding, I have learned many things about the aerosols during these three years. They led me into this exciting field, and always has been there to provide guidance and professional support. I greatly appreciate their enthusiasm and encouragement along my doctoral research.

I would like to extend my sincere thanks to my committee members: Dr. Nadine Chaumerliac, Dr. Matthias Beekmann, Pr. Dr. Sabina Stefan, and Dr. Edouard Debry for their support and interest in my research.

Many thanks to Dr. Wolfram Wobrock and Dr. Andrea Flossmann for giving me the opportunity to work in the Laboratoire de Meteorologie Physique during these three years. I am very thankful to Florence Holop and Cecile Yvetot for their assistance with the necessary paperwork.

It has been a pleasure to have worked with Cecile, Fred (they adopted me in my first day in France), Carole, Christelle, Yoann, Laurent, Evelyn, Maxime and all PhD students during my stage. Working at LaMP was very enjoyable and a very pleasant experience and all the group members treating me like one of them from the beginning, I always felt part of the group. For those who participate to the unforgettable lunch and coffee breaks very special thanks. I am grateful to Carole, Yoann, Laurent and Christelle for help me with some of the thesis arrangements.

I appreciate a lot the wonderful moments spent in France with my friends Rahimeh, Nathalie, Jean-Francois, and those who participated to the French classes.

Alphabetically, for their constant support I am grateful to Claudiu, Mirela, and Rodica.

I would specially thank Veronica for her encouragement and help during the darkness before dawn. Without her encouragement I couldn’t finish my thesis draft under the double pressure of health issues and painful writing.

Last but not the least, I would like to express my utmost thank to my family for always being on my side. Their unconditional love and support are really immeasurable and fathomless not only during my doctoral study but also throughout my whole life.

Introduction

Aerosol particles are ubiquitous in the Earth's atmosphere. All liquid or solid particles suspended in air are defined as aerosol particles. Atmospheric aerosol particles extend over a very large range of sizes: from sub-nanometer sized clusters of molecules up to millimeter-sized dust particles. The atmospheric aerosol consists of particles from a large number of sources, both natural and anthropogenic.

Although a minor constituent of the atmosphere, the aerosol particles are linked to visibility reduction, adverse health effects and heat balance of the Earth. Particles in the atmosphere scatter and absorb solar as well as terrestrial radiation. Therefore they influence the global radiation budget directly. Besides their direct effect on the radiation budget (Bellouin et al., 2005, Yu, et al., 2006), a large fraction of the atmospheric aerosol particles acts as cloud condensation nuclei (CCN). When clouds form in the atmosphere, water condenses on the available cloud condensation nuclei. A changing in the number concentration of CCN modifies the number concentration and the size of the cloud droplets. Aerosol particles can also indirectly affect the heterogeneous chemistry of reactive greenhouse gases. While the combined global radiative forcing due to increases in major greenhouse gases (CO_2, CH_4 and N_2O) is +2.3 Wm^{-2}, anthropogenic contribution to aerosol particles (primarily sulfate, organic carbon and nitrate) produce a cooling effect, with a total direct radiative forcing of −0.5 Wm^{-2} and an indirect cloud albedo forcing of −0.7 Wm^{-2} (IPCC, 2007). Moreover, airborne particles play an important role in the spreading of biological organisms, reproductive materials, and pathogens (pollen, bacteria, spores, viruses, etc.), and they can cause or enhance respiratory, cardiovascular, infectious, and allergic diseases (Berstein et al, 2004, Davila et al, 2007, Shiraiwa et al., 2012).

The characteristics of an aerosol population (total number concentration, size distribution, chemical composition etc.) depend on the location: urban or remote rural; continental or marine; boundary layer or higher up; as well as on the season and even the time of the day (e.g. Poschl, 2005).

Based on their source, aerosol can be divided into two groups: primary aerosols which are directly released into the atmosphere such as wave breaking and dust emissions and all type of anthropogenic emissions; and secondary aerosols which are formed in the atmosphere from the gaseous phase: precursor gases become particles by nucleation and condensation (Seinfeld and Pandis, 1998). In the latter case, chemical reactions can play an important role by turning high volatility gases into species with low vapor pressure and thus high saturation ratio, i.e. creating favorable conditions for particulate matter formation.

Nucleation is occurring when condensable vapors create stable clusters of the sub-nanometer size. The clusters grow into stable new particles with further condensational growth. This latter process is called new particle formation, and it is favored when the condensational surface represented by preexisting particles is low, while condensable precursor gases concentrations are high.

The atmospheric new particle formation processes may be relevant because the freshly formed particles can grow into sizes where they act as CCN and therefore influence cloud properties and climate (Pirjola et al., 1999, Dusek et al., 2006, Spracklen et al. 2006, Merikanto et al, 2009).

Nucleation and new particle formation events have been observed in many environments.

However, information on the vertical extends of nucleation and new particle formation is rare as only few observational points exist and the measurement techniques are difficult to apply during airborne studies.

Chemical transport models can be used to ameliorate our understanding of the governing processes for aerosol formation. Modeling studies are complementary to laboratory and field campaigns for developing a complete picture of the atmospheric transformation of a species. For example, modeling work can highlight a deficiency in current understanding when the modeled and observed concentrations do not agree, and laboratory experiments can identify a new species or formation pathway to include in a model. A well developed model can then be used to diagnose how projected changes in emissions or climate may influence pollutant concentrations.

Atmospheric models constitute an important tool for simulations of transport and transformation of aerosols and gases and thus to improve our knowledge about aerosol particles primary and secondary sources of aerosol particles. The ability of chemistry-transport models (CTMs) to

accurately simulate aerosols at high altitude stations is still to be demonstrated due to reduced number of monitoring sites and difficulties to take into account the complexity of the air parcels dynamics in mountainous areas. Continuous aerosol measurements have mostly been carried out at low altitudes. This is reasonable because the stations are easier to be built and operated there. However, low-altitude measurements are easily affected by local aerosol sources and small-scale meteorological patterns in boundary layer. Regional and large-scale concentration levels of aerosol particles can therefore be observed more reliably in measurements conducted at high altitudes. Observations from high-altitude stations have a special significance as the aerosols in this region are far from potential sources and are more representative of background conditions and a greater spatial extent (Asmi, 2011).

The goal of this thesis is to investigate the capability of the regional air-quality model CHIMERE to reproduce the mass and number concentrations and temporal evolution of the aerosols particles at high altitudes (as for example Puy de Dome research station), and in particular, evaluate its capacity to simulate the formation of new particles due to nucleation. Specifically, this thesis aims to address the following questions:

-What is the impact of a fine resolution topographical database on the accuracy of simulation of dynamical parameters at high altitude?
-What is the impact of the use of different emissions databases in the accuracy of gas-phase and aerosol concentration predictions?
-What is the most adequate nucleation parameterization scheme for simulating new particle formation at high altitude?
-What is the influence of the choice of the primary particle size distribution on the prediction of new particle formation?

The observed data used to compare with the modeling results are from the Puy de Dome research station (45º 46' 15" N; 2º 57' 50" E, 1465 m a.s.l.). This station provides continuous measurements of the aerosol particle size distribution, aerosol hygroscopicity, aerosol particle nucleation in the nano-meter range. The work of Boulon et al., 2011 presents an analysis of the occurrence of nucleation at two different rural altitude sites, at the Puy de Dome station and at

the surface station Opme (660 m asl) located around 12 km South-Easth of the Puy de Dome station. They showed that the frequency of nucleation events was higher at Puy de Dome site (97.5% of events detected) in comparison with lower station of Opme (56% of events detected) leading to the conclusion that the nucleation process is clearly enhanced at the high altitude station and the new particle formation process usually occurs in elevated altitudes.
Additionally, during intensive field campaigns, on-line chemical analysis of the aerosol is available with high time resolution. We propose here to confront the regional air-quality model CHIMERE coupled with the meteorological model WRF both with high altitude measurements performed at the Puy de Dome station and with ground based measurements made inside the urban boundary layer of Clermont-Ferrand.

This thesis is structured as follows: the first chapter will provide an overview of the relevant aspects of aerosol in the atmosphere and previous modeling approaches. Chapter 2 describes our modeling system and introduces the various parts of the computer models we used. Chapter 3 presents the evaluation of both the meteorological model and the air quality models using for the meteorological model two different topographical inputs and for the air quality model two different emission databases. Results of the simulations using different nucleation schemes are presented and discussed in chapter 4. Three nucleation parameterizations are tested using the CHIMERE model. Weak, moderate, and strong nucleation events of aerosol particles together with days without nucleation from observation performed at Puy de Dome research station are selected for the evaluation. The ability of the different theories to reproduce the occurrence or lack of a nucleation event is evaluated. Subsequently, these results are summarized and implications of our findings discussed. A brief outlook on the direction of future research is given in the last chapter.

Chapter 1. General introduction: the dynamics and the dispersion of aerosols at local scale

This chapter is dedicated to presenting fundamental information on aerosols and their properties, and the description of the general principles of numerical modeling of the particles. First, the various constituents of aerosol and their microphysical properties are described. In the last section of this introductory chapter, we give a summary of current knowledge and major advances in aerosol modeling. Different approaches for the inclusion of particles in the models are described based on a literature review.

Aerosols play a key role in many fields and on many scales of atmospheric and climate science, ranging from the nanometer scale of molecular interactions and chemical reactions to the global scale of the climate system. The recently published Fourth Assessment Report (AR4) of the United Nations Intergovernmental Panel on Climate Change (IPCC) states that the full range of processes leading to modification of cloud properties by aerosols is not well understood and the magnitudes of associated indirect radiative effects are poorly determined (Solomon et al., 2007).

The tropospheric aerosol consists of water, inorganic acids and salts, and many different organic compounds originating from natural and anthropogenic processes. Numerous individual organic compounds present in ambient aerosol samples have been identified (e.g. Mazurek et al., 1997; Pio et al., 2001; Tsapakis et al., 2002). These compounds consist mostly of different alkanes, acids, alcohols, aldehydes, ketones, nitrates and aromatic hydrocarbons. Thus, the tropospheric aerosol is, from a physicochemical point of view, an organic-inorganic mixture. Figure 1.1 shows a selection of important atmospheric topics and effects related to the composition and non-ideal thermodynamics of mixed organic-inorganic aerosol particles.

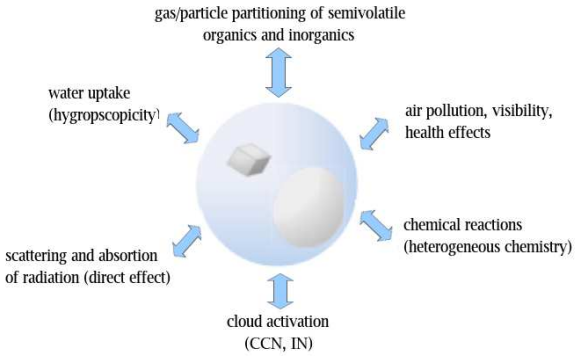

Figure 1.1. The thermodynamics of mixed aerosol and related effects

Tropospheric aerosols, especially the very fine particles originating from anthropogenic activities, have an impact on air quality and human health. In addition, scattering and absorption of solar and terrestrial radiation influence the visibility and the earth's radiative budget.

Numerical models of meteorology and air quality can play a role in characterizing the concentration and properties of aerosol. They are also useful tools to explore control strategies, provide short-term forecasts, test our understanding of the science, and explore new theories about air pollution science.

1.1. The atmospheric aerosols

The atmospheric aerosols are particles in suspension in the air. They represent the condensed phase in liquid and solid form. Many classifications are used to describe the aerosols phase: in function of their origin (natural or anthropogenic), of their nature (inorganic or organic), of their size (the number distribution). The aerosols size varies from one nanometer to a few tens of microns. The aerosols with superior size are not generally considered as particles in suspension because they can sediment under gravitational effect. The inferior limit corresponds to the smaller condensation nuclei measured until now. If more than 90% of particles in suspension have a diameter less than 0.1 μm, the mass majority is composed of particles having a superior diameter.

The term “atmospheric aerosols” encompasses a wide range of particle types having different compositions, sizes, shapes and optical properties. Aerosol loading, or amount in the atmosphere,

is usually quantified by mass concentration or by an optical measure, aerosol optical depth (AOD). Usually numerical models and in situ observations use mass concentration as the primary measure of aerosol loading (Remer et al., 2009).

Aerosols interact both directly and indirectly with the Earth's radiation budget and climate. As a direct effect, the aerosols scatter sunlight directly back into space. As an indirect effect, aerosols in the lower atmosphere can modify the size of cloud particles, changing how the clouds reflect and absorb sunlight, thereby affecting the Earth's energy budget.

Aerosols also can act as sites for chemical reactions to take place (heterogeneous chemistry). The most significant of these reactions are those that lead to the destruction of stratospheric ozone. During winter in the polar region, aerosols grow to form polar stratospheric clouds. The large surface areas of these cloud particles provide sites for chemical reactions to take place. These reactions lead to the formation of large amounts of reactive chlorine and, ultimately, to the destruction of ozone in the stratosphere. Evidence now exists that shows similar changes in stratospheric ozone concentrations occur after major volcanic eruptions, like Mt. Pinatubo in 1991, where tons of volcanic aerosols are blown into the atmosphere (http://www.nasa.gov/centers/langley/news/factsheets/Aerosols.html).

The radiative effects of aerosols affect the climate opposite to that of increasing concentrations of greenhouse gas emissions (which contribute to the global warming). The lifetime of aerosols, however, is much shorter, in general, than that of greenhouse gas emissions. Quantitatively, on a global scale, the radiative impacts of particles do not compensate the radiative impact of greenhouse gas emissions. However, locally, the concentrations of aerosols can be very important. The radiative effects can then have important consequences (IPCC, 2007). By increasing aerosol and cloud optical depth, anthropogenic emissions of aerosols and their precursors contribute to a reduction of solar radiation at the surface. As such, worsening air quality contributes to regional aerosol effects. The decline in solar radiation from 1961 to 1990 affects the partitioning between direct and diffuse solar radiation: Liepert and Tegen (2002) concluded that over Germany, both aerosol absorption and scattering must have declined from 1975 to 1990 in order to explain the simultaneously weakened aerosol forcing and increased direct/diffuse solar radiation ratio. The direct/diffuse solar radiation ratio over the USA also increased from 1975 to 1990, likely due to increases in absorbing aerosols. Increasing aerosol optical depth associated with scattering aerosols alone in otherwise clear skies produces a larger

fraction of diffuse radiation at the surface, which results in larger carbon assimilation into vegetation (and therefore greater transpiration) without a substantial reduction in the total surface solar radiation (Niyogi et al., 2004, IPCC, 2007).

The aerosols can significantly alter the chemical composition of the atmosphere (Faust, 2004). They can absorb semi-volatile species thus changing the kinetic equilibrium. Also the heterogeneous reactions can occur on the surface of aerosols. The particles then behave as a catalyst for the chemical reactions that affect the gas phase.

Finally, aerosols can have significant health impacts. The fine and ultrafine particles enter the respiratory system. Aerosols carry various chemical species, particularly organic species, which can cause inflammatory and/or allergenic reactions. The aerosols are, also correlated to certain cardiovascular diseases. Suspected are especially the ultrafine particles which can cross the respiratory mucosa and to be responsible for systemic effects, including blood coagulation and cardiovascular effects. These effects appear to be strongly dependent on the diameter of the particles and their chemical composition (WHO, 2000).

One of the greatest challenges in studying aerosol impact is the immense diversity, not only in particle size, composition, and origin, but also in spatial and temporal distribution. For most aerosols, whose primary source is emissions near the surface, concentrations are greatest in the atmospheric boundary layer, decreasing with altitude in the free troposphere. However, smoke from wildfires and volcanic effluent can be injected above the boundary layer, after injection, any type of aerosol can be lofted to higher elevation, this can extend their atmospheric lifetimes, increasing their impact spatially and climatically.

1.1.1. The sources

Atmospheric particles are produced by two distinctly different mechanisms: particulate emissions produce *primary* particles spanning a wide range of sizes, and gas-to-particle conversion creates nanometer-sized particles by atmospheric nucleation, or new material on all sizes by condensation, both process being called *secondary* production. These production mechanisms differ greatly in their spatial and temporal variations and the factors that control these variations. For example, particulate emissions occur almost universally close to the ground whereas nucleation occurs in the boundary layer (Kulmala et al., 2004) and in the upper

troposphere (Twohy et al., 2002; Benson et al., 2008). The increased aerosol concentrations are largely due to secondary particle production, i.e. homogeneous nucleation and subsequent growth from vapors.

An important part of the atmospheric aerosols mass have a natural primary origin. As an example of primary sources we can mention mainly the erosion of dust under the action of the wind, the formation of marine aerosols released by the burst at the surface of an ocean of bubbles air forms at the breaking waves, the volcanic eruptions or the biogenic aerosols made by the various activities of the planet.

The anthropogenic aerosols come principally from the road and the air traffic, and various industrial activities. However, we could also note all combustion processes such as fires, which had in the past disastrous health consequences, or the cigarettes smoke. The emission of volatile organic compounds (VOCs) of anthropogenic origin is a source of secondary aerosols. Indeed, these VOCs can be oxidized in the atmosphere giving rise to compounds whose saturated vapor pressure is low enough to form secondary aerosols by the transformation process gas/particle.

1.1.2. The size distribution and formation mechanism

The size of atmospheric particles varies from one nanometer to a few tens of microns and has an influence on their lifetime in the atmosphere that can vary from a couple of hours to several weeks. Moreover, the optical properties of aerosols, together with their effect on environment and health vary considerably as a size function. The size distribution can be represented in number, mass, volume or surface. The aerosol distribution is controlled by a complex system of physical processes. The experimental characterization of the spectral distribution proposed by Whitby (1976) highlights three principal modes (see Figure 1.2):

- *the nucleation mode* containing ultrafine particles having the diameter less than 0.1 micrometer, formed mainly by condensation of vapors during combustion processes at high temperatures or by homogeneous nucleation during cooling. These particles can then grow by coagulation between themselves or with larger particles and thus passing into the higher mode, which is the main loss in this mode. Although the largest number of airborne particles appear in the

nucleation mode, these particles give a small contribution to the total mass of particles because of their very small size.

- *the accumulation mode* contains particles with a diameter between 0.1 and 2 microns resulting from the coagulation of nucleation mode particles and condensation of vapors on existing particles whose size increases while they are in the range. This mode is a major contributor to the surface and the total mass of aerosols in the atmosphere. The accumulation mode is so called because the atmospheric removal processes are less efficient in this size range. These fine particles can remain in the atmosphere for days or weeks. Dry and wet depositions (precipitation scavenging) are the main processes by which these particles are eventually removed from the atmosphere.

- *the coarse mode* contains particles with a diameter greater than 2 microns, generally formed by mechanical processes such as wind erosion, breaking ocean waves, grinding operations in the industry, etc. These particles are efficiently removed by settling under the action of gravity. Their life is short, from several hours to several days. They have a small contribution to the number concentration of particles, but much to their total mass.

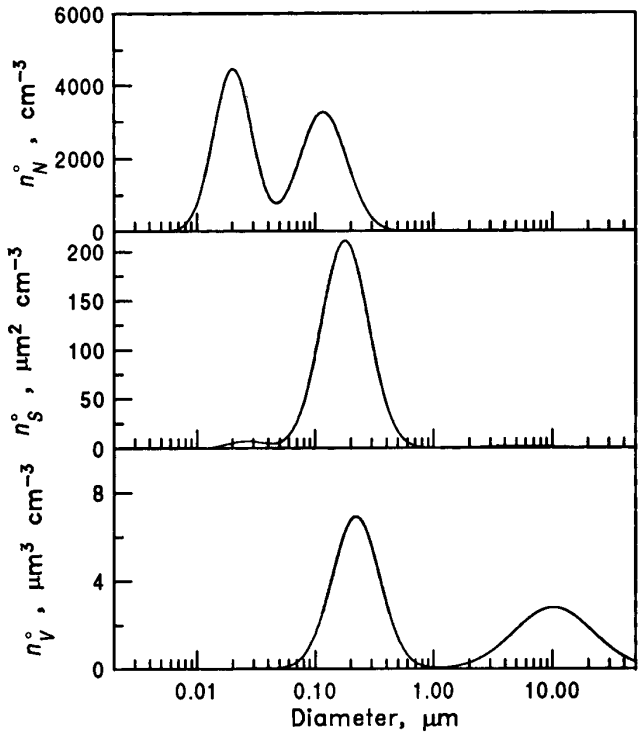

Figure 1.2. Typical remote continental aerosol number, surface and volume distributions (Reproduced from "Atmospheric Physics and Chemistry", Seinfeld and Pandis, 1998)

1.1.3. The aerosol transformation

Once suspended in the atmosphere, aerosols can undergo transformations (changes in size and/or chemical composition) under the action of microphysical processes:

- the condensation (evaporation) of gas molecules of gas from the surface of the aerosol.
- the coagulation of aerosols between them.
- the nucleation: from a thermodynamically unstable phase, liquid or solid fragments of a new phase more stable are formed.

The ensemble of these processes is described by the models of aerosols dynamics.

The aerosol particle size distribution and its temporal and spatial variability is a fundamental aerosol property, especially regarding CCN activity. Nucleation is one of the key process controlling particles number distributions (Merikanto et al., 2009). Model estimates suggest that new particle formation can contribute up to 40% of the CCN at the boundary layer, and 90% in the remote troposphere (Pierce and Adams, 2007).

Pure sulfuric acid (H_2SO_4) has a low vapor pressure at atmospheric temperatures (Ayers et al., 1980). The H_2SO_4 vapor pressure is reduced further in the presence of water (Marti et al, 1997) due to the large mixing enthalpy that is freed when the two substances are mixed. When H_2SO_4 is produced from sulfur dioxide (SO_2) in the gas phase, it is therefore easily super-saturated and the gaseous H_2SO_4 starts to condense. Water vapor is omnipresent in the atmosphere and therefore a condensation of H_2SO_4 and H_2O is always occurring. If the gaseous H_2SO_4 molecules do not encounter pre-existing (aerosol) surfaces to condense on before colliding with other H_2SO_4 and H_2O molecules, they may cluster with the other molecules. If these clusters continue to grow and overcome the nucleation barrier, then new, thermodynamically stable aerosol particles are formed from the gas phase. This is termed *binary homogeneous* nucleation: *binary* for the two substances H_2SO_4 and H_2O that nucleate and *homogeneous* because no other catalyst like a foreign surface is involved in the formation.

Nucleation was observed at a range of atmospheric and meteorological conditions. Many open questions remain about the details of the nucleation mechanism and about the nucleating agents. The nucleation and subsequent growth processes influence the total particle number, the particle size distribution as well as the chemical and optical properties of the atmospheric aerosol.

Climatic effects, like the indirect aerosol effects, are potentially influenced by the number of nucleation mode particles growing to sizes at which they can become active cloud condensation nuclei (Spracklen et al., 2006, Pirjola et al., 2004). Sulfur dioxide is considered the most important precursor gas for atmospheric nucleation particles. It is emitted into the atmosphere mostly by anthropogenic sources such as combustion of sulfur-containing fossil fuels (Stern, 2005). Therefore, aerosol nucleation in the atmosphere would be expected to be enhanced by anthropogenic activities. On the other hand, the pre-existing aerosol that can take up gaseous sulfuric acid and thereby suppressing nucleation is increased as well by anthropogenic sources.

Several nucleation mechanisms have been discussed to occur in the atmosphere. The binary nucleation of sulfuric acid and water (Noppel, et al., 2002, Vehkamaki et al., 2002, Yu, 2006, Hanson, Lovejoy, 2006), the ternary nucleation of H_2SO_4, H_2O, and ammonia (NH_3) (Coffman et al., 1995, Weber et al., 1996, Korhonen et al, 1999, Yu, 2006), ion-induced nucleation (Yu, Turco, 2001, Laakso et al., 2002, Eichkorn et al. 2002, Lee, et al., 2004, Lovejoy et al., 2004, Kazil, Lovejoy, 2004) and reactive nucleation involving sulfuric acid and organic acids (R.H. Zhang et al., 2004, Metzger et al., 2010) are most prominent.

The schematics of an atmospheric nucleation process of H_2SO_4 and H_2O with subsequent growth involving also organics is illustrated in Fig. 1.3. The particles eventually may grow large enough to act as cloud condensation nuclei.

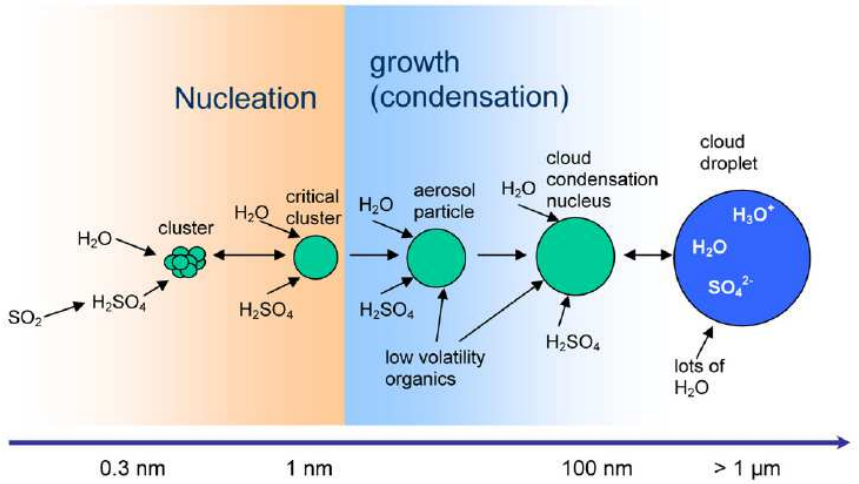

Figure 1.3. Schematic representations of the nucleation and subsequent growth process for atmospheric binary homogeneous nucleation of H_2SO_4 and H_2O. (adopted from Curtius, 2006)

Parameterized equations of the nucleation rates, size of the critical cluster and critical cluster composition as a function of the gas-phase concentration of the involved chemical species and as a function of temperature have been derived for the binary H_2SO_4/H_2O system (Kulmala et al., 1998, Vehkamaki et al., 2002), the ternary $H_2SO_4/H_2O/NH_3$ system (Napari et al., 2002b), the ion-induced nucleation of the H_2SO_4/H_2O system (Modgil et al, 2005) as well as for organics nucleation (Metzger et al., 2010).

1.1.4. Chemical composition

We distinguish between inorganic aerosols and organic aerosols. The major inorganic species simulated in the aerosol models include sulfates, nitrates, chlorates, ammonia and sodium. Organic species are less well known (especially their activity). For this reason the modeled species are generally used to simulate the organic phase with the method of allocation between phases simplified. Finally, inert species such as mineral dust and elemental carbon also contribute significantly to the aerosol mass.

The study made by Putaud et al. (2004) give a detailed chemical characterization of the aerosol for various European sites (urban, rural, traffic). A fairly homogeneous composition of PM2.5 and PM10 were observed on different urban sites. As shown in Fig. 1.4, the urban aerosol (PM2.5 and PM10) is composed from 5 to 10% of black carbon, 20% organic matter, from 35 to 45% inorganic material and 5 to 10% mineral dust. This predominance of organic matter and the inorganic fraction in the secondary composition the aerosol attests the importance of the processes of secondary particulate formation and transport over long distances. The coarse fraction of the aerosol is mainly composed of mineral dust (> 20%) and salt (10%). The unidentified fraction ("unknown") of the aerosol is between 17 and 45% of the total mass, which illustrates the difficulty of measuring the composition of the particles, due to the variety of its constituents and limits of measuring instruments. The difference between urban and rural sites lies mainly in the relative contribution of largest nitrate and ammonium in urban areas, and sulfates in rural areas.

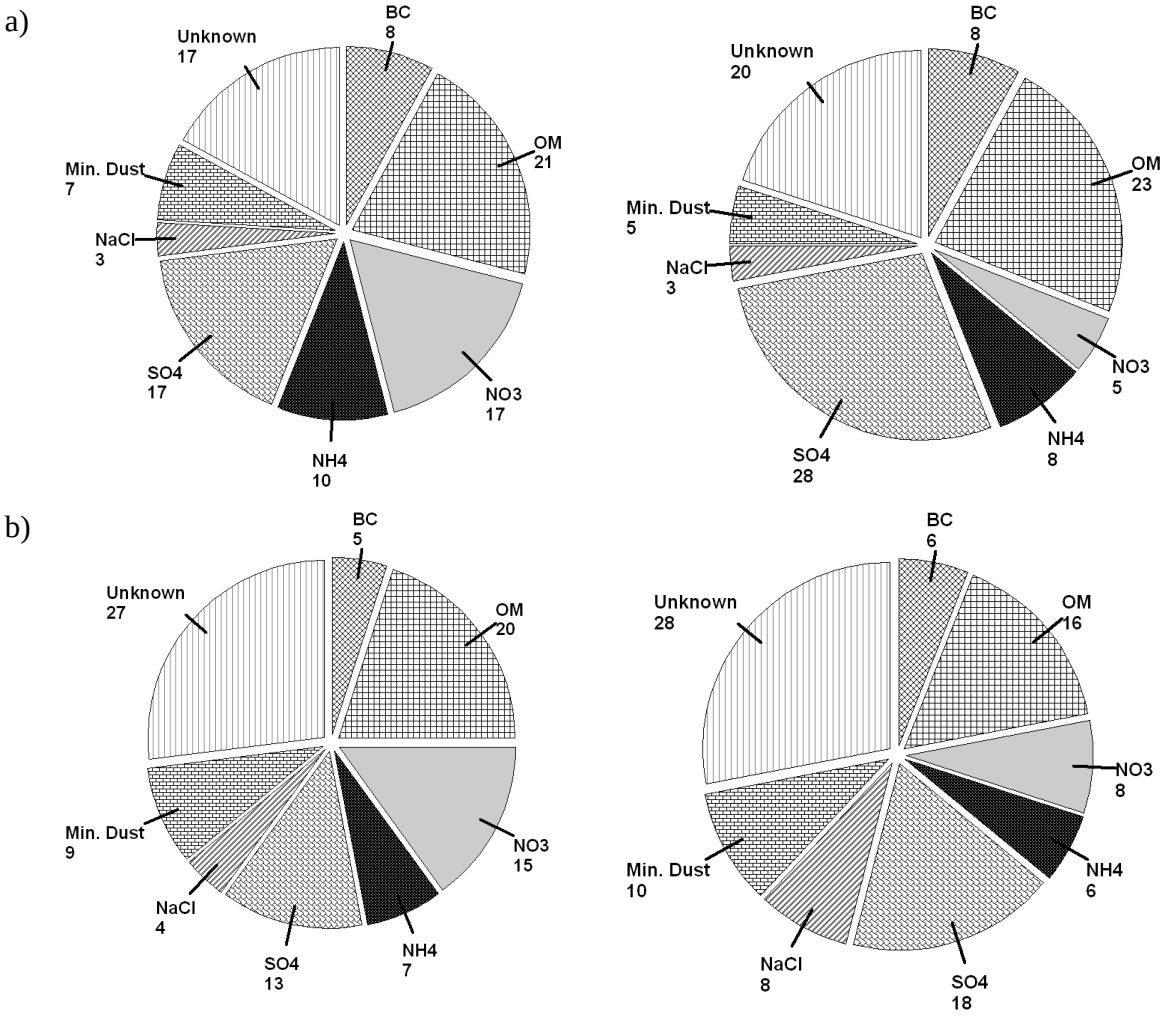

Figure 1.4. The average composition of PM2.5 (a) and PM10 (b) observed in several European stations (urban-left panel and rural-right panel). Adapted from (Putaud et al. 2004)

1.1.5. The deposition

Once suspended in the atmosphere, the aerosols have a limited lifetime before deposition or transformation. The average lifetime of aerosols ranges from few days to one week. However, the lifetime depends on aerosols size and also of its environment.

There is principally two deposition phenomenon:

- dry deposition which depends essentially on the soil rugosity that characterize the capacity to capture the suspended particles;
- wet scavenging of particles that are drained by the droplets of rain until the soil surface.

1.1.6. Emissions estimation

Aerosols have various sources from both natural and anthropogenic processes. Natural emissions include wind-blown mineral dust, aerosol and precursor gases from volcanic eruptions, natural wild fires, vegetation, and oceans. Anthropogenic sources include emissions from fossil fuel and biofuel combustion, industrial processes, agriculture practices, and human-induced biomass burning.

Following earlier attempts to quantify man-made primary emissions of aerosols (Turco et al., 1983; Penner et al., 1993), a systematic work was undertaken in the late 1990s to calculate emissions of black carbon (BC) and organic carbon (OC), using fuel-use data and measured emission factors (Liousse et al., 1996; Cooke and Wilson, 1996; Cooke et al., 1999). The work was extended in greater detail and with improved attention to source-specific emission factors in Bond et al. (2004), who provides global inventories of BC and OC for the year 1996, with regional and source-category discrimination that includes contributions from industrial, transportation, residential solid-fuel combustion, vegetation and open biomass burning (forest fires, agricultural waste burning, etc.), and diesel vehicles.

Emissions from natural sources—which include wind-blown mineral dust, wildfires, sea salt, and volcanic eruptions—are less well quantified, mainly because of the difficulties of measuring emission rates in the field and the unpredictable nature of the events. However, dust emission schemes that have been developed and used in the regional models range from simple type schemes, in which the vertical dust flux depends on a prescribed erodible surface fraction and fixed threshold friction velocity (Gillette and Passi, 1998; Uno et al., 2001) to advanced schemes, in which the surface characteristics are taken into account explicitly in the parameterizations of the threshold friction velocity, and horizontal and vertical fluxes (Marticorena and Bergametti, 1995; Shao et al., 1996; Shao, 2004). Every dust emission scheme adopts different parameterizations for the wind erosion mechanism and the influence of input parameters is different, thus the scattering of simulation results is yielded.

Sea salt aerosol (SSA) often dominates the mass concentration of marine aerosol, especially at locations remote from anthropogenic or other continental sources, and SSA is one of the dominant aerosols globally (along with mineral dust) in terms of mass emitted into the atmosphere. Estimates of global annual mass emission of sea salt (calculated as the integral over

the size-distributed number production flux times the volume per particle times the mass of sea salt per unit volume of seawater) with current chemical transport models and global climate models, using various parameterizations of the sea spray source function (SSSF), range over nearly 2 orders of magnitude, from 0.02 to 1 × 1014 kg yr^{-1} (Textor et al., 2006). Much of this variation is due to the different dependences on wind speed and to the upper size limit of the particles included.

Aerosols can be produced from atmospheric trace gases via chemical reactions, and those aerosols are called secondary aerosols, as distinct from primary aerosols that are directly emitted to the atmosphere as aerosol particles.

For example, most sulfate and nitrate aerosols are secondary aerosols that are formed from their precursor gases, sulfur dioxide (SO_2) and nitrogen oxides (NO and NO_2, collectively called NO_x), respectively.

The formation of ammonium nitrate aerosol depends on the thermodynamic state of its precursor and depends strongly on the environmental conditions. Gaseous ammonia and nitric acid react in the atmosphere to form aerosol ammonium nitrate, NH_4NO_3.

$$NH_3(g) + HNO_3(g) \leftrightarrow NH_4NO_3(s) \quad (1.1)$$

Ammonium nitrate is formed in areas characterized by high ammonia and nitric acid conditions and low sulfate conditions. Depending on the ambient relative humidity (RH), ammonium nitrate may exist as a solid or as an aqueous solution of NH_4 and NO_3. Equilibrium concentrations of gaseous NH_3 and HNO_3, and the resulting concentration of NH_4NO_3 is calculated by thermodynamical principals, requiring the ambient RH and temperature. At low temperatures the equilibrium of the system shifts towards the aerosol phase. At low RH conditions NH_4NO_3 is solid, and at RH conditions above the deliquescence, NH_4NO_3 will be found in the aqueous state.

$$NH_3(g) + HNO_3(g) \leftrightarrow NH_4 + NO_3. \quad (1.2)$$

For a given temperature the solution of the equilibrium equation requires the calculation of the corresponding molarities. These concentrations depend not only on the aerosol nitrate and ammonium but also on the amount of water in the aerosol phase. Therefore, calculations of the

aerosol solution composition require estimation of the aerosol water content. The presence of water allows NH_4NO_3 to dissolve in the liquid aerosol particles and increases its aerosol concentration. Ammonium and nitrate will exist in the aerosol phase only if there is enough ammonia and nitric acid present to saturate the gas phase.

Sulfuric acid plays an important role in nitrate aerosol formation. Sulfuric acid possesses an extremely low vapor pressure. Furthermore $(NH_4)_2SO_4$ is the preferred form of sulfate, so each mole of sulfate will remove 2 moles of ammonia from the gas phase.

$$NH_3 + H_2SO_4(g) \leftrightarrow (NH_4)HSO_4 \quad (1.3)$$

$$NH_3 + (NH_4)H_2SO_4(g) \leftrightarrow (NH_4)_2SO_4 \quad (1.4)$$

Therefore two regimes are important for nitrate formation: the ammonia-rich and the ammonia-poor case.

Heterogeneous reactions of gaseous species with coarse aerosol species, like mineral dust and sea salt particles, have an important impact on NH_4NO_3 formation. Once HNO_3 is formed, it is most likely captured by coarse mode sea-salt and dust particles, leading to a depletion of aerosol nitrate in the fine mode. During the night when ammonia is present in excess, ammonium nitrate can be formed; however, since this salt is thermodynamically not stable, it can evaporate during the day whereby the aerosol precursor gases NH_3 and HNO_3 are likely to condense on preexisting and larger aerosol particles (Wexler and Seinfeld, 1990).

Those sources have been studied for many years and are relatively well known. By contrast, the sources of secondary organic aerosols (SOA) are poorly understood, including emissions of their precursor gases (called volatile organic compounds, VOC) from both natural and anthropogenic sources and the atmospheric production processes.

Globally, sea salt and mineral dust dominate the total aerosol mass emissions because of the large source areas and/or large particle sizes.

However, sea salt and dust also have shorter atmospheric lifetimes because of their large particle size, and are radiatively less active than aerosols with small particle size, such as sulfate, nitrate, BC, and particulate organic matter (POM, which includes both carbon and non-carbon mass in the organic aerosol), most of which are anthropogenic in origin.

1.2. Air pollution modeling

Air pollution modeling is a numerical tool used to describe the causal relationship between emissions, meteorology, atmospheric concentrations, deposition, and other factors. Air pollution measurements give important, quantitative information about ambient concentrations and deposition, but they can only describe air quality at specific locations and times, without giving clear guidance on the identification of the causes of the air quality problem. Air pollution modeling, instead, can give a more complete deterministic description of the air quality problem, including an analysis of factors and causes (emission sources, meteorological processes, and physical and chemical changes), and some guidance on the implementation of mitigation measures.

Air pollution models play an important role in science, because of their capability to assess the relative importance of the relevant processes. Air pollution modeling is the only method which quantifies the deterministic relationship between emissions and concentrations/depositions, including the consequences of past and future scenarios and the determination of the effectiveness of abatement strategies. This makes air pollution models indispensable in regulatory, research, and forensic applications.

The concentrations of substances in the atmosphere are determined by: 1) transport, 2) diffusion, 3) chemical transformation, and 4) deposition on the ground. Transport phenomena, characterized by the mean velocity of the fluid, have been measured and studied for centuries. For example, the average wind has been studied by man for sailing purposes. The study of diffusion (turbulent motion) is more recent.

Among the first articles that mention turbulence in the atmosphere, are those by Taylor (1915, 1921).

One of the first challenges in the history of air pollution modeling (e.g., Sutton, 1932, Bosanquet, 1936) was the understanding of the diffusion properties of plumes emitted from large industrial stacks. For this purpose, a very successful, yet simple model was developed – the Gaussian Plume Model. This model was applied for the main purpose of calculating the maximum ground level impact of plumes and the distance of maximum impact from the source. The model was formulated by determining experimentally the horizontal and vertical spread of the plume, measured by the standard deviation of the plume's spatial concentration distribution.

Experiments provided the geometrical description of the plume by plotting the standard deviation of its concentration distribution, in both the vertical and horizontal direction, as a function of the atmospheric stability and downwind distance from the source. Atmospheric stability is a parameter that characterizes the turbulent status of the atmosphere.

In the 1960s, the studies concerning dispersion from a point source continued and were broadening in scope. Major studies were performed by Hogstrom (1964), Turner (1964), Briggs (1965) (the developer of the well-known plume-rise formulas), Moore (1967), Klug (1968). The use and application of the Gaussian plume model spread over the whole globe, and became a standard technique in every industrial country to calculate the stack height required for permits. The Gaussian plume model concept was soon applied also to line and area-sources. Gradually, the importance of the mixing height was realized (Holzworth, 1967, Deardorff, 1975) and its major influence on the magnitude of ground level concentrations. To include the effects of the mixing height, multiple reflections terms were added to the Gaussian Plume model (e.g., Yamartino, 1977).

Shortly after 1970, scientists began to realize that air pollution was not only a local phenomenon. It became clear - firstly in Europe - that the SO_2 and NO_x emissions from tall stacks could lead to acidification at large distances from the sources. It also became clear - firstly in the US - that ozone was a problem in urbanized and industrialized areas. And so it was obvious that these situations could not be tackled by simple Gaussian-plume type modeling.

Two different modeling approaches were followed, Lagrangian modeling and Eulerian modeling. In Lagrangian modeling, an air parcel (or “puff”) is followed along a trajectory, and is assumed to keep its identity during its path. In Eulerian modeling, the area under investigation is divided into grid cells, both in vertical and horizontal directions.

Lagrangian modeling, directed at the description of long-range transport of sulfur, began with studies by Rohde (1972, 1974), Eliassen (1975) and Fisher (1975). The work by Eliassen was the start for the well-known EMEP-trajectory model which has been used over the years to calculate air pollution of acidifying species and later, photo-oxidants. Lagrangian modeling is often used to cover longer periods of time, up to years.

Eulerian modeling began with studies by Reynolds (1973) for ozone in urbanized areas, with Shir and Shieh (1974) for SO_2 in urban areas, and Egan (1976) and Carmichael (1979) for regional scale sulfur. From the modeling studies by Reynolds on the Los Angeles basin, the well-

known Urban Airshed Model-UAM originated for photochemical simulations. Eulerian modeling, in these years, was used only for specific episodes of a few days.

So in general, Lagrangian modeling was mostly performed in Europe, over large distances and longer time-periods, and focused primarily on SO_2. Eulerian grid modeling was predominantly applied in the US, over urban areas and restricted to episodic conditions, and focused primarily on O_3. Also hybrid approaches were studied, as well as particle-in-cell methods (Sklarew et al., 1971). Early papers on both Eulerian and Lagrangian modeling are by Friedlander and Seinfeld (1969), Eschenroeder and Martinez (1970) and Liu and Seinfeld (1974).

A comprehensive overview of long-range transport modeling in the seventies was presented by Johnson (1980).

The next, obvious step in scale is global modeling of the earth's troposphere. The first global models were 2-D models, in which the global troposphere was averaged in the longitudinal direction (Isaksen, 1978). The first, 3-D global models were developed by Peters (1979) (see also Zimmermann, 1988).

It can be stated that, since approximately 1980, the basic modeling concepts and tools were available to the scientific community. Developments after 1980 concerned the fine-tuning of these basic concepts.

Photochemical air quality models have become widely recognized and routinely utilized tools for regulatory analysis and attainment demonstrations by assessing the effectiveness of control strategies. These photochemical models are large-scale air quality models that simulate the changes of pollutant concentrations in the atmosphere using a set of mathematical equations characterizing the chemical and physical processes in the atmosphere. These models are applied at multiple spatial scales from local, regional, national, and global.

1.2.1. Modeling of atmospheric aerosols

The aerosols modeling capability has developed rapidly in the past decade. In the late 1990s, there were only a few models that were able to simulate one or two aerosols components, but now there are a few dozen models that simulate a comprehensive suite of aerosols in the atmosphere. As introduced before, aerosols consist of a variety of species, including dust, sea salt, sulfate, nitrate, and carbonaceous aerosols (black and organic carbon) produced from natural

and man-made sources with a wide range of physical properties. Because of the complexity of the processes and composition, and highly inhomogeneous distribution of aerosols, accurately modeling atmospheric aerosols and their effects remains a challenge. Models have to take into account not only the aerosol and precursor emissions, but also the chemical transformation, transport, and removal processes (e.g. dry and wet depositions) to simulate the aerosol mass concentrations. Furthermore, aerosol particle size can grow in the atmosphere because the ambient water vapor can condense on the aerosol particles. This "swelling" process, called hygroscopic growth, is most commonly parameterized in the models as a function of relative humidity. Modeling plays a key role for quantitatively integrating knowledge and for evaluating our understanding of physical and chemical processes in the atmosphere. The main goal of aerosol modeling is to establish a detailed description of the aerosol particle concentrations and their composition and size distribution. This requires advanced modeling techniques and innovation as well as reliable validation data of particle characteristics. The aerosol modules implemented in a chemistry transport models generally take into account gas-to-particle conversion and aerosol dynamics and enable simulation of the complete aerosol number/mass/composition distribution.

1.2.2. Choice of Vertical Coordinate System for Air Quality Modeling

Many different types of vertical coordinates have been used for various meteorological simulations. For example, the geometric height is used to study boundary layer phenomenon because of its obvious advantage of relating near surface measurements with modeled results.

Pressure coordinates are natural choices for atmospheric studies because many upper atmospheric measurements are made on pressure surfaces. Because most radiosonde measurements are based on hydrostatic pressure, one may prefer use of the pressure coordinate to study cloud dynamics. This idea of using the most appropriate vertical coordinate for describing a physical process is referred to as a generic coordinate concept (Byun et al., 1995).

Several different generic coordinates can be used in a CTM for describing different atmospheric processes while the underlying model structure should be based on a specific coordinate consistent with the meteorological model.

Byun (1999a) discusses key science issues related to using a particular vertical coordinate for air quality simulations. They include a governing set of equations for atmospheric dynamics and thermodynamics, the vertical component of the Jacobian (metric tensor associated with the vertical coordinate transformation), the form of continuity equation for air, the height of a model layer (expressed in terms of geopotential height), and other special characteristics of a vertical coordinate for either hydrostatic or non-hydrostatic atmosphere applications.

Not only the assumptions on atmospheric dynamics, but also the choice of coordinate can affect the characteristics of atmospheric simulations. For the time-independent vertical coordinates (z, p, sigma-z, sigma-p), the vertical Jacobians are also time-independent. Especially with the hydrostatic assumption, one can obtain a diagnostic equation for the vertical velocity component which includes sound-waves together with meteorological signals. Further assumptions on flow characteristics, such as anelastic approximation, provide a simpler diagnostic equation for the non-solenoidal air flow. For such cases, with or without the anelastic approximation, one can maintain trace species mass conservation in a CTM by using the vertical velocity field estimated from the diagnostic relation. This diagnostic works whether the horizontal wind components, temperature, and density field data are directly provided from a meteorological model or interpolated from hourly data at the transport time step. This suggests that the mass error can be estimated with the diagnostic relations that originate from one of the governing equations of the preprocessor meteorological models. For a non-hydrostatic atmosphere, which does not have a special diagnostic relation for time independent coordinate, one should rely on methods to account for the mass consistency errors.

1.2.3. Off-line and On-line Modeling Paradigms

Air quality models are run many times to understand the effects of emissions control strategies on the pollutant concentrations using the same meteorological data. A non-coupled prognostic model can provide adequate meteorological data needed for such operational use. This is the so-called off-line mode air quality simulation. However, a successful air quality simulation requires that the key parameters in meteorological data be consistent. For example, to ensure the mass conservation of trace species, the density and velocity component should satisfy the continuity equation accurately. Details of this issue will be discussed below.

Dynamic and thermodynamic descriptions of operational meteorological models should be self-consistent, and necessary meteorological parameters are readily available at the finite time steps needed for the air quality process modules during the numerical integration. This is the so-called on-line mode air quality simulation. There have been a few successful examples of integrating meteorology and atmospheric chemistry algorithms into a single computer program (e.g., Vogel et al., 1995, Arteta, 2005). For certain research purposes, such as studying two-way interactions of radiation processes, the on-line modeling approach is needed. However, the conventional on-line modeling approach, where chemistry-transport code is imbedded in one system, exhibits many operational difficulties. For example, in addition to tremendously increasing the computer resource requirements, differences in model dynamics and code structures hinder development and maintenance of a fully coupled meteorological/chemical/emissions modeling system for use in routine air quality management.

Figure 1.5 shows structures of the on-line and off-line air quality modeling systems, respectively, commonly used at present time.

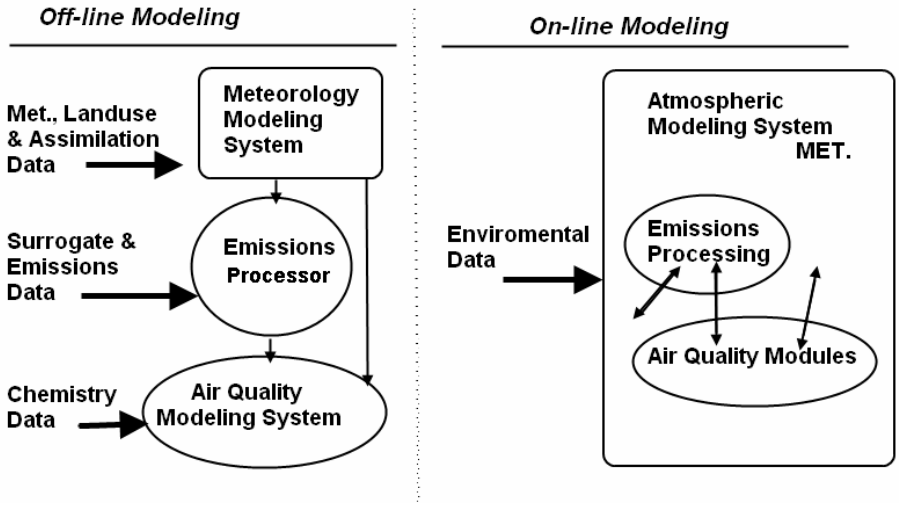

Figure1.5. The structure of current on-line and off-line air quality models

Table 1.1 compares a few characteristics of on-line and off-line modeling paradigms (Byun, 1999b). Each method has associated pros and cons. However, to accomplish the goals of multiscale on-line/off-line modeling with one system, a full adaptation of the one-atmosphere concept is needed. These are:

- Development of the fully coupled chemistry-transport model to a meteorological modeling system requires a fundamental rethinking of the atmospheric modeling approach in general.

  Some of the suggested requirements for a next generation mesoscale meteorological model that can be used as a host of the on-line/off-line modeling paradigms are:
- Scalable dynamics and thermodynamics: Use fully compressible form of governing set of equations and a flexible coordinate system that can deal with multiscale dynamics.
- Unified governing set of equations: Not only the weather forecasting, dynamics and thermodynamics research but also the air quality studies should rely on the same general governing set of equations describing the atmosphere.
- Mass conservation in each grid box: As opposed to the simple conservation of domain total mass, cell-based conservation of the scalar (conserving) quantities is needed. Use of proper state variables, such as density and entropy, instead of pressure and temperature, and representation of governing equations in the conservation form rather than in the advective form are recommended.
- State-of-the-art data assimilation method: Not only the surface measurements and upper air soundings, but also other observation data obtained through the remote sensing and other in situ means must be included for the data assimilation.
- Multiscale physics descriptions: It has been known that certain parameterizations of physical processes, including clouds, used in present weather forecasting models are scale dependent. General parameterization schemes capable of dealing with a wide spectrum of spatial and temporal scales are needed.

During this thesis we used the off-line air quality model CHIMERE. The description of this model is done in the section 2.2.

The CHIMERE model was chosen due to the advantages of the off-line modeling approaches:

• possibility of independent parameterizations;

• low computational cost (if numerical weather prediction data are available is not necessary to run a meteorological model);

• independence of atmospheric pollution model runs on meteorological model computations;

• more flexible grid construction and generation for CTMs, e.g. within the surface and boundary layer;

• suitable for emission scenarios analysis and air quality management.

Table 1.1. Characteristics of on-line and off-line modeling paradigms

	Off-line modeling	On-line modeling
Dynamic consistency	-Need sophisticated interfaces processors -need careful treatment of meteorology data in AQM	-Easier to accomplish, but must have proper governing equations -meteorology data available as computed
Process interactions	-No two-way interactions between meteorology and air quality	-Two-way interactions between meteorology and air quality -small error in meteorological data will cause large problem in air quality simulation
System characteristics	-Systems maintained at different institutions -modular at system level. Different algorithms can be mixed and tested -large and diverse user base -community involvement	-Proprietary ownership -expensive in terms of computer resource need (memory and CPU) -unnecessary repeat of computations for control strategy study -low flexibility -limited user base
Application characteristics	-Easy to test new science concept -efficient for emissions control study -good for independent air quality process study	-Difficult to isolate individual effects -excellent for studying feedback of meteorology and air quality

1.2.4. Overview of Existing Algorithms for Aerosol Modeling

1.2.4.1. Available thermodynamic equilibrium models

Several gas aerosol atmospheric equilibrium models have been developed with varying degrees of complexity and rigor in both the computational and the thermodynamic approaches. Bassett and Seinfeld (1983) developed EQUIL in order to calculate the aerosol composition of the ammonium-sulfate-nitrate-water aerosol system. They later introduced an improved version,

KEQUIL, to account for the dependence of the partial vapor pressure on the spherical shape of the particles, the so-called Kelvin effect (Bassett and Seinfeld, 1984).

Another widely used model for the sulfate-nitrate-ammonia-water system is MARS (Saxena et al., 1986) that aimed at reducing the computational time while maintaining reasonable agreement with EQUIL and KEQUIL. MARS was developed for incorporation into larger aerosol models, so speed was a major issue. The main feature of MARS was the division of the whole aerosol species regime into subdomains, in order to minimize the viable species in each one. Since each domain contains fewer species than the entire concentration domain does, the number of equations solved is reduced, thus, speeding up the solution process. A major drawback of MARS is that it uses thermodynamic properties (equilibrium constants, activity coefficients) at 298.15 K, thus affecting the distribution of volatile species (nitrates) between the gas and the particulate phases, if calculations are done at a different temperature (Nenes et al., 1998). All the simplifications rendered MARS about four hundred times faster than KEQUIL and sixty times faster than EQUIL.

The major disadvantage of the previous three models was the neglect of sodium and chloride species, which are major components of marine aerosols. These species were first incorporated into the SEQUILIB model (Pilinis and Seinfeld, 1987). SEQUILIB used a computational scheme similar to that of MARS. It also presented an algorithm for calculating the distribution of volatile species among particles of different sizes so that thermodynamic equilibrium is achieved between all the particles and the gas phase.

In 1993, Kim *et al.* developed SCAPE, which implements a domain-oriented solution algorithm similar to that of SEQUILIB, but with updated thermodynamic data for the components. SCAPE also calculates the pH of the aerosol phase from the dissociation of all weak and strong acid/base components, and includes the temperature dependence of single salt deliquescence points using the expressions derived by Wexler and Seinfeld (1991). SCAPE embodied the main correlations available for calculating multi-component solution activity coefficients, and let the user select the one which should be used. SCAPE always attempts to solve for a liquid phase, by using SEQUILIB to calculate approximate concentrations that serve as a starting point for the iterative solution of the full equilibrium problem. Because of this approach, SCAPE can predict the presence of water, even at very low ambient relative humidities. In certain cases, the activity coefficients may lower the solubility product enough so that there is no solid precipitate

predicted. There is no relative humidity “boundary” that could inhibit this, so a liquid phase may be predicted for relative humidities as low as 20%. There are two ways to solve this problem. Either certain assumptions must be made about the physical state of the aerosol at low relative humidities (like MARS and SEQUILIB), or the full minimization problem must be solved.

A different approach has been followed by Jacobson *et al.* (1996) in their model, EQUISOLV. The equilibrium concentrations are calculated by numerically solving each equilibrium equation separately, based on an initial guess for the concentrations. After solving each equation, the solution vector is updated and the new values are used to solve the remaining equations. This sequence is repeated over and over, until concentrations of all species converge. This open architecture makes it easy to incorporate new reactions and species. However, the general nature of the algorithm could potentially slow down the solution process, when compared to the domain approach used in MARS, SEQUILIB and SCAPE. Solubility products are used to determine the presence of solids. For this reason, EQUISOLV, just like SCAPE, can predict the presence of water even at very low relative humidities. Even for cases in which a solid aerosol is predicted, a negligible amount of water is assumed to exist in order to estimate the vapor pressure of species in the aerosol phase. Whilst this should not affect the results (because there is too little water to affect the solution), additional computation is required, which could increase CPU time.

Another thermodynamic equilibrium model available to the scientific community is ISORROPIA. ISORROPIA models the sodium - ammonium - chloride - sulfate - nitrate - water aerosol system. The aerosol particles are assumed to be internally mixed, meaning that all particles of the same size have the same composition. The number of viable species (thus, the number of equilibrium reactions solved) is determined by the relative abundance of each species and the ambient relative humidity. A more detailed description of the equilibrium reactions and the solution procedure of ISORROPIA is presented elsewhere (Nenes et al.,1998). Special provision was taken in order to render ISORROPIA as fast and computationally efficient as possible. The equilibrium equations for each case were ordered and manipulated so that analytical solutions could be obtained for as many equations as possible. The number of iterations performed during the numerical solution largely determines the speed of the model. Hence, minimizing the number of equations needing numerical solution considerably reduces CPU time.

Adopting this approach, most cases could be solved using only one level of iteration. By comparison, SEQUILIB is more simplistic and potentially faster, but proves to be slower than ISORROPIA, mainly because SEQUILIB solves more equations numerically and uses nested iteration procedures of two (and sometimes three) levels when solving the equations. Another factor that speeds up ISORROPIA is the usage of pre-calculated tables, whenever possible.
CHIMERE uses ISORROPIA as thermodynamic equilibrium model.

1.2.4.2. A comparison of different gas/particle models

Six modules that simulate the gas/particle partitioning of inorganic species were compared using 40 different case studies for the EPA Models-3 Community Multiscale Air Quality (CMAQ) Modeling System. These six modules included MARS-A (Binkowski and Shankar, 1995), SEQUILIB (Pilinis and Seinfeld, 1987), SCAPE2 (Kim and Seinfeld, 1995; Meng et al., 1995), EQUISOLV II (Jacobson, 1999), AIM2 (Clegg et al., 1998a, b) and ISORROPIA (Nenes et al., 1999). All modules treat sulfate, nitrate, ammonium and water. Except for MARS-A, all modules also treat sodium and chloride. In addition, SCAPE2 and EQUISOLV II treat crustal soluble species: calcium, magnesium, potassium and carbonate. The conclusions of this comprehensive review are summarized in Table 1.2.
AIM2 does not simulate alkaline systems and was therefore not considered for incorporation into Models-3/CMAQ. MARS-A is the default model of Models-3/CMAQ. It was selected two new modules for incorporation into Models-3/CMAQ: one that provides treatment of sea salt and is computationally efficient and one that can provide a treatment of all relevant chemical species including sea salt and crustal material. Among the computationally efficient modules, ISORROPIA was judged superior to SEQUILIB (see Table 1.2). For a comprehensive treatment of the aerosol system, both SCAPE2 and EQUISOLV II were considered suitable. Since SCAPE2 was already coupled to the modules that simulate aerosol dynamics, it was selected for incorporation into Models-3/CMAQ.

Table 1.2. Comparison of existing modules for gas/particle partitioning of inorganic chemical species.

	MARS-A	SEQUILIB	ISORROPIA	SCAPE2	EQUISOLV II	AIM2
Performance	Higher H_2O for medium RHs and higher NH_4NO_3 for sulfate-poor cases and low RHs	Poor NO_3 and H^+ predictions for some sulfate-rich cases; higher NH_4NO_3 for sulfate-poor cases and low RHs	Innacurate at some high RHs (above 50%) for various conditions including some acidic, neutral and alkaline cases	Higher H^+ for some sulfate-rich cases and low RHs	Higher NH_4Cl for cases with NaCl and low RHs	Not valid for alkalin systems
Stability	Good	Poor for some sulfate-rich/neutral cases and high RHs cases	Good	Non-convergence for some sulfate-rich cases and low RHs	Incomplete convergence for low RHs	Numerical difficulties for very low initial H^+ and NO_3
Speed	Fast	Fast	Fast	Moderately fast	Slow for one cell, fast for multiple cells	Relatively slow

1.2.4.3. Parameterization of the size distribution of particles

To represent the size distribution of aerosols, several approaches can be used, however, modal and sectional representations are the most commonly used in current models. Each has its advantages, but the choice of particle size is essential as it affects the performance of the model. In the modal approach, the size distribution consists of several modes (typically modes of nucleation, accumulation and coarse mode) represented by functions analytical generally log-normal or gamma (Binkowski and Shankar, 1995; Whitby and McMurry, 1997). The main advantage of this approach comes from the analytical solution equations that govern the evolution of particle size, which significantly reduces the number of variables and thus reduce the computation time. However, the modal approach does not describe the variability of aerosols according to their size, the aerosols properties are assumed uniform in each mode (Zhang et al., 2002).

In the sectional approach, the size distribution is approximated by a finite number of sections or

intervals (Warren, 1986). In a given mesh model, the particles belonging the same section have the same chemical composition and the same dynamic properties. The number of sections can vary from 2 to tens, knowing that the accuracy increases with the number of sections, but also the computation time. To allow the correct consideration on aerosol dynamic processes, a minimum of 6 to 8 sections is recommended (Zhang et al. 2002). The sectional approach is used in CHIMERE to describe the aerosol dynamic process. The sectional approach is well suited to the detailed study of the aerosol processes, while the modal approach (generally comprising 2-3 modes) is better to modeling on a global scale which requires greater speed of calculation.

In addition, the models must take into account the processes that influence the distribution in aerosol size. The main ones are *the nucleation*, which creates new particles by significantly increasing their number and their mass somewhat as the particles are formed very small, *the condensation and absorption*, which increases the mass of particles and retain their number; *the coagulation*, which reduces the number of particles, but retains the mass. Zhang et al. (1999) have evaluated different parameterizations used in the models and concluded that the existence of many uncertainties, particularly regarding the treatment of nucleation.

1.2.4.4. Nucleation parameterizations

The nucleation process is the formation of new aerosol particles by aggregation of condensable gas molecules. It occurs when the partial pressures of species likely to become higher than the condensing saturated vapor pressure associated and can lead to a sharp increase in the number of ultrafine particles (diameter between 1 and 10 nm), the increase of the mass remains low.

The classical nucleation theory was developed to describe homogeneous nucleation, that is nucleation of vapor on embryos that consist only of vapor molecules. The theory involves many approximations and is based on equations that describe the change of concentrations of molecule clusters of different sizes. At saturation equilibrium the average concentration of the clusters is constant, that is if a molecule is added to a cluster, this is matched by the loss of a molecule from a cluster. When the saturation is sufficiently above the equilibrium value and a large number of molecules impact on the clusters, larger clusters can be formed. When the cluster exceeds a critical size (critical cluster) it likely continues to grow. The supersaturation required for this to happen is called “critical supersaturation” and, for a given vapor, is a function of the

temperature. The nucleation rate is defined as the net number of clusters which grow larger than the critical size per time unit.

Use of different binary nucleation parameterizations in 3-D models introduce significant uncertainties in the predicted number production rates and number concentrations of PM2.5, particularly in the nucleation mode (Roth et al., 2003). The binary parameterizations of Wexler et al. (1994), Pandis et al. (1994), Fitzgerald et al. (1998) and Harrington and Kreidenweis (1998) are based on the same set of calculations for the nucleation rates performed by Jaecker-Voirol and Mirabel (1989), which calculate the absolute nucleation rates based on heteromolecular homogeneous nucleation theory of the H_2SO_4–H_2O system. Discrepancies occurring between different parameterizations of nucleation rates originate from the different algorithms used for these parameterizations. The parameterizations of Kulmala et al. (1998) and Vehkamaki et al. (2002) are also based on the classical binary homogeneous nucleation model that simulates nucleation kinetics and accounts for hydration.

McMurry and Friedlander (1979) use an approach that partitions gas-to-particle conversion between nucleation of new particles and condensation on existing particles, which is a more realistic approach than the one based on the absolute prediction of a nucleation rate. The ternary nucleation parameterization of Napari et al. (2002a) is based on a detailed parameterization of ternary nucleation (H_2SO_4-H_2O-NH_3) with the largest deviation between modeling results and observation no more than one order of magnitude.

1.2.4.5. Brownian coagulation

The random variation in the bombardment of particles by gas molecules is the origin of the particle Brownian motion. Brownian coagulation takes place when, due to this motion, particles collide and adhere to each other, forming larger particles. This process causes the decrease of the total particle number concentration and an increase in the mean particle size.

Beside Brownian motion, other forces, such as Van der Waals interaction, shear forces or sedimentation can also affect coagulation of particles.

Kerminen (1993) made a study on the effect of Van der Waals forces and Brownian coagulation on the particle size distribution. The results show that Van der Waals forces can enhance coagulation between ultrafine particles of similar size. The effect is visible on short time scales.

For studies on time scales larger than a few minutes only Brownian coagulation needs to be included.

The rate of change of the number concentration of a polydisperse aerosol due to coagulation is

$$\left(\frac{\partial n}{\partial t}\right)_{coag} = -\frac{1}{2}\int_0^\infty \int_0^\infty k_{1,2}\, n(r_1) n(r_2)\, dr_1 dr_2 \tag{1.5}$$

where $n(r_1)$ and $n(r_2)$ are the number concentrations of particles of radius r_1 and r_2, respectively. $k_{1,2}$ is the coagulation coefficient expressed by

$$k_{1,2} = 4\pi(r_1 + r_2)(D_1 + D_2)\beta \tag{1.6}$$

where D_1 and D_2 are the particle diffusion coefficients ($cm^2\ s^{-1}$) and β is the Fuchs correction factor (Fuchs, 1964). The coagulation coefficient has the unit of $cm^3\ s^{-1}$. The diffusion coefficient and β are written as:

$$D = \frac{k_B T C_c}{6\pi\eta r} \tag{1.7}$$

and

$$\beta = \frac{1}{1 + \frac{4(D_1 + D_2)}{(r_1 + r_2)\sqrt{(v_1^2 + v_2^2)}}} \tag{1.8}$$

where k_B is the Boltzman constant, η is the viscosity of air, C_c the Cunningham correction factor and v is the mean thermal velocity of the particles, with

$$C_c = 1 + \frac{\lambda}{r}\left[1.257 + 0.4\exp(-1.1r/\lambda)\right] \tag{1.9}$$

and

$$v = \sqrt{\frac{8k_B T}{\pi M}} \tag{1.10}$$

with λ the air mean free path and M the particle mass (Seinfeld and Pandis, 1998).

The matrix representing the coagulation coefficient is symmetric, with, along the diagonal, minimum values for particles having the same size. The temperature determines the Brownian motion of the particles that decreases with particle size. The maximum value of the coagulation coefficient is reached for coagulation taking place between a very small and a very large particle: the first moves fast, the latter offers the largest surface for the impact.

1.2.4.6. Condensation

The other important phenomenon influencing the growth of atmospheric particles is condensation. Particles in the size range of 0.01 μm to 1 μm grow mainly by vapor molecules that diffuse to a particle surface and are taken up by the particle.

When a particle is not in equilibrium with the surrounding gas phase, i.e. when the equilibrium concentration is not equal to the concentration of the compound in the gas phase, a molecular flux of the gas to the particle takes place (or vice versa). The rate of change of the particle number concentration is

$$\left(\frac{\partial n(r)}{\partial t}\right)_{cond\,/\,evap} = -\frac{\partial}{\partial r}\left(\frac{\partial r}{\partial t} n(r)\right) \tag{1.11}$$

Where $\partial r/\partial t$ is the rate of change of the particle radius due to condensation/evaporation on the particle. The mass transfer process depends on the particle size relative to the mean free path of the gas molecules, λ. When the particle size is much smaller than λ, the air resists the particle motion as a series of discrete impacts. When the particle size is larger than λ, air appears to the particle as a continuum. In the two cases particles are said to be in the kinetic and continuum regime, respectively. The particle size range intermediate is called the transition regime. Mass transfer in the transition regime has been treated by several investigators (see Seinfeld and Pandis, 1998). The flux of condensing gas to a particle of radius r that applies to both kinetic and continuum regimes can be expressed by (Fuchs, 1959):

$$C_{cond} = -\frac{4\pi D_m r}{\frac{4D_m}{\alpha v r} + \frac{r}{r+\Delta}}(C_\infty - C_s) \quad (1.12)$$

where D_m is the diffusion coefficient and v the mean thermal velocity of the gas molecules, respectively, Δ is the distance from the particle surface within which the kinetic theory applies, and C_∞ and C_s are the gas phase concentration and the concentration of the gas at the particle surface. The accommodation coefficient α is a parameter that accounts for the fraction of molecules that impinges on the droplet and sticks to it, therefore $0 \leq \alpha \leq 1$. The accommodation coefficient depends on the condensing gas and the particle composition. Several values of Δ have been proposed, including $\Delta = 0$ and $\Delta = \lambda$, where λ is the mean free path of a gas molecule (Vignatti, 1999).

1.3. Conclusion

In this chapter, we described the main properties of aerosol particles, and different modeling approaches for their consideration in chemistry-transport models. We have seen that the aerosol particles suspended in the atmosphere are a complex multiphase entity, resulting from a large number of emission sources and atmospheric processes. Each element of this heterogeneous mixture is characterized by a state, chemical composition, particle size and dynamics of change in the atmosphere. This diversity of composition and size gives them the microphysical properties, making them difficult to measure and to take them into account in models. The aerosol modeling requires continuous progress in understanding and parameterization of the processes governing the evolution of aerosols. Many models have been developed for continental and regional scales to allow monitoring and study of particles involved in air quality. They nevertheless contain numerous uncertainties and must be continuously improved and validated using measurements.

In the following chapter it will be described the principal models involved in the calculations made during this thesis.

Chapter 2. The description of the meteorological model and the chemical transport model

The air quality at the regional scale is controlled by large-scale phenomena, as the synoptic weather situation or the contributions of air masses originating from long-range transport, and from phenomena at the small scale. To simulate air quality in these scales, a system of multi-scale modeling of atmospheric dynamics is essential. The principle of such a calculation is to solve the physics equations on grids for large scale areas and to use finer grids in areas of interest. This calculation involves the use of a certain number of nested grids in order to obtain a finer grid resolution. The Weather Research and Forecast model (WRF) was developed for this purpose. The nesting mode can be used one way or two-way for a large number of grid levels.

2.1. The WRF model

The Weather Research and Forecasting (WRF) model is a numerical weather prediction (NWP) and atmospheric simulation system designed for both research and operational applications.
WRF is a portable code that can be run in computing environments ranging from parallel supercomputers to laptops. WRF is maintained and supported as a community model to facilitate wide use internationally, and used for applications across scales ranging from large-eddy to global simulations. Such applications include real-time weather prediction, data assimilation development and studies, parameterized-physics research, regional climate simulations, air quality modeling, atmosphere-ocean coupling, and idealized simulations. The principal components of the WRF system are depicted in Figure 2.1. The WRF Software Framework (WSF) provides the infrastructure that accommodates the dynamics solvers, physics packages that interface with the solvers, and programs for initialization.

There are two dynamics solvers in the WSF: the Advanced Research WRF (ARW) solver (originally referred to as the Eulerian mass or “em” solver) developed primarily at NCAR, and the NMM (Non-hydrostatic Mesoscale Model) solver developed at NCEP.

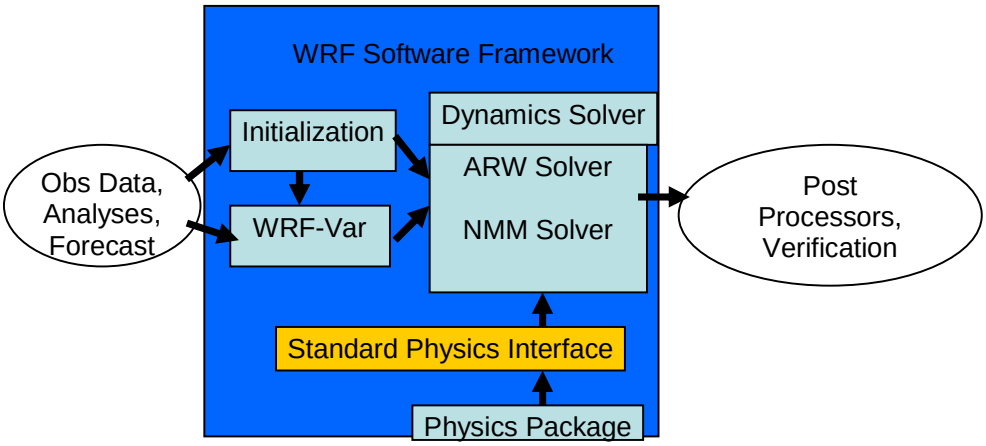

Figure 2.1. Major Features of the ARW System, Version 3

2.1.1. Dynamical equations

In developing the Eulerian prototypes, it was followed Ooyama’s (1990) philosophy of formulating the prognostic equations in terms of variables that have conservation properties for both the height and mass coordinates. The resulting models conserve mass, dry entropy and scalars to machine round-off; exact momentum conservation is sacrificed for the efficiency of the split-explicit acoustic mode integration scheme. The primary difference in the Eulerian prototypes is the vertical coordinate, and the practical differences following from this are that the mass coordinate surfaces move whereas the height coordinate surfaces are fixed, and the upper boundaries conditions differ the height coordinate model uses a rigid upper lid and the mass coordinate model uses constant pressure.

2.1.2. Height coordinate

In the height coordinate model, the conservative form for the wind V and potential temperature Θ can be defined as

$$V = \rho v = (U,V,W),\ \Theta = \rho\theta \qquad (2.1)$$

and prognostic non-hydrostatic equations in conservative form without terrain are

$$\frac{\partial U}{\partial t} + \nabla \cdot (vU) + \gamma R\pi \frac{\partial \Theta'}{\partial x} = F_U \tag{2.2}$$

$$\frac{\partial V}{\partial t} + \nabla \cdot (vV) + \gamma R\pi \frac{\partial \Theta'}{\partial y} = F_V \tag{2.3}$$

$$\frac{\partial W}{\partial t} + \nabla \cdot (vW) + \gamma R\pi \frac{\partial \Theta'}{\partial z} - g\left(\bar{\rho}\pi'/\bar{\pi} - \rho'\right) = F_W \tag{2.4}$$

$$\frac{\partial \Theta}{\partial t} + \nabla \cdot (v\Theta) = F_\Theta \tag{2.5}$$

$$\frac{\partial \rho'}{\partial t} + \nabla \cdot V = 0 \tag{2.6}$$

v = (u, v,w) are the covariant velocities in the two horizontal and vertical directions, respectively. Θ is the potential temperature. F_U, F_V, F_W, *and* F_Θ represent forcing terms arising from model physics, turbulent mixing, spherical projections, and the earth's rotation. Perturbation variables are defined as deviations from a time invariant hydrostatically balanced reference state such that $p = \bar{p}(z) + p'$, $\rho = \bar{\rho}(z) + \rho'$ and $\Theta = \bar{\rho}(z)\bar{\theta}(z) + \Theta'$. g is the acceleration due to gravity, $\gamma = c_p / c_v = 1.4$ is the ratio of the heat capacities for dry air. In arriving at this formulation, the following relation was used

$$\nabla p = \gamma R\pi \nabla \Theta \tag{2.7}$$

and pressure was obtained from the diagnostic equation of state

$$p = p_o \left(\frac{R\Theta}{p_o}\right)^\gamma . \tag{2.8}$$

2.1.3. Mass coordinate

The ARW equations are formulated using a terrain-following hydrostatic-pressure vertical coordinate denoted by η and defined as

$$\eta = (p_h - p_{ht})/\mu \qquad \text{where } \mu = p_{hs} - p_{ht} \tag{2.9}$$

p_h is the hydrostatic component of the pressure, and p_{hs} and p_{ht} refer to values along the surface and top boundaries, respectively.

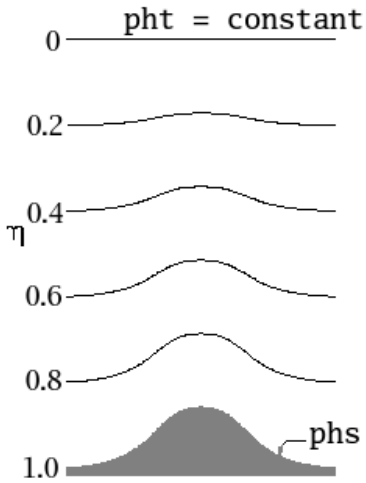

Figure 2.2. ARW η coordinate

The coordinate definition, proposed by Laprise (1992), is the traditional σ coordinate used in many hydrostatic atmospheric models. η varies from a value of 1 at the surface to 0 at the upper boundary of the model domain. This vertical coordinate is also called a mass vertical coordinate. Since $\mu(x, y)$ represents the mass per unit area within the column in the model domain at (x, y), the appropriate flux form variables are

$$V = \mu v = (U,V,W), \ \Omega = \mu \dot{\eta}, \ \Theta = \mu\theta. \tag{2.10}$$

v = (*u*, *v*,*w*) are the covariant velocities in the two horizontal and vertical directions, respectively, while $\omega = \dot{\eta}$ is the contravariant 'vertical' velocity. Θ is the potential temperature. Also appearing in the governing equations of the ARW are the non-conserved variables $\varphi = gz$ (the geopotential), p (pressure), and $\alpha = 1/\rho$ (the inverse density).

Using these variables, the equations (2.2 – 2.6) can be written in terms of the prognostic equations:

$$\frac{\partial U}{\partial t} + (\nabla \cdot vU)_\eta + \mu\alpha\frac{\partial p}{\partial x} + \frac{\partial p}{\partial \eta}\frac{\partial \phi}{\partial x} = F_U \tag{2.11}$$

$$\frac{\partial V}{\partial t} + (\nabla \cdot vV)_\eta + \mu\alpha\frac{\partial p}{\partial y} + \frac{\partial p}{\partial \eta}\frac{\partial \phi}{\partial y} = F_V \tag{2.12}$$

$$\frac{\partial W}{\partial t} + (\nabla \cdot vW)_\eta - g\left(\frac{\partial p}{\partial \eta} - \mu\right) = F_W \tag{2.13}$$

$$\frac{\partial \Theta}{\partial t} + (\nabla \cdot v\Theta)_\eta = F_\Theta \tag{2.14}$$

$$\frac{\partial \mu}{\partial t} + (v \cdot \nabla\phi)_\eta = 0 \tag{2.15}$$

$$\frac{\partial \phi}{\partial t} + (v \cdot \nabla\phi)_\eta = gw \tag{2.16}$$

together with the diagnostic hydrostatic pressure equation

$$\frac{\partial \phi}{\partial \eta} = -\mu\alpha \tag{2.17}$$

and gas law

$$p = \left(\frac{R\Theta}{p_0\mu\alpha}\right)^\gamma . \tag{2.18}$$

Further information concerning the dynamical equations and the numerical methods used in the Eulerian models can be found at http://www.mmm.ucar.edu/wrf/users/docs/arw_v3.pdf.

2.1.4. Turbulent transport in PBL

Turbulent transport in the PBL is using the mixture to non-local gradient described in Hong and Pan (1996). Figure 2.3 shows a typical profile of the coefficient of turbulent mixing in the atmospheric boundary layer.

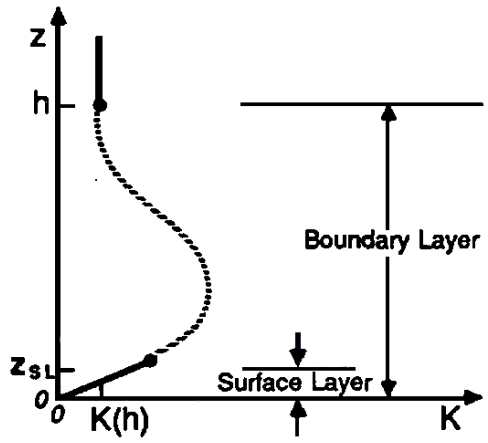

Figure 2.3. Typical variation of eddy viscosity K with height in the boundary layer proposed by O'Brien (1970). Adopted from Stull (1988). h is the height of PBL, z_{SL} is the height of surface layer.

According to Deardorff (1972), Troen and Mahrt (1986), Holtslag and Moeng (1991), and Holtslag and Boville (1993), the turbulent diffusion equations for prognostic variables (C; u, v, θ, q) can be expressed by

$$\frac{\partial C}{\partial t} = \frac{\partial}{\partial z}\left[K_c \left(\frac{\partial C}{\partial z} - \gamma_c \right) \right], \tag{2.19}$$

where K_c is the eddy diffusivity coefficient and γ_c is a correction to the local gradient that incorporates the contribution of the large-scale eddies to the total flux. This correction applies to θ and q in the mixed boundary layer.

As in Troen and Mahrt (1986), Holtslag et al. (1990), and Holtslag and Boville (1993), the momentum diffusivity coefficient is formulated as

$$K_{zm} = k w_s z \left(1 - \frac{z}{h}\right)^p , \tag{2.20}$$

where p is the profile shape exponent, k is the von Karman constant, z is the height from the surface, and h is the height of the PBL. The mixed-layer velocity scale is represented as

$$w_s = u_* \phi_m^{-1}, \tag{2.21}$$

where u_* is the surface frictional velocity scale and ϕ_m is the wind profile function evaluated at the top of the surface layer. The non-local gradient (or countergradient) term is given by

$$\gamma_c = b \frac{\overline{(w'c')}}{w_s}, \tag{2.22}$$

where $\overline{(w'c')}$ is the corresponding surface flux for θ and q, and b is a coefficient of proportionality. To satisfy the compatibility between the surface-layer top and the bottom of the PBL, the profile functions ϕ_m and ϕ_t is identical to those used in surface-layer. For the unstable and neutral conditions ($\overline{(w'\theta')} \le 0$),

$$\phi_m = \left(1 - 16 \frac{0.1h}{L}\right)^{-1/4} , \text{ for } u \text{ and } v \tag{2.23}$$

$$\phi_t = \left(1 - 16 \frac{0.1h}{L}\right)^{-1/2} , \text{ for } \theta \text{ and } q \tag{2.24}$$

while for the stable regime ($\overline{(w'\theta')} > 0$)

$$\phi_m = \phi_t = \left(1 + 5\frac{0.1h}{L}\right), \tag{2.25}$$

where h is the boundary layer height, and L is the Monin-Obukhov length scale. The top of surface layer is estimated as 0.1h. After Troen and Mahrt (1986) and Holtslag et al. (1990), the calculation of b leads at b=7.8. The boundary layer heights is given by

$$h = Rib_{cr}\frac{\theta_{virt}\left|U(h)\right|^2}{g(\theta_v(h) - \theta_s)}, \tag{2.26}$$

Where Rib_{cr} is the critical bulk Richardson number, $U(h)$ is the horizontal wind speed at h, θ_{virt} is the virtual potential temperature at the lowest model level, $\theta_v(h)$ is the virtual temperature at h, and θ_s is the appropriate temperature near the surface.

The eddy diffusivity for temperature and moisture (K_z) is computed from K_{zm} by using the Prandtl number taken constant within whole mixed boundary layer

$$\Pr = \left(\frac{\phi_t}{\phi_m} + bk\frac{0.1h}{h}\right). \tag{2.27}$$

Numerically, the boundary layer height, h, is obtained iteratively from previous relations.

2.1.5. Land-surface parameterization

The land-surface models (LSMs) use atmospheric information from the surface layer scheme, radiative forcing from the radiation scheme, and precipitation forcing from the microphysics and convective schemes, together with internal information on the land's state variables and land-surface properties, to provide heat and moisture fluxes over land points and sea-ice points. These fluxes provide a lower boundary condition for the vertical transport done in the PBL schemes (or the vertical diffusion scheme in the case where a PBL scheme is not run, such as in large-eddy mode). The land-surface models have various degrees of sophistication in dealing with thermal and moisture fluxes in multiple layers of the soil and also may handle vegetation, root, and

canopy effects and surface snow-cover prediction. The land-surface model provides no tendencies, but does update the land's state variables which include the ground (skin) temperature, soil temperature profile, soil moisture profile, snow cover, and possibly canopy properties. There is no horizontal interaction between neighboring points in the LSM, so it can be regarded as a one-dimensional column model for each WRF land grid-point, and many LSMs can be run in a stand-alone mode.

Turbulent parameterization described before is coupled in the model with the Noah LSM, which is the successor of the OSU LSM described by Chen and Dudhia (2001). The scheme is a unified code for research and operational purposes. This is a 4-layer soil temperature and moisture model with canopy moisture and snow cover prediction. We used the Noah LSM because additionally predicts soil ice and fractional snow cover effects, has an improved urban treatment, and considers surface emissivity properties, which are all new since the OSU scheme.

2.1.5.1. Thermodynamics of the LSM model

The surface skin temperature is determined following Mahrt and Ek (1984) by applying a single linearized surface energy balance equation representing the combined ground-vegetation surface. The ground heat flux is controlled by the diffusion equation for soil temperature (T):

$$C(\Theta)\frac{\partial T}{\partial t} = \frac{\partial}{\partial z}\left[K_t(\Theta)\frac{\partial T}{\partial z} \right], \tag{2.28}$$

where the volumetric heat capacity, C, and the thermal conductivity, K_t, are formulated as functions of volumetric soil water content, Θ is the fraction of unit soil volume occupied by water.

The layer-integrated form of eq 2.29 for the ith soil layer is:

$$\Delta z_i C_i \frac{\partial T_i}{\partial t} = \left(K_t \frac{\partial T}{\partial z} \right)_{zi+1} - \left(K_t \frac{\partial T}{\partial z} \right)_{zi} \tag{2.29}$$

The prediction of Ti is performed using the Crank–Nicholson scheme. The temperature at the lower boundary, assumed to be 3 m below the ground surface, is specified by the annual mean

surface air temperature. This also implies that the total soil column in the current LSM cannot exceed 3 m, although the number of layers is not limited.

2.1.5.2. Model hydrology

In the hydrology model, the prognostic equation for the volumetric soil moisture content (Θ) is

$$\frac{\partial \Theta}{\partial t} = \frac{\partial}{\partial z}\left(D\frac{\partial \Theta}{\partial z} \right) + \frac{\partial K}{\partial z} + F_{\Theta} \tag{2.30}$$

where both the soil water diffusivity D and hydraulic conductivity K are function of Θ, and F_{Θ} represents sources and sinks (i.e. precipitation, evaporation, and runoff) for soil water.

The total evaporation, E, is the sum of 1) the direct evaporation from the top shallow soil layer, E_{dir}; 2) evaporation of precipitation intercepted by the canopy, E_c; and 3) transpiration via canopy and roots, E_t. That is, $E=E_{dir}+E_c+E_t$.

The direct evaporation from the ground surface is done by

$$E_{dir} = (1-\sigma_f)\beta E_p \text{ and } \beta = \frac{\Theta_1 - \Theta_w}{\Theta_{ref} - \Theta_w}, \tag{2.31}$$

Where E_p is the potential evaporation, Θ_{ref} and Θ_w are the field capacity and wilting point, and σ_f is the green vegetation fraction.

The wet canopy evaporation and canopy evapo-transpiration are determined by

$$E_c = \sigma_f E_p \left(\frac{W_c}{S} \right)^n \text{ and } E_t = \sigma_f E_p B_c \left[1 - \left(\frac{W_c}{S} \right)^n \right], \tag{2.32}$$

where W_c is the intercepted canopy water content, S is the maximum canopy capacity (chosen here to be 0.5mm), B_c is a function of canopy resistance, and $n=0.5$.

2.1.5.3. Snow and sea-ice model

Because the LSM scheme is designed for application over a continental scale and should be able to deal with various surface characteristics, a simple snow and sea-ice model is included. The snow model has only one layer of snow cover and simulates the snow accumulation, sublimation, melting, and heat exchange at snow–atmosphere and snow–soil interfaces. The precipitation is categorized as snow when the temperature in the lowest atmospheric layer is below 0^0C. The model estimates the heat flux G between the soil and the snow by

$$G = K_{snow} \frac{T_s - T_{soil}}{D_{snow}}, \tag{2.33}$$

where K_{snow} is the thermal diffusivity for snow, T_s is the "skin" temperature, T_{soil} the temperature in the first soil layer, and D_{snow} the physical snow depth that is assumed to be 10 times the water-equivalent snow depth.

Still, there are several weaknesses in this simple snow model: 1) uniform snow cover over a given grid cell, 2) only one layer of snow, 3) constant thermal diffusivity for snow, and 4) no consideration of snow age and porosity.

2.1.6. Soil module

The WRF model's soil module is using parameters tabulated by type of occupation of land and season: winter or summer. The land uses 24 classes defined by the USGS.

2.1.7. Lateral boundary conditions

Due to the nesting capability of WRF, boundary conditions for the outmost domain as well as for the nested domain are needed. The calculation for the outmost domain is forced using meteorological data from global models of type AVN or ECMWF. Using these data to the edges of the computational domain is performed with a relaxation type boundary condition. There are two uses of the specified boundaries in the ARW: for the outer-most coarse grid or for the time-dependent boundaries supplied to a nested grid. The specified lateral boundary conditions for the

nest are automatically selected for all of the fine grids, even if the coarse grid is using combinations of the symmetry, periodic, or open options. If the specified lateral boundary condition is selected for the coarse grid, then all four grid sides (west, east, north, and south) use specified lateral conditions.

The coarse grid specified lateral boundary is comprised of both a specified and a relaxation zone (as shown in Fig. 2.4). For the coarse grid, the specified zone is determined entirely by temporal interpolation from an external forecast or analysis. The width of the specified zone is run-time configurable, but is typically set to 1 (i.e., the last row and column along the outer edge of the coarsest grid is entirely specified by temporal interpolation using data from an external model). The second region of the lateral boundary for the coarse grid is the relaxation zone. The relaxation zone is where the model is nudged or relaxed towards the large-scale forecast (e.g., rows and columns 2 through 5 in Fig.2.4). The size of the relaxation zone is a run-time option.

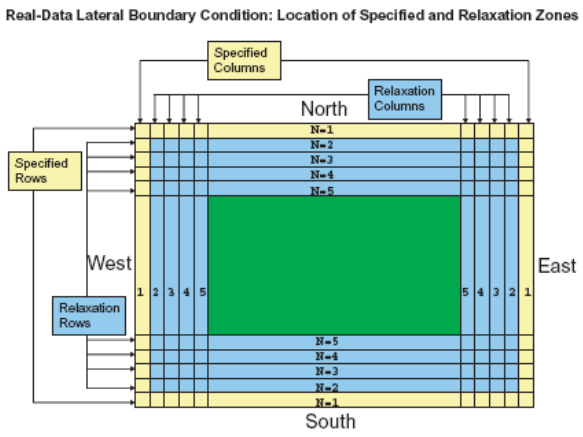

Figure 2.4. Specified and relaxation zones for a grid with a single specified row and column, and four rows and columns for the relaxation zone. These are typical values used for a specified lateral boundary condition for a real-data case.

The specified lateral boundary condition for the coarse grid requires an external file, generated during the same pre-processing as the initial condition file. Let ψ be any prognostic value having a lateral boundary entry, after Davies and Turner (1977),

$$\partial_t \psi\big|_n = F_1(\psi_{LS} - \psi) - F_2\Delta^2(\psi_{LS} - \psi) \qquad (2.34)$$

where n is the number of grid points in from the outer row or column along the boundary (*SpecZone + 1* $\leq n \leq$ *SpecZone + RelaxZone - 1*; see Fig.) and ψ_{LS} is the large-scale value obtained by spatial and temporal interpolation from the external analysis or model forecast by WPS . Δ^2 is a 5-point horizontal smoother applied along η-surfaces. The weighting function coefficients F_1 and F_2 are given by

$$F_1 = \frac{1}{10\Delta t}\frac{SpecZone + \mathrm{Re}laxZone - n}{\mathrm{Re}laxZone - 1} \tag{2.35}$$

$$F_2 = \frac{1}{50\Delta t}\frac{SpecZone + \mathrm{Re}laxZone - n}{\mathrm{Re}laxZone - 1} \tag{2.36}$$

where n extends only through the relaxation zone (*SpecZone + 1* $\leq n \leq$ *SpecZone + RelaxZone – 1*). F_1 and F_2 are linear ramping functions with a maximum at the first relaxation row or column nearest the coarse grid boundary (just inside of the specified zone).

On the coarse grid, the specified boundary condition applies to the horizontal wind components, potential temperature, ϕ', $\mu_d^{'}$ and water vapor. The lateral boundary file contains enough information to update the boundary zone values through the entire simulation period.

2.1.8. Nesting

The ARW supports horizontal nesting that allows resolution to be focused over a region of interest by introducing an additional grid (or grids) into the simulation. In the current implementation, only horizontal refinement is available: there is no vertical nesting option. The nested grids are rectangular and are aligned with the parent (coarser) grid within which they are nested. This nesting implementation is in many ways similar to the implementations in other mesoscale and cloudscale models (e.g. MM5, ARPS, COAMPS).

Nested grid simulations can be produced using either 1-way nesting or 2-way nesting. The 1-way and 2-way nesting options refer to how a coarse grid and the fine grid interact. In both the 1-way and 2-way simulation modes, the fine grid boundary conditions (i.e., the lateral boundaries) are interpolated from the coarse grid forecast. In a 1-way nest, this is the only information exchange between the grids (from the coarse grid to the fine grid). In the 2-way nest integration, the fine

grid solution replaces the coarse grid solution for coarse grid points that lie inside the fine grid. This information exchange between the grids is now in both directions (coarse-to-fine for the fine-grid lateral boundary computation and fine-to-coarse during the feedback at each coarse-grid time step).

2.2. The CHIMERE model

2.2.1. Model description

The CHIMERE multi-scale model is primarily designed to produce daily forecasts of ozone, aerosols and other pollutants and make long-term simulations for emission control scenarios. CHIMERE runs over a range of spatial scales from the urban scale to the regional scale with resolutions from 1-2 km to 100 km.

CHIMERE proposes many different options for simulations which make it also a powerful research tool for testing parameterizations, hypotheses. It can run with several vertical resolutions, and with a wide range of complexity. It can run with several chemical mechanisms, simplified or more complete, with or without aerosols.

The CHIMERE regional modeling system based on the meteorological fields of WRF is capable, in theory, to be used anywhere over the world with mesh ranging from 1 km to several of kilometers. CHIMERE was developed primarily as an operational model equipped with numerical optimization to reduce the computation time.

The CHIMERE model was developed by the scientists of IPSL/LMD (l'Institut Pierre Simon Laplace/Le Laboratoire de Météorologie Dynamique), INERIS (Institut National de l'Environnement Industriel et des Risques), LISA (Laboratoire Inter-universitaire des Systèmes Atmosphériques). First version has developed in 1997 as a box model version for Paris area. It was continuously developed, thus was introduced: in 1999 the cartesian grid (over Europe), in 2000 the adjoint version and inverse modeling of surface emissions fluxes, in 2004 the aerosol module, in 2005 the first version of CHIMERE-dust, in 2007 the deep convection and a new deposition scheme (http://www.lmd.polytechnique.fr/~menut/documents/200909-chimere-formation-menut.pdf).

2.2.2. The modeling principle

CHIMERE is a three-dimensional chemistry-transport model based on an Eulerian advection scheme. It calculates the spatio-temporal evolution of concentrations of many gaseous species and particulates at each grid point. The dynamic equation describing the evolution of the k species, having Q_k concentration, at time t is given by the equation 2.37:

$$\begin{aligned}
\frac{\partial Q_k(x,t)}{\partial t} &= -div\left[u(x,t)Q_k(x,t)\right] && \text{advection}\\
&+div\left[K(x,t)\nabla Q_k(x,t)\right] && \text{turbulent transport}\\
&+V_d(x,t)\nabla Q_k(x,t) && \text{deposition}\\
&+\chi_k(T,L,I,x,t) && \text{chemical sources/sink}\\
&+E_k(x,t) && \text{emissions}\\
&+\left[\partial Q_k(x,t)/\partial t\right] && \text{aerosol physics and chemistry}
\end{aligned} \qquad (2.37)$$

where x is the vector defining the position on considered grid, u is the wind speed vector, K the eddy diffusivity tensor, T the temperature, L the liquid water content, I the photolysis rate. Different terms of production and loss are present in this equation related to transport, chemical reactions, emission, deposition and aerosol dynamics.

2.2.3. Meteorological input data

The CHIMERE model requires multiple weather variables as input data, such as surface pressure, horizontal wind, temperature, specific humidity, liquid water content and precipitation. These data may come from different numerical weather prediction models as for example from the ECMWF model (European Centre for Medium-Range Weather Forecasts), with a resolution of 0.25 degree, but also results from the mesoscale model WRF can be used.

We used data from the WRF model, better suited to applications at the regional scale because of their higher spatial resolution. Thus, the meteorological simulations are conducted on the

principle of two-way interaction (two-way nesting) on three nested grids, respectively 45 km, 9km and 3 km resolution. The data are then linearly interpolated on the CHIMERE model grid.

2.2.4. The horizontal transport

The horizontal transport is treated using the numerical scheme of order 3 PPM (Parabolic Piecewise Method) developed by Colella and Woodward (1984), which has the advantage of conserving the mass and to be very little diffusive. However, it is quite expensive in computing time. For this reason, only slow species are transported with this scheme, the others being transported with the classic "upstream" of order 1. In the case of aerosols, this last pattern is used to transport its various compounds.

2.2.5. Vertical transport and turbulent diffusion

The vertical transport is calculated to offset the convergence or divergence of horizontal mass flux. Thus, when the surface layer mass balance is positive (more incoming air masses than outgoing), an upward vertical wind is created between the surface layer and the next layer. This new vertical transportation is integrated into the mass balance of the next layer and the process is repeated until the top of the model, where the pollutants are removed permanently or imported from the free troposphere. This method has the advantage of conserving the mass and creating a vertical transport consistent with the horizontal one.

Vertical transport is also caused by turbulence in the boundary layer. The calculation of the vertical eddy diffusivity K is based on the parameterization of Troen and Mahrt (1986). This approach allows to calculate the diffusivity profile $K(z)$ in each model column, using a scale factor w_s and the mixing height h:

$$K(z) = kw_s z(1 - z/h)^2 . \qquad (2.38)$$

The height of the boundary layer h can either be directly provided by the meteorological model (in the case of using WRF) or be recalculated in CHIMERE. In the latter case it is determined as the maximum height between the height obtained by the parameterization of Troen and Mahrt

(1986) based on the Richardson number (Ri = 0.5 threshold value) and that calculated in the convective case (Cheinet, 2002). It is also noted that the horizontal diffusion is neglected.

2.2.6. Chemical mechanism MELCHIOR

CHIMERE uses the mechanism MELCHIOR 2 which is a simplified version of MELCHIOR (Derognat et al., 1998). The following chemical species are managed by MELCHIOR 2:

- *inorganic compounds* (O_3-ozone, H_2O_2-hydrogen peroxide, OH-hydroxyl radical, HO_2-hydroperoxy radical, NO-nitric oxide, NO_2-nitrogen dioxide, NO_3-nitrogen trioxide, N_2O_5-dinitrogen pentoxide, HONO-nitrous acide, HNO_3-nitric acid, SO_2-sulfur dioxide);
- *hydrocarbon species* (CH_4-methane, C_2H_6-ethane, NC_4H_{10}-n-butane, C_2H_4-ethene, C_3H_6-propene, OXYL-o-xylene, C_5H_8–isoprene, APINEN-α-pinene, BPINEN-β-pinene, LIMONE–limonene, TERPEN–terpenes, HUMULE–Humulene, OCIMEN–Ocimene);
- *carbonyls* (HCHO-formaldehyde, CH_3CHO-acetaldehyde, CH_3COE-methyl ethyl ketone, GLYOX–glyoxal, MGLYOX-methyl glyoxal, CH_3COY-dimethyl glyoxal, MEMALD-unsaturated dicarbonyls, reacting like 4-oxo-2-pentenal, MVK-methyl vinyl ketone, MAC–methacroleine);
- *organic nitrates* (PAN-peroxyacetyl nitrate, CARNIT-nitrate carbonyl taken as α-nitrooxy acetone, ISNI -unsaturated nitrate from isoprene degradation);
- *organic peroxides* (CH_3O_2H-methyl hydroperoxide, PPA-peroxy acetyl acid);
- *(per)oxy radicals* (CH_3O_2-methyl peroxy radical, CH_3COO-peroxy acetyl radical);
- *operators* (oRO_2-representing peroxy radicals from OH attack to C_2H_5, $NCHH_{10}$, C_2H_4, C_3H_6, OXYL, CH_3COE, MEMALD, and MVK; oROOH representing organic peroxides from oRO_2+HO_2 reactions; obio representing peroxy radicals produced by C_5H_8 and APINEN+ OH reaction; obioH representing biogenic organic peroxides from obio+HO_2 and obio+obio reactions; oPAN representing PAN homologue compounds (except PAN); PANH representing results from oPAN+HO_2 reaction; toPAN representing results from oPAN+NO_2 reaction; oRN1 representing organic nitrate peroxy radicals from NO_3 attack to C_2H_4, C_3H_6, C_5H_8, APINEN, BPINEN, LIMONE, TERPEN, OCIMEN, HUMULE and OH attack to ISNI).

A number of 120 chemical reactions are involved in the calculation of concentrations of gaseous species using MELCHIOR 2 mechanism (http://www.lmd.polytechnique.fr/chimere/docs/CHIMEREdoc2011.pdf, p.103-107).

2.2.7. Emissions

The CHIMERE model requires the following representatively species: NO (nitrogen monoxide), NO_2 (nitrogen dioxide), HONO (nitrous acid), SO_2 (sulphur dioxide), NH_3 (ammoniac), CO (carbon monoxide), CH_4 (methane), C_2H_6 (ethane), NC_4H_{10} (n-Butane), C_2H_4 (ethene), C_2H_6 (ethane), C_3H_6 (propene), C_5H_8 (isoprene), OXYL (o-Xylene), HCHO (formaldehyde), CH_3CHO (acetaldehyde), CH_3COE (methyl ethyl Ketone), APINEN (α-pinene), PPM_fin (primary particulate matter), PPM_coa (primary particulate matter), PPM_big (primary particulate matter), H2SO4_fin (primary sulfuric acid), BaP_fin (benzo(a)pyrene), BbF_fin (benzo(b)fluoranthene), BkF_fin (benzo(b)fluoranthene), OCAR_fin (primary organic carbon), BCAR_fin (primary black carbon) from an emission database representing main gaseous compounds and aerosols required by its chemical mechanism MELCHIOR.

The VOC emissions are calculated from the EMEP emission database

- 8 primary VOC's (explicit or family representatives): Methane, Ethane, N-butane, Ethene, Propene, Ortho-xylene, Isoprene, α-pinene;
- 12 (10) secondary VOC's (explicit or family representatives): Formaldehyde, Acetaldehyde, Methyl-ethyl-ketone, Glyoxal, Methyl-glyoxal, Dimethyl-glyoxal, 4-oxo-2-penatanal, 5-methyl-3H-furan-2-one, Methyl-vinyl-ketone, Methyl-acroleine, (Methanol), (Ethanol).

Then the VOC's are disaggregated into real compounds using a speciation profile (depending on activity sector). In the data provided on CHIMERE server, the VOC speciation comes from the British PORG speciation, which is public. The construction of model-species emissions then requires a type of aggregation procedure (Middleton et al., 1990). Each real VOC emissions are aggregated into one or several model VOC(s), with a branching coefficient and a reactivity-dependent coefficient (see the Middleton procedure), for which reactivities and molar masses for both the real and the model VOCs have to be known. In the British speciation, 227 real VOCs are considered, and the following AGGREGATION file gives these informations for the

MELCHIOR mechanism. Reactivities have been calculated on the basis of the Leeds University MCM Master Mechanism and the Kwok structure/reactivity approach. The SPECIATION files gives the VOCs list and the 9-activity speciation, and the way VOCs are preprocessed in CHIMERE for continental scale.

It should be noted that the uncertainty in the spatial distribution of individual VOC emissions is large, given that the VOC profiles are assumed to be the same all over Europe, with the exception of traffic, where national differences (e.g. the ratio gasoline / diesel) are taken into account. Monthly, daily and hourly variations of the emissions are modeled by imposing respective variations from the (Society, 1994) data base.

2.2.7.1. Anthropogenic emission

Anthropogenic emissions are the different compounds: PM2.5, PM10-2.5, NOx, CO, SO2, NH3 and non-methane volatile organic compounds (including ethane, n-butane, ethane, isoprene, formaldehyde, acetaldehyde). Annual data of anthropogenic emissions for these components are taken from the EMEP data base (Vestreng, 2003) web site (www.emep.int). The data are spatially interpolated from the EMEP grid into CHIMERE grid.

2.2.7.2. Biogenic emissions

Using the data and parameterization from the MEGAN model (Guenther et al., 2006) six of CHIMERE species are calculated: isoprene, α-pinene, β-pinene, limonene, ocimene and NO. Estimates of biogenic VOC's from vegetation and NO emissions are calculated as

$$ER_i = EF_i \times \gamma_{T,i} \times \gamma_{PPFD} \times \gamma_{LAI} \quad (2.39)$$

where ER_i ($\mu g\ m^{-2}\ h^{-1}$) is the emission rate of species i, EF_i ($\mu g\ m^{-2}\ h^{-1}$) is an emission factor at canopy standard conditions, and γ_i (unitless) is an emission activity factor that accounts for deviations from canopy standard conditions. The canopy standard conditions relevant for this study are defined as: air temperature (T) of 303 K, photosynthetic photon flux density (PPFD) of 1500 μmol m^{-2} s^{-1} at the top of the canopy, leaf area index (LAI) of 5 m^2 m^{-2} and a canopy with 80% mature, 10% growing and 10% old foliage (Bessagnet et al., 2009).

In rural areas, NO emissions from microbial processes or soil fertilizer application are also taken into account. Since these emissions strongly depend on temperature, they are processed in the model as biogenic emissions (Stohl et al., 1996).

2.2.7.2. Natural emissions

Other emission processes of particles can also be taken into account, such as mineral dust emissions by local erosion of soil or the raising of particles deposited under the action of wind and turbulence. A simplified parameterization of these processes has recently been introduced in the CHIMERE model by Vautard et al. (2005). These emissions are directly dependent on weather conditions and are calculated based on wind speed and soil parameters. Thus, the flow of particles (g m^{-2} s^{-1}) issued by erosion is given by equation (White 1986):

$$F = \alpha C u_{*_s} (u_{*_s}^2 - u_{*_t}^2) \tag{2.40}$$

where u_{*_s} is the saltation friction velocity, u_{*_t} is the threshold friction velocity, C is a coefficient that may depend on several surface factors and α is the sandblasting efficiency.
The flux of particles produced by the resuspension processes is given by the equation (2.41) (Vautard et al. 2005)

$$F = Pf(w)u_*^{1.43} \tag{2.41}$$

where *f(w)* is a function of soil water content, and *P* a constant adjusted to compensate missing mass of PM_{10}.
Sea salt emissions are calculated using formula given by Monahan, 1986:

$$\frac{dF}{dr} = 1.373 U_{10}^{3.41} r^{-3} (1 + 0.057 r^{1.05}) 10^{1.19 e^{-B^2}} \tag{2.42}$$

$$B = \frac{0.38 - \log(r)}{0.65} \tag{2.43}$$

where F is the flux of sea salt particle number in particles m^{-2} s^{-1} μm^{-1}, r the particle radius in μm and U_{10} is the wind speed at 10 m in m s^{-1}.

2.2.8. Dry deposition

Dry deposition may be defined as the transport of particulate and gaseous contaminants from the atmosphere onto surfaces in the absence of precipitation (Davidson and Wu, 1989). Therefore, dry deposition of gases and particles is an intermediary transport process responsible for the removal of pollutants from the atmosphere.

For many compounds, dry deposition can be as important as wet deposition as a removal process. Due to the difficulty in making direct measurements of dry deposition and the need for a suitable model parameterization, dry deposition is often treated as a first-order removal mechanism, where the flux of a pollutant to the surface is the product of a characteristic deposition velocity and its concentration in the "surface layer" (i.e., the lowest model layer).

Dry deposition is affected by the following major factors:

(a) Meteorological variables (e.g., wind speed, temperature, terrain, atmospheric stability, and humidity).

(b) Surface variables (e.g., surface aerodynamic roughness and structure, pH, surface charge, hydrophobicity, porosity)

(c) Properties of the depositing material (e.g., chemical reactivity, solubility, diameter, surface charge, and shape).

Dry deposition is considered for model gas species i and is parameterized as downward flux

$$F_{d,i} = -v_{d,i} c_i \tag{2.44}$$

where $F_{d,i}$ represents the vertical dry deposition flux, $v_{d,i}$ – deposition velocity and c_i concentration of species i.

The deposition velocity is described through a resistance analogy (Wesely, 1989):

$$v_{d,i} = \frac{1}{R_a + R_b + R_c}, \quad (2.45)$$

where R_a is the aerodynamic resistance, R_b is the quasi-laminar layer resistance and R_c is the canopy resistance.

2.2.9. Aerosols

An aerosols module was introduced in the CHIMERE model by Bessagnet et al., (2004) to describe the spatio-temporal evolution of aerosol concentrations resulting from the emission process, transport, chemistry and particles microphysics.

2.2.9.1. Chemical composition and distribution of aerosols

To represent the aerosol population, the sectional (or bin) approach was considered in the model (Gelbard and Seinfeld 1980). It discretizes the density distribution in a finite number of bins (Warren, 1986). Thus, all particles in section (or bin) l having the same composition are characterized by their mean diameter d_l. The bins follow a geometrical progressions, $bins(n) = \sqrt{\text{int}(n) * \text{int}(n-1)}$, where $n \in (1,int)$ and $int(n+1)=int(n)*stepbin$, with $stepbin = (10^{-6}/10^{-8})^{1/(n\,\text{int}-1)}$, *nint* representing the modeled number of bins plus 1. For a given bin size x as $x = ln(m)$, with m the particle mass, $q(x)$ is the differential mass density distribution defined as:

$$q(x) = \frac{dQ}{dx} \quad (2.46)$$

where Q is the mass concentration function.

Q_l^k (μg m^{-3}) is the mass concentration of the chemical component k in section (or bin) l and Q_l (μg m^{-3}) is the total mass concentration in section l :

$$Q_l = \int_{xl-1}^{xl} q(x)dx = \sum_k Q_l^k \ . \qquad (2.47)$$

The atmospheric aerosols represented in the model are primary particulate matter, nitrate, sulfate, ammonium, biogenic secondary organic aerosol (SOA), anthropogenic SOA and water (Bessagnet et al., 2009).

2.2.9.2. Nucleation

The parameterization of (Kulmala et al., 1998) for sulfuric acid nucleation is used in the model by default. This process, favored by cold humid atmospheric conditions, affects the number of ultrafine particles. The nucleated particle mass is added to the smallest bin in the sectional distribution. In this study, a detailed analysis of the impact of the use of other nucleation schemes will be performed (see chapter 4).

2.2.9.3. Coagulation

Since Q_l^k is the mass concentration of component k in section l, the mass balance equation for coagulation (Gelbard and Seinfeld, 1980) follows

$$\left(\frac{dQ_l^k}{dt}\right)_{coag} = \frac{1}{2}\sum_{i=1}^{l-1}\sum_{j=1}^{l-1}\left[{}^{1a}\beta_{i,j,l}Q_j^k Q_i + {}^{1b}\beta_{i,j,l}Q_i^k Q_j\right]$$
$$-\sum_{i=1}^{l-1}\left[{}^{2a}\beta_{i,l}Q_i Q_j^k - {}^{2b}\beta_{i,l}Q_l Q_i^k\right]$$
$$-\frac{1}{2}{}^{3}\beta_{l,l}Q_l Q_l^k - Q_l^k\sum_{i=l+1}^{m}{}^{4}\beta_{i,l}Q_i \qquad (2.48)$$

The sectional coagulation coefficients ${}^{1a}\beta$, ${}^{1b}\beta$, ${}^{2a}\beta$, ${}^{2b}\beta$, ${}^{3}\beta$, and ${}^{4}\beta$ (Fuch, 1964) depend on particle characteristics and meteorological data such as temperature, pressure and turbulence parameters. For sub-micron particles, coagulation is essentially driven by Brownian motions. For coarse particles sedimentation is an efficient process.

2.2.9.4. Condensation

Secondary aerosols are often produced by atmospheric gases reacting and condensing, or by cooling vapor condensation (gas to particle conversion). Fine aerosol particles (less than 1 mm in radius) originate almost exclusively from condensation of precursor gases. A key precursor gas is sulfuric acid (H_2SO_4), which is produced in the atmosphere by oxidation of sulfur dioxide (SO_2) emitted from fossil fuel combustion, volcanoes, and other sources. H_2SO_4 has a low vapor pressure over H_2SO_4-H_2O solutions and condenses under all atmospheric conditions to form aqueous sulfate particles. The composition of these sulfate particles can then be modified by condensation of other gases with low vapor pressure including NH_3, HNO_3, and organic compounds. Organic carbon represents a major fraction of the fine aerosol and is contributed mainly by condensation of large hydrocarbons of biogenic and anthropogenic origin.

As long as the partial pressure of a compound in the gas phase is higher than the vapor pressure of that compound in aerosol, growth will occur. Of course, the opposite situation is possible, where particles outgas certain compounds, but in the urban environment growth tends to be the dominant process. Condensational growth is another mechanism by which aerosol can leave the nucleation mode.

Seinfeld and Pandis (1998) derive an expression for particle diameter with respect to time for cases of condensation of out-gassing:

$$D_p^2 = D_{p0}^2 + 2At \tag{2.49}$$

where: D_p-particle diameter, D_{p0}-initial particle diameter, A-constant. The term A is, in fact, related to the driving force for the condensation, and is only constant in situations like persistent supersaturation of the gas phase species. The interesting point about the equation is that it predicts smaller particles will grow proportionally faster than large particles. In fact, Seinfeld and Pandis comment that it tends to produce monodisperse (one size) aerosol as $t \rightarrow \infty$.

2.2.9.5. Dry deposition

As for gases, according to Seinfeld and Pandis, 1998, dry deposition for aerosols also makes uses a resistance scheme and is expressed as it follows:

$$v_d = \frac{1}{r_a + r_b + r_a r_b v_s} + v_s \,. \qquad (2.50)$$

where v_s is the sedimentation velocity, r_a is the aerodynamic resistance, r_b is the quasi-laminar layer resistance and r_c is the canopy resistance

2.2.9.6. Wet deposition

Wet deposition is the predominant removal process for particles. Particles act as cloud condensation nuclei; the cloud droplets grow and collect into sufficiently large sizes to fall as precipitation. Particles that are entrained into the cloud or that exist below precipitating clouds, can also be directly scavenged by precipitation via accretion and impaction processes.

The rates of aerosol activation to cloud droplets and impaction depend upon the cloud type (e.g., prolonged stratiform vs. vigorous convective development), precipitation rate, and particle size distribution.

Wet deposition can also be an important removal process for relatively soluble gaseous pollutants and this occurs through the following series of steps:

- Mixing of trace gas and condensed water in common air space;
- Absorption of gas molecules by water droplets;
- Possible aqueous-phase reactions of the pollutant within water droplets;
- Precipitation of droplets to the earth's surface;
- Diffusion of ambient gases into falling precipitation.

It is important to note that each of the above steps may be reversible, so that the overall wet deposition rate for gases depends on the net results of the forward and backward processes at each step.

Nitric acid and ammonia in the gas phase are scavenged by cloud droplets. This process is assumed to be reversible. Moreover, for in-cloud scavenging, dissolved gases in a non precipitating cloud can reappear in the gas phase due to cloud dissipation. Equilibrium between dissolved gases concentration and gas-phase concentrations follows Seinfeld and Pandis (1998). Dissolution of gases in precipitating drops is assumed to be irreversible, both for HNO_3 and NH_3. The scavenging coefficient Γ is expressed as:

$$\Gamma = \frac{pD_g}{6.10^5 u_g D^2}\left(2 + 0.6R_e^{1/2} S_c^{1/3}\right), \qquad (2.51)$$

p being the precipitation rate (mm h^{-1}), D_g the molecular diffusion coefficient (m^2 s^{-1}), u_g the raindrop velocity (m s^{-1}), *Re* and *Sc* respectively the Reynolds and Schmidt numbers of drops. In the CHIMERE model, sulfur dioxide and hydrogen peroxide are also scavenged by precipitation. Particles in clouds can be scavenged either by coagulation (collection) with cloud droplets or by precipitating drops. Particles also act as cloud condensation nuclei to form new droplets. This latter process of nucleation is the most efficient one in clouds. According to Tsyro, 2002, and Guelle et al., 1998, the deposition rate is written as:

$$\left(\frac{dQ_l^k}{dt}\right)_{incl} = -\frac{\zeta_l p_r}{w_l h} Q_l^k \qquad (2.52)$$

with p_r being the precipitation rate released in the grid cell (g cm^{-2} s^{-1}), w_l the liquid water content (g cm^{-3}), h the cell thickness (cm) and ζ_l an empirical uptake coefficient (in the range 0-1) depending on particle composition.

Particles below the cloud are scavenged by raining drops, the deposition rate of particles being:

$$\left(\frac{dQ_l^k}{dt}\right)_{subcl} = -\frac{\alpha p E_l}{u_g} Q_l^k, \qquad (2.53)$$

with α being an empirical coefficient, p the precipitation rate in the grid cell (g cm^{-2} s^{-1}), E a collision efficiency coefficient between particles and raining drops (Loosmore and Cederwall, 2004) and u_g the falling drop velocity (cm s^{-1}).

2.3. Conclusion

This chapter has presented the WRF and the CHIMERE models, which are the main tools of this thesis. These models include parameterizations of complex physics and complex chemistry of atmospheric particles. We detailed these parameterizations. In the following chapter of this thesis, we will seek to evaluate and improve performance of these models by comparing the modeling results with observations from different atmospheric sites. Chapter 3 will present the validation by comparing the model simulations to results from an intensive measurement campaign realized from February 24 to March 8, 2009 at Puy de Dome site (45º 46' 15'' N; 2º 57' 50'' E, 1465 m a.s.l.) and with the measurements made in urban environments operated by Air Quality Measurement Networks (for the Clermont-Ferrand region: Atmo-Auvergne).

Chapter 3. The influence of the emissions database on the CHIMERE simulation results

Emission inventories have long been fundamental tools for air quality management. Emission estimates are important for developing emission control strategies, determining applicability of permitting and control programs, ascertaining the effects of sources and appropriate mitigation strategies, and a number of other related applications by an array of users, including local agencies, consultants, and industry.

With the increasing use of numerical atmospheric chemistry modeling on local, regional and global scales, the creation of inventories with wider coverage and analysis of the interaction among the various scales have become essential. In the past decades, various programs of international cooperation have emerged with the objective of providing integrated emission information on continental or global scales. To note are the EMEP (Co-operative Programme for Monitoring and Evaluation of the Long-Range Transmission of Air Pollutants in Europe e http://www.ceip.at/) in Europe, and the Global Emissions Inventory Activity (GEIA) from the International Global Atmospheric Chemistry Programme (http://www.geiacenter.org/).

The spatial and temporal resolution of the global inventories is normally low, and therefore does not capture the specific characteristics of each region, principally with respect to the representation of urban centers.

Emission data provide surface fluxes of gases and aerosols in the atmosphere due to man made activities (e.g. industry and traffic) and natural processes (e.g. dust, lightening, fires, volcanoes, biogenic VOC emissions etc.). However, the man made emissions are often emissions of the eco-system, which was subject to human activity such as agriculture and deforestation. Natural emissions (e.g. sea salt spray and wind blown dust) are often not given in total prescribed numbers but are modeled by means of parameterization (emission models) from input data such as wind and surface conditions. Emission data sets differ in many respects. The discrepancies are

due to different total numbers of chemical species, different selection of chemical species and breakdown of volatile organic compounds, different temporal and spatial resolution and variability, different selections of emitting processes, different injection heights and different, mostly not well documented methodologies.

In the following we will be analyze the influence of emissions databases by comparing on one side the anthropogenic gas emissions from the EMEP inventory (Vestreng, 2003) with spatial resolution of 50km with on the other side, the MACC European emissions with a horizontal resolution of 0.125°x0.0625° (Kuenen et al., 2011) for NOx, SO_2, NMVOC, CH_4, NH_3, CO, PM10 and PM2.5. The biogenic emissions are calculated using the MEGAN model data (Guenther et al., 2006).

The ability of the model to simulate real measurements is assessed using both emission databases by comparing the model simulations to results from an intensive measurement campaign driven from February 24 to March 8, 2009 at Puy de Dome site (45º 46' 15" N; 2º 57' 50" E, 1465 m a.s.l.). The measurements performed at high altitude are representative of horizontal scales which are larger than measurements performed within urban environments usually operated by Air Quality Measurement Networks (for the Clermont-Ferrand region: Atmo-Auvergne). However, measurements performed at high altitude on a mountain top might also be difficult to simulate due to more complex air mass dynamics at the vicinity of the mountain chain. Hence, we also chose to compare model simulations with lower altitude measurements within the Atmo-Auvergne measurement network at lower altitudes.

3.1. Measurement sites

Measurements were performed during an intensive campaign at Puy de Dome summit station, France, during February 24 – March 8, 2009 period. Due to its large elevation this site is mostly above the boundary layer during the winter season, when the temperature drops very low and the thermal convection is weak.

Aerosol particle size and compositions measurements were carried out using a Time of Flight Aerosol Mass Spectrometer and a Scanning Mobility Particle Sizer, which provide the size distribution and the source-apportioned chemical composition with high temporal resolution (of the order of the minute).

The Puy de Dome research station (PDD) is located at 1465m a.s.l. in the centre of France (see Fig. 3.1). The Puy de Dome itself is located in the center of a mountain range that extends from north to south, and is the first topographic barrier facing the prevailing winds from the west. The station is surrounded mainly by a protected area which is a part of the natural park of the volcanoes of Auvergne where fields and forests are predominant, the agglomeration of Clermont-Ferrand (300.000 inhabitants) being located 16 km East of the station. Meteorological parameters, including the wind speed and direction, temperature, pressure, relative humidity and radiation (global, UV and diffuse), and atmospheric trace gases (O_3, NOx, SO_2, CO) are monitored continuously throughout the year. Winter and summer temperatures vary typically from -10 to +10 ^{o}C and 5 to 25 ^{o}C respectively. Westerly and northerly winds are dominant. During the November-April period, the access road to the station is restricted preventing the measuring site from local contamination.

The PDD station is ideally situated at an altitude allowing to sample both the masses belonging to the boundary layer (mainly during the day), and air masses belonging to the free troposphere (mainly at night). In fact, it also allows a study of the interface between two layers of the atmosphere and processes associated with mixing of air masses of high and low pollutant concentrations that takes place. However, because of its topographical situation of the first barrier, the resort is very often cloudy (about 50% of the time throughout the year) (Venzac, 2009).

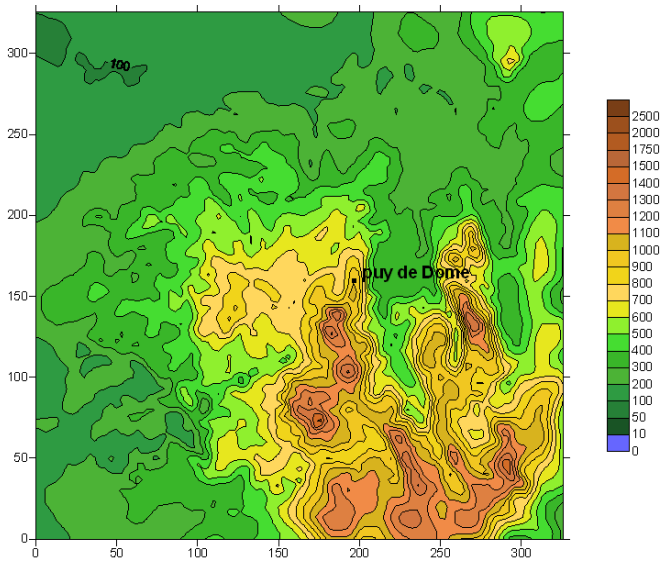

Figure 3.1. Topography associated with the PDD site

Measurements of several species inside the atmospheric boundary layer (BL) were also performed during this study. The BL sites used in this study are part of the Atmo-Auvergne (the regional air quality agency) surface network at which the following compounds are monitored: O_3, NOx, SO_2, PM10 and PM2.5. The BL sites characteristics are described in Table 3.1

During February 24 – March 8, 2009 period were measured 212 hourly values for gas-phase component and 79 hourly values for the aerosol-phase components at PDD summit. For BL sites we have 312 hourly values for all components. The differences results from periods with cloud events on PDD summit which were excluded from the observational data set.

Table 3.1. Atmo-Auvergne sites characteristics

Name	Type	Latitude	Longitude	Altitude	Sampling altitude	Measurements
Clermont - Gerzat	Peri-urban	45° 49' 25"	3° 08' 33"	325 m	3.5 m	NO NO_2 PM10 O_3
Clermont - Pardieu	Peri-urban	45° 45' 49"	3° 08' 06"	354 m	3 m	NO NO_2
Clermont - Montferrand	Urban	45° 47' 53"	3° 06' 48"	340 m	3.5 m	NO NO_2 SO_2 PM10 PM2.5 O_3
Clermont - Gare	Urban station	45°46'33"	3°05'46"	365 m	3 m	NO NO_2 SO_2 PM10 PM2.5
Clermont – Delille	Urban	45° 46' 54"	3° 05' 42"	365 m	3.5 m	NO NO_2 PM10 PM2.5 O_3
Clermont - Lecoq	Urban	45°46'20"	3°05'15"	390 m	5 m	NO NO_2 PM10 O_3
Clermont – Jaude	Urban	45° 46' 32	3° 04' 57"	385 m	15 m	NO_2 SO_2 O_3
Clermont – Royat	Peri-urban	45° 45' 53"	03° 02' 48"	525 m	4 m	NO NO_2 SO_2 O_3

The location of urban sites comparatively with PDD location and their location into the urban area of Clermont-Ferrand are shown in Fig. 3.2 (http://www.atmoauvergne.asso.fr/mesures/implantations.htm).

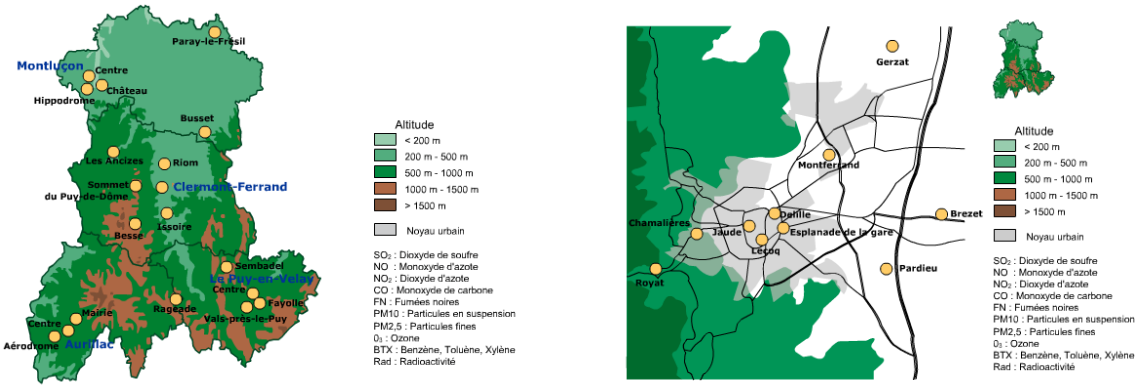

Figure 3.2. Location of Atmo-Auvergne measurement stations

3.2. Model geometry

3.2.1. WRF configuration

One of the main difficulties of the simulations using chemistry-transport models is to take into account the complexity of the air parcels dynamics in mountainous areas. A realistic description of the governing dynamical and thermo-dynamical condition is important for calculating gas and aerosol impacts on air quality. For this reason, we have used a (nested) modeling system that allows reproducing correctly this scale dynamics associated with the complex topography of the measurement site. To take into account the interactions between topography and the synoptic circulation, the mesoscale model WRF (WRF-ARW V3.2) is used in two-way nesting mode (Skamarock et al., 2008). To have a good resolution in meteorological forcing on the Auvergne region, it was decided to use a large computational domain. WRF operates on the 45 km, 9 and, respectively 3 km resolution domains having 100x100, 111x111, and respectively 100x100 grid points. WRF uses meteorological initial conditions and lateral boundary conditions every 6 h from the ECMWF (European Center for Medium range Weather Forecast) re-analyses data base. Data produced during pre-processing and modeling simulations of WRF are in the Lambert conformal projection. The time step of the output data has been set to 1 hour. In order to better reproduce the complex topography associated the PDD, the NASA Shuttle Radar Topographic Mission 90m Digital Elevation Data (~3s) were used (http://srtm.csi.cgiar.org/) which provides digital elevation data for over 80% of the globe. For our purpose were used the data for the marked area shown in the red rectangle in Figure 3.3.

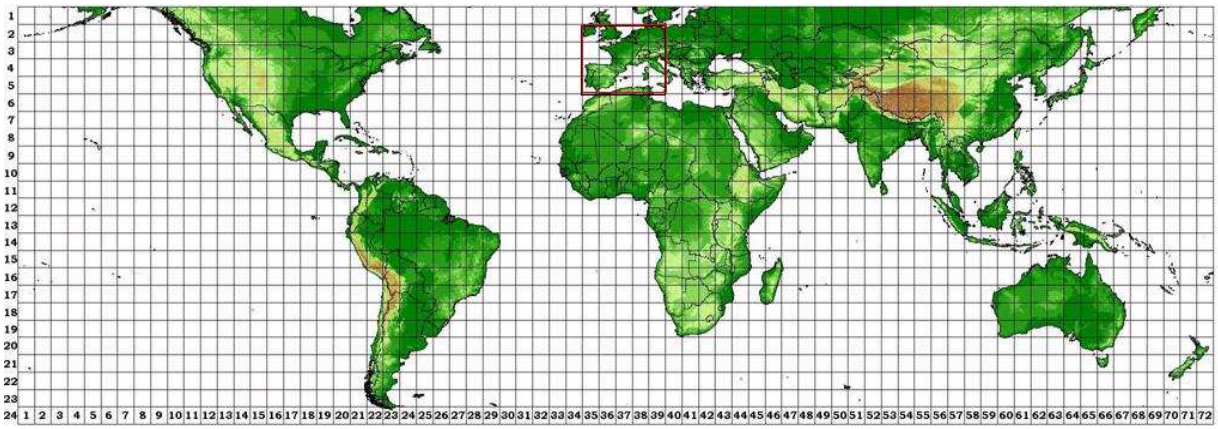

Figure 3.3. The domain at 90 m resolution – red rectangle (from http://srtm.csi.cgiar.org)

The default topography of 30s resolution has a range between 175.41 and 1561.46 m (1010.58 m at PDD site), while the 3s resolution has a range between 175.19 and 1564.45 m (1050.97 m at PDD site). Although we can see that the differences between modeled and real values of the PDD site are reduced using 3s resolution, the horizontal resolution of third domain is not sufficient to reproduce the altitude of PDD. The test made shown that using a grid which has 250 m horizontal resolution the model is able to reproduce accurately the PDD altitude.

3.2.2. CHIMERE configuration

Three domains (domains 1, 2, and 3 shown in Fig. 3.4) were employed for the CHIMERE calculations. Domains 1, 2, and 3 contain 98x74, 145x98, and 129x90 grid cells, with horizontal resolutions of 0.405, 0.081, and 0.027 degrees, respectively, and 8 verticals layer from the surface up to 500 hPa. The aerosol module takes into account primary particulate matter (anthropogenic primary species of elemental carbon, primary organic carbon, and other industrial dusts), nitrate, sulfate, ammonium, biogenic secondary organic aerosol (SOA), anthropogenic SOA and water, and uses 24 bins from 1 nm to 64 μm in order to take in account the particles lied in the nucleation mode. The parameterization of Vehkamaki et al. (2002) for sulfuric acid nucleation is used. The model was run over the period with full restart (i.e. the concentration fields are saved every 24h of integration and for the following run these concentrations are used as restart conditions), with a first spin-up run of 5 days in order to initialize the model from initial climatological values.

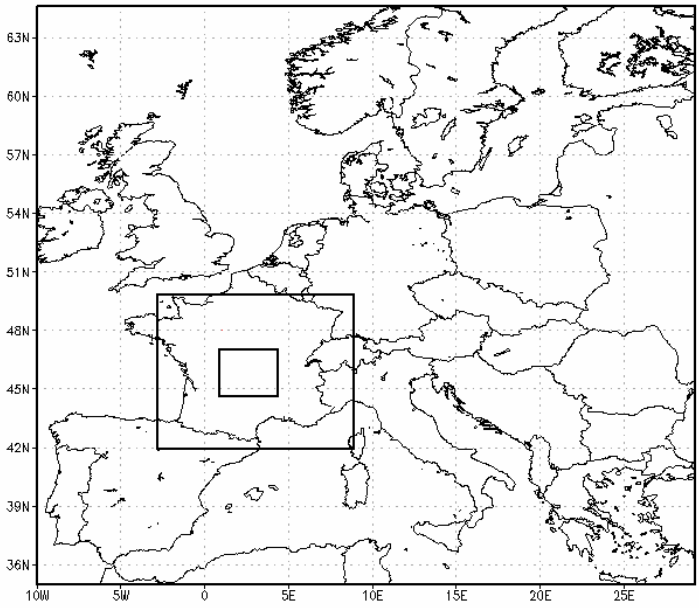

Figure 3.4. The CHIMERE domains employed in the calculations

3.3. Simulation of the meteorological parameters

The WRF simulations were made using two different topographical data sets: the default topography at 30" resolution (WRF-30") and the SRTM topography at 3" resolution (WRF-3").
The temperature and the relative humidity are evaluated for two stations at different altitudes. Because the observations for wind data are mostly missing, the wind speed and wind direction will not be evaluated. The evaluation of the modeled meteorological data sets is made using calculated statistics: hourly BIAS error, hourly root mean square error (RMSE) and the correlation coefficient (R).

$$BIAS = \frac{1}{N}\sum_{i=1}^{N} F_i - O_i$$

$$RMSE = \sqrt{\frac{\sum_{i=1}^{N}(F_i - O_i)^2}{N}}$$

where F_i represents the forecasted values, O_i represents the observed values, and N represents the total number of observations.

Figure 3.5 compares the diurnal variation of the WRF-30" and WRF-3" results averaged for the period from 24 February – 8 March 2009 against observations made at PDD summit. Each box ranges from the lower to the upper quartiles with a central bar at the median value, while the whiskers extend to the 25th and 75th percentiles. The vertical bars indicate the maximum and minimum, the horizontal line represents the median, therefore, measurements above and below the median can easily be discerned.

The hourly median for temperature shows that the temperature is generally well reproduced by both model configurations. However, diurnal variations are more pronounced in the model compared to measurements and during daytime, temperatures are overestimated by the model, up to 2.80 ^{o}C for WRF-30" and up to 2.45 ^{o}C WRF-3", with maxima observed around noon time (Fig. 3.5a). The underestimation for the first hours of the forecast can be associated with the spin-up of the WRF model. Even though the diurnal variation of the median temperature is more pronounced in the model compared to measurements, the variability of the diurnal variation of the temperature is very similar in both simulations to the measurements.

The relative humidity is underestimated by the model, within a range of (-28.9;-3.3%) for WRF-30" and (-27.7;-1.9%) for WRF-3" (Fig.3.5b) and the hourly median shows that the model is not reproducing well the observed mean diurnal variation of relative humidity observed at PDD summit. While the model is predicting a minimum in the RH during the morning hours, measurements are showing a median RH constantly close to 95 % RH. Again, the modeled variability in the diurnal cycle is closer to the variability in the measurements. Here, the bias between model and measurement is likely partly due to measurement artifacts. Indeed RH sensors do not react immediately to a decrease in RH after they have reached saturation (100%). Usually it takes a couple of hours after the actual RH is lower than 100% before the sensor indicate a RH decrease. It is also not excluded that the model does not simulate the presence of clouds properly when there are some. The combination of both measurement and model bias would explain that RH is not simulated as well as temperature at the Puy de Dome station.

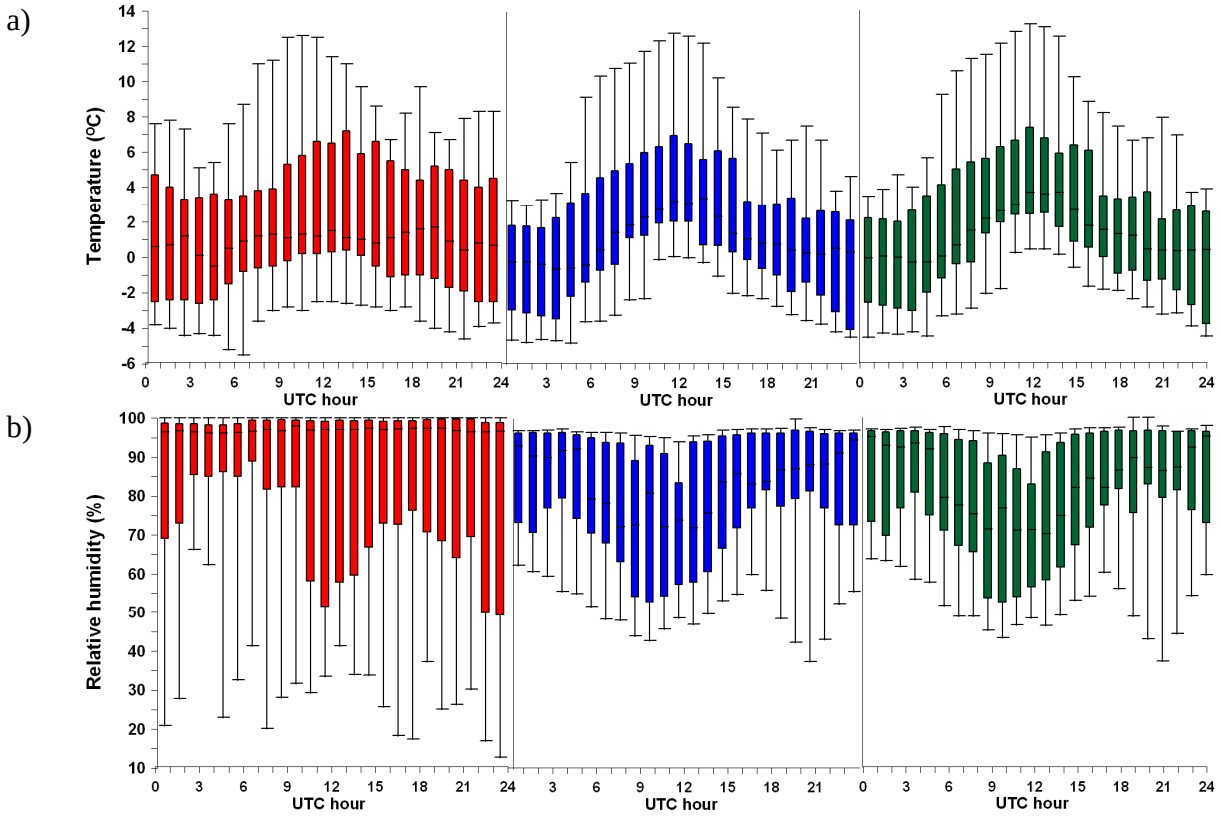

Figure 3.5. Hourly boxplot for temperature (a) and relative humidity (b) for the observation (red line) together with calculated values by WRF-30" (blue line) and WRF-3" (green line) at PDD station. The line in the middle of the box is the median, while the boxes represent the upper and lower quartile and the "whiskers" represent the 25th and 75th percentile for 24 February – 8 March 2009 period.

Table 3.2 shows that for the entire period the values of BIAS and RMSE for the temperature and relative humidity of WRF-3" match better the observation than WRF-30", and have similar R values.

Table 3.2. Statistics for meteorological parameters for 24 February – 8 March 2009 period at PDD station

	BIAS*		RMSE**		R	
Parameter/model	WRF-30"	WRF-3"	WRF-30"	WRF-3"	WRF-30"	WRF-3"
Temperature (^{o}C)	-0.13	0.12	1.52	1.41	0.83	0.86
RH (%)	-12.38	-10.96	12.5	11.12	0.47	0.46

Figure 3.6 compares the average diurnal variation of the WRF-30" and WRF-3" results against the observations made at Cezeaux (45° 45' 33" N, 3° 6' 46" E), a boundary layer station situated at 410 m altitude.

The hourly median for temperature shows that the mean diurnal temperature evolution is generally well reproduced by both model configurations. However, while during daytime the differences between model and observation are not important, during night time the temperatures are underestimated by the model, up to -3.06 ^{o}C for WRF-30" and up to -2.60 ^{o}C WRF-3" (Fig. 3.6a).

Contrarily to PDD station, the mean diurnal relative humidity modeled for the BL station is in generally overestimated within a range of (-5.17; 19.01%) for WRF-30" and (-4.09;19.22%) for WRF-3" (Fig.3.6b). The hourly median variation shows that the relative humidity is generally well reproduced by both model configurations.

Table 3.3 confirms that, as in the case of PDD summit, for the entire period the values of BIAS and RMSE for the temperature and relative humidity of WRF-3" match better the observation than WRF-30", and have similar R values, Table 3.3.

Table 3.3. Statistics for meteorological parameters for 24 February – 8 March 2009 period for BL station

	BIAS*		RMSE**		R	
Parameter/model	WRF-30"	WRF-3"	WRF-30"	WRF-3"	WRF-30"	WRF-3"
Temperature (^{o}C)	-0.69	-1.02	1.65	1.58	0.87	0.87
RH (%)	7.09	6.41	10.87	10.49	0.64	0.66

Because we found that using WRF-3" the meteorological parameters are better predicted in the following only this configuration it will be used.

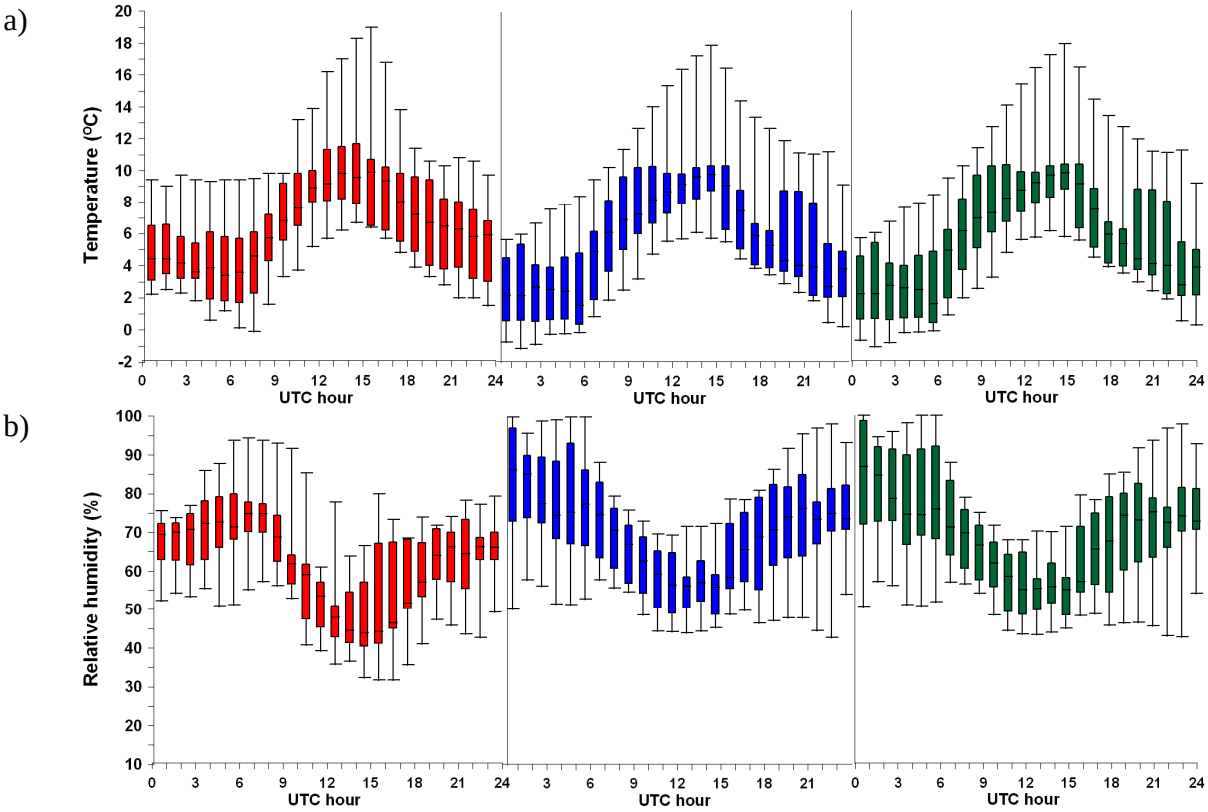

Figure 3.6. Hourly boxplot for temperature (a) and relative humidity (b) for the observation (red line) together with calculated values by WRF-30" (blue line) and WRF-3" (green line) for BL station. The line in the middle of the box is the median, while the boxes represent the upper and lower quartile and the "whiskers" represent the 25th and 75th percentile for 24 February – 8 March 2009 period.

3.4. Simulation of the gaz and particulate mass concentrations in the boundary layer station

The capacity of the model to simulate the pollutants concentration for BL stations is evaluated using statistical parameters such as mean error (BIAS), root mean square error (RMSE) and normalized mean bias (NMB), as described previously.

The error analysis applied to the ATMO-Auvergne network sites clearly showed that the model has difficulties in reproducing the BL stations concentrations in the urban environment (Table 3.4). However, as can be observed in the Table 3.3, that the values of BIAS, RMSE and NMB

are reduced for all parameters when the MACC emissions database is used in comparison with EMEP emissions database.

Table 3.4. Statistics for ATMO Auvergne stations for 24 February – 8 March 2009 period

Parameter/Emissions database	*BIAS (ppbv)		**RMSE (ppbv)		***NMB(%)	
	EMEP	MACC	EMEP	MACC	EMEP	MACC
NO	-10.82	-8.17	15.40	14.78	-98.33	-91.58
NO_2	-15.02	-11.03	16.47	13.10	-88.30	-64.88
O_3	17.24	14.49	17.86	15.83	65.67	55.19
SO_2	-0.46	0.15	0.76	0.86	-59.25	17.72
PM2.5	-11.17	-10.02	11.67	10.87	-58.59	-52.40
PM10	-13.31	-11.81	14.47	13.26	-58.98	-51.27

*** $NMB = 100 * \left(\sum_{i=1}^{N} F_i - O_i \right) / \sum_{i=1}^{N} O_i$

The NO concentration is underestimated within a factor of 60.08 when EMEP emissions are used and it is significantly reduced to a factor of 11.87 for MACC emissions. The NO_2 concentration is underestimated within a factor of 8.55 for EMEP emissions, and 2.84 for MACC emissions. The O_3 is overestimated by a factor of 1.65 for the EMEP emissions and respectively 1.55 for MACC emissions. For SO_2, the use of the EMEP database gives us an underestimation within a factor of 2.45, while the MACC emissions database overestimates the observation by a factor of 1.17. Both PM2.5 and PM10 simulations are underestimated compared to the observations, by a factor of 2.45, respectively 2.43 when EMEP emissions are used, and by a factor of 2.10, respectively 2.05 when MACC emissions are used.

These values indicate that the use of the MACC emissions data base increases the agreement between model and measurements for all gaseous species and also for particle mass, compared to the use of the EMEP emissions data base.

In order to better identify when and why there are some discrepancies between simulations and measurements, we use medians and quartiles to graphically summarize the studied parameters during their mean diurnal evolution (i.e. averaged over the whole measurement period of 14 days). Figure 3.7 compares the average diurnal trend of the CHIMERE results based on the EMEP and MACC emissions against observations.

The hourly median concentration for O_3 shows that the model overpredicts the measured ozone concentrations with both emission databases. However, while the diurnal variation of ozone is

not captured at all by the model when using the EMEP emission inventory, the model predicts correctly a mid-day maximum and early morning and early evening minima when using the MACC inventory. The overprediction of O_3 by the model is highest during nighttime for both emission databases. Ozone concentrations are closely linked to the NO_x cycle and it can be overestimated due to insufficient depletion due to lack of NO and NO_2 emission (see Fig 3.7 b,c).

The NO median diurnal variation shows that for both emission databases the model fails to simulate the strong morning peak, even though a larger variability of NO concentrations in the morning is predicted when using the MACC emission inventory. The higher resolution of the MACC data base seems to increase the accuracy of local emissions, which is important for such a short life time species. Morning and evening peaks are typically linked to traffic-related sources, hence, the model underpredictions are likely caused by too weak emissions due to traffic, but also a too strong boundary layer mixing might contribute. The model does not capture the observed morning and evening peaks of NO_2, using the EMEP data base. It does predict them at the right moments of the day using the MACC data base, although they are still underpredicted by a factor of 3.71 compared with the observation. This can express the direct impact on the overestimation of ozone for the same time period.

The diurnal variation of the SO_2 median concentration is well simulated by CHIMERE when using the MACC emissions database, with slight increases around 9 am and 6 pm. However, SO_2 concentrations are underestimated all through the day when using the EMEP emissions by a factor of 2.19. Again, some sources of pollutants linked to urban traffic seem to be missing in the EMEP inventory.

As for most primarily emitted gases, aerosol particles are underestimated by the model compared to measurements. The modeled median diurnal variations of PM2.5 and PM10 concentrations show an improvement when MACC emissions are used, as they show the two morning and evening peaks linked to the traffic. However, for both inventories, day and nighttime concentrations are significantly underpredicted, and secondary sources are likely missing in the model. This aspect will be further studied by investigating which chemical species are underestimated in particular in the aerosol phase (see section 3.5.2).

From this analysis, we can conclude that the model is not able to capture the intensity of urban variability from human activity. However, using the MACC emissions data base, we can see a

significant improvement in comparison with EMEP emissions database for boundary layer concentration in urban and suburban environments.

a)

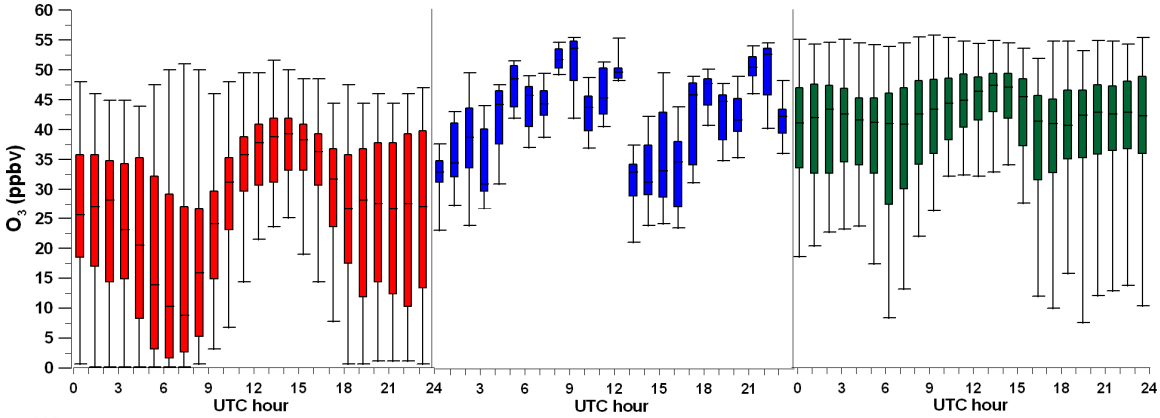

b)

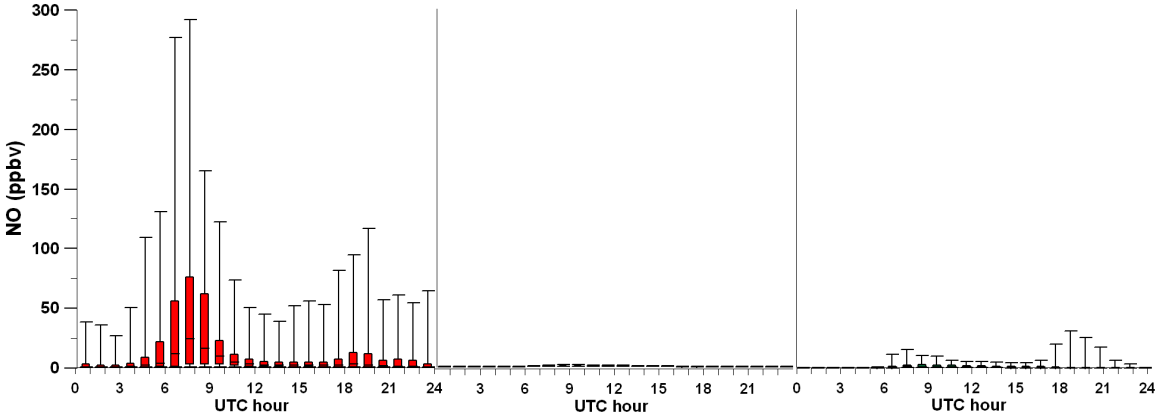

c)

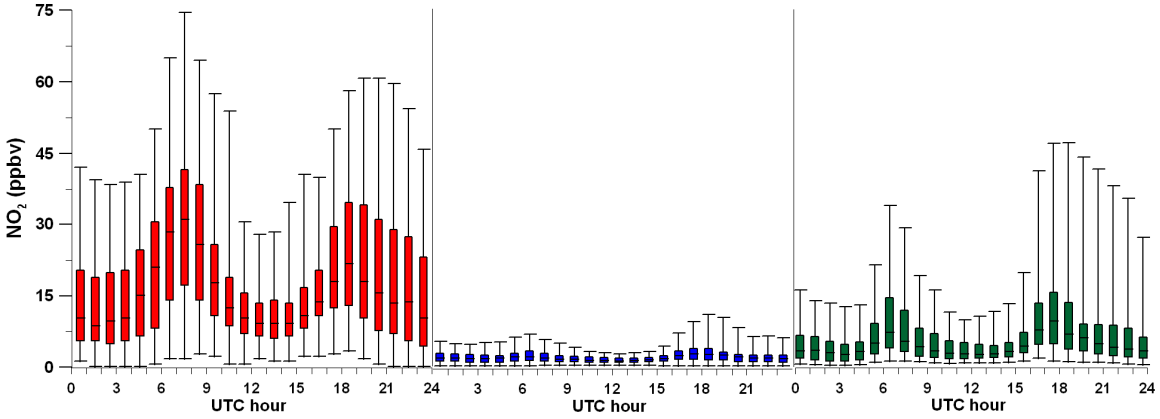

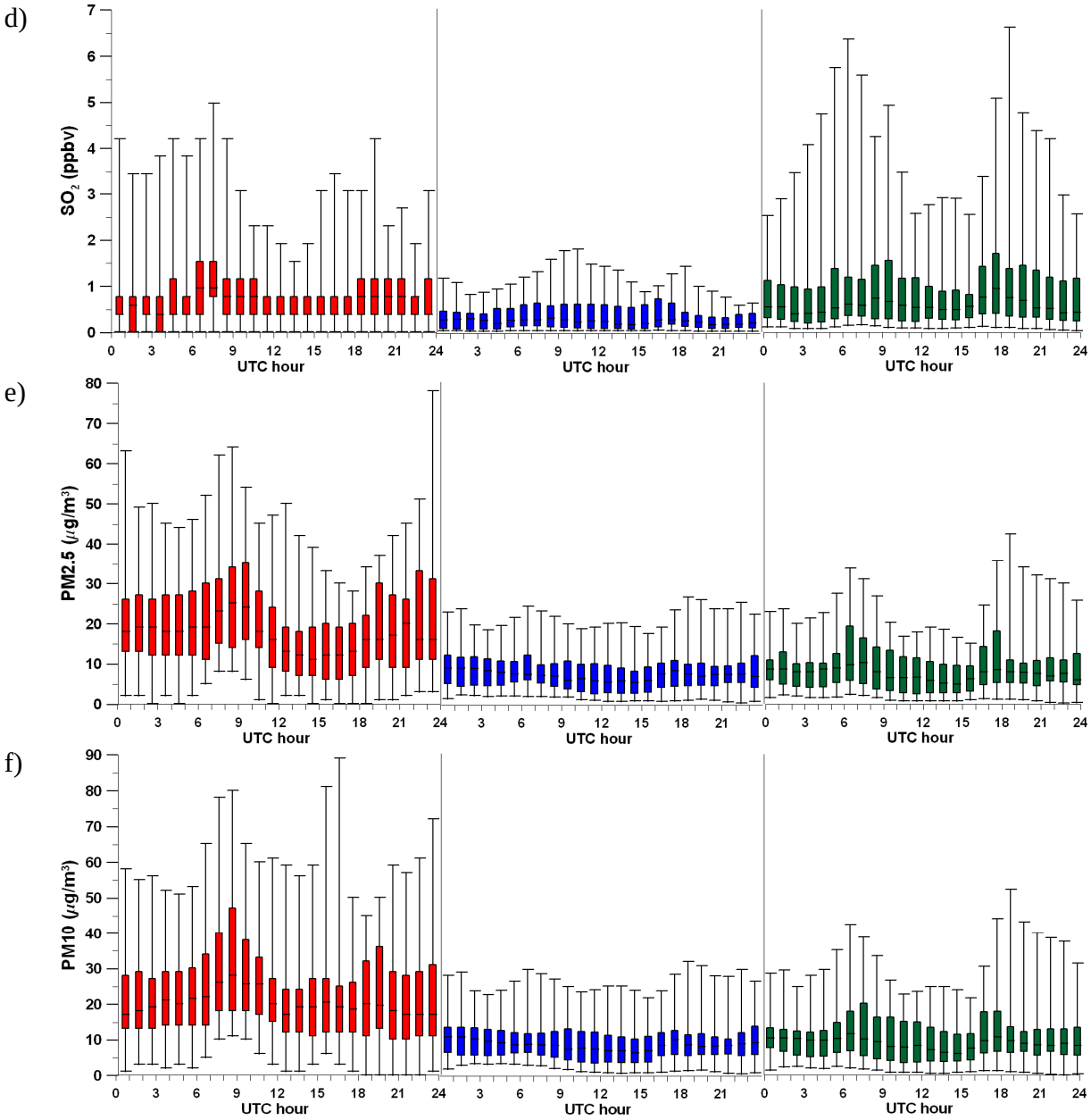

Figure 3.7. Hourly boxplot for O_3 (a), NO (b), NO_2 (c), SO_2 (d), PM2.5 (e), and PM10 (f) for urban stations of the ATMO-Auvergne network for the observation (red line) together with calculated values by CHIMERE-EMEP (blue line) and CHIMERE-MACC (green line). The line in the middle of the box is the median, while the boxes represent the upper and lower quartile and the "whiskers" represent the 25th and 75th percentile for 24 February – 8 March 2009 period.

3.5. Simulation of the gas and particulate mass concentrations at the high altitude station

We are now going to compare modeled and measurement pollutant concentrations at the altitude site of the Puy de Dome, where long range transport is taking a larger part in the atmospheric burden. The same error analysis as for the BL stations is applied. The ME, RMSE and NMB for PDD site using two different emissions database are presented in Table 3.5 and Table 3.6.

3.5.1. Gas phase components

As can be seen in Table 3.5 the values of BIAS, RMSE and NMB for the period 24 February – 8 March 2009 do not significantly differ from one emission database to the other as opposed to previously observed for the surface stations in the boundary layer.

Table 3.5. Statistics for PDD site for 24 February – 8 March 2009 period

Parameter/Emissions	*BIAS (ppbv)		**RMSE (ppbv)		***NMB(%)	
database	EMEP	MACC	EMEP	MACC	EMEP	MACC
NO	-0.07	-0.08	0.09	0.11	-48.31	-54.78
NO_2	-0.08	-0.10	0.44	0.70	-7.83	-8.84
O_3	4.18	4.55	5.81	6.12	9.43	10.26
SO_2	-0.05	-0.15	0.19	0.20	-18.21	-61.39
CO	-9.95	-13.00	18.75	23.43	-6.68	-8.74

As shown by Fig. 3.8, the model reproduces the surface ozone time variation at PDD with a very slight overestimation. The overestimation factors are close for both emissions inventories databases, i.e. 1.09 for EMEP and 1.10 for MACC.

The evolution of the NO_2, and NO on PDD summit is also generally well captured; the model underestimates the NO by a factor of 1.93 for EMEP, respectively 2.21 for MACC, and the NO_2 by a factor of 1.08 for EMEP, and 1.09 for MACC.

The concentrations of CO tend to be overestimated by the model (by a factor of 1.07 for EMEP and 1.09 for MACC), which could reflect a problem with the current source inventories due to

overestimation of local anthropogenic sources and biomass burning emissions as well as an underestimation of OH (Bey et al., 2001). This comparative analysis between simulations and observed data shows that the model could reproduce the mean diurnal cycle of most considered species.

Contrarily to other gaseous species, the SO_2 concentrations measured at the PDD are underestimated within a factor of 1.22 by the model when the EMEP emission inventories are used and by a factor of 2.58 when the MACC inventory is used. This is surprising since SO_2 concentrations were not as underestimated by the model when using the MACC inventory as when using the EMEP inventory for the BL sites.

a)

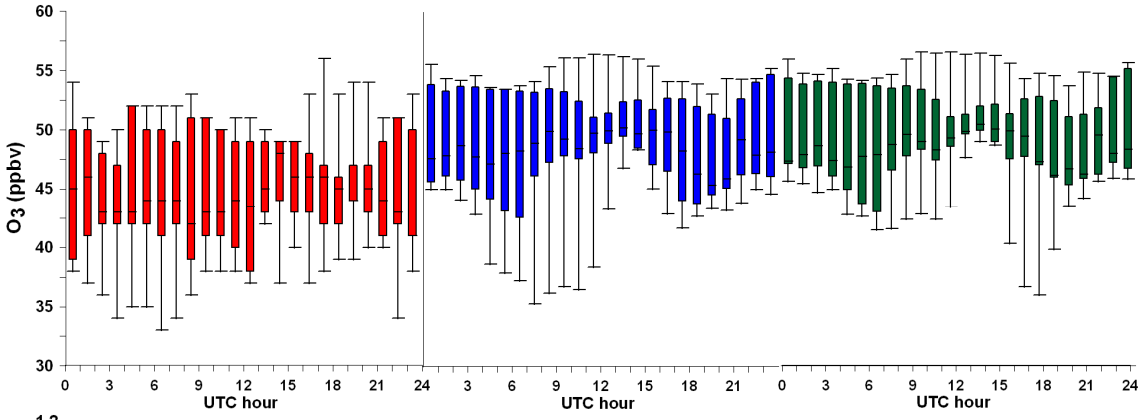

b)

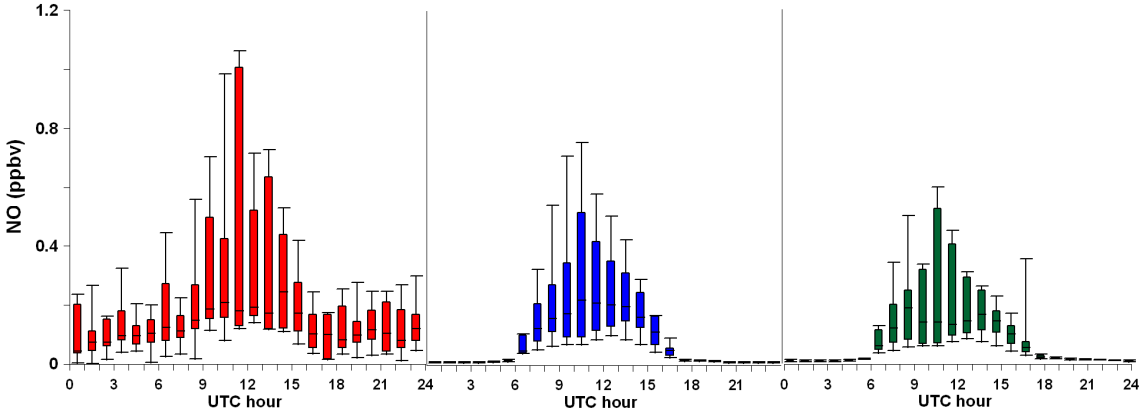

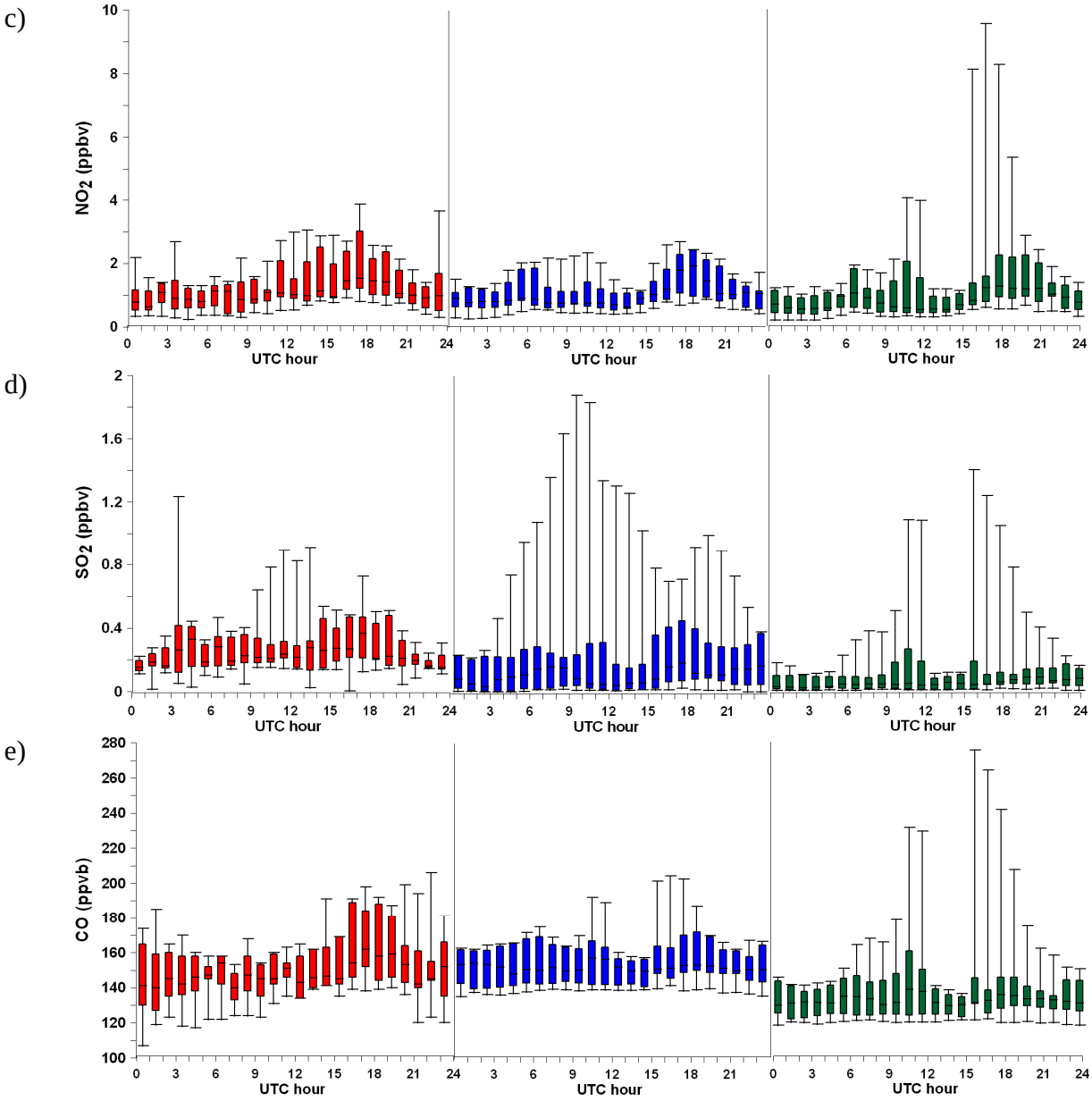

Figure 3.8. Hourly boxplot for O_3 (a), NO (b), NO_2 (c), SO_2 (d), and CO (e) for PDD site for the observation (red line) together with calculated values by CHIMERE-EMEP (blue line) and CHIMERE-MACC (green line). The line in the middle of the box is the median, while the boxes represent the upper and lower quartile and the "whiskers" represent the 25th and 75th percentile for 24 February – 8 March 2009 period.

Overall the model is more successful in reproducing the background concentrations observed at the elevated site (Puy de Dome) than in reproducing the concentrations observed in the urban area of Clermont-Ferrand where they are more influenced by local sources. Differences in simulations when different emission data bases are used are not significant when simulating high

altitude concentrations. Diurnal variations of gaseous pollutant are well captured, indicating that vertical transport is relatively well simulated. For example, maxima concentrations of NO are observed and modeled at mid-day at the PDD, while they are modeled and measured with morning and evening peaks in the BL. This is clearly the effect of the increase of the BLH that reaches the PDD level during mid-day, bring BL pollutant up to the summit.

The differences between observed and modeled concentration of pollutants for the BL stations and the PDD station can be due to the weather conditions during the analyzed period.

For the BL station, during daytime the modeled wind speed median is overestimated due to convection, while during nighttime the median wind speed is underestimated (see Fig. 3.9a). Due to its location, in the urban area of Clermont-Ferrand, stagnant weather conditions are observed, causing high pollutants concentrations during winter time. These stagnant conditions are characterized by low wind speeds (see Fig. 3.9a).

For the PDD station, the wind is speed is in generally underestimated (see Fig. 3.9b), this underestimation is more accentuated during nighttime up to 7.95 m/s. The reduced vertical mixing in combination with stronger horizontal winds during analyzed period means that the particles can be transported in the boundary layer over longer distances.

Topographical configuration significantly affects air flow in the lower atmosphere and remarkably influences alterations in its direction and speed. On the basis of the topographic data and wind direction and speed in the region, we can conclude that the urban area is not ventilated during the analyzed period leading to the increase of pollutants (see Fig. 3.2 and 3.10a).

Winds at the PDD summit have a strong westerly component (modeled and observed), so it is rare that anthropogenic pollution from either town reaches the station (see Fig. 3.10b).

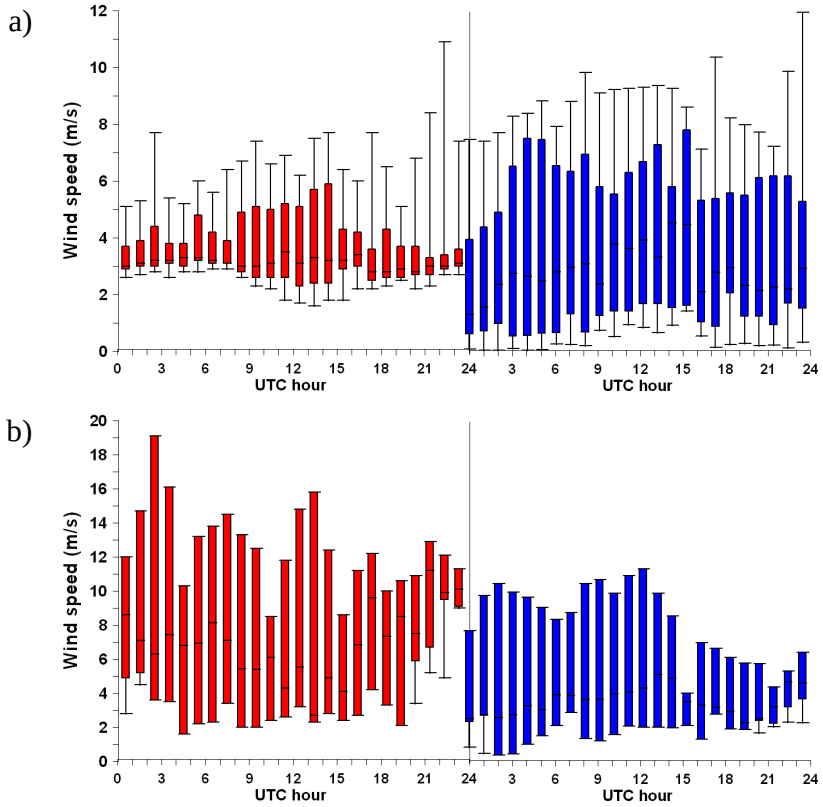

Figure 3.9. Hourly boxplot for wind speed at the BL station (a) and PDD (b) for the observation (red line) together with calculated values by WRF (blue line). The line in the middle of the box is the median, while the boxes represent the upper and lower quartile and the "whiskers" represent the 25th and 75th percentile for 24 February – 8 March 2009 period.

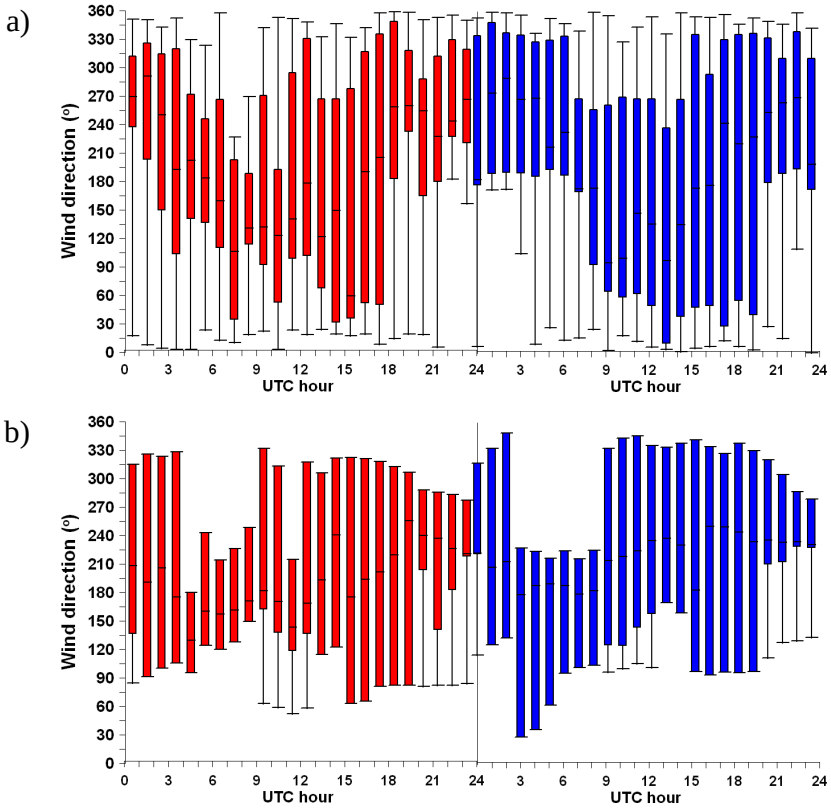

Figure 3.10. Hourly boxplot for wind direction at the BL station (a) and PDD (b) for the observation (red line) together with calculated values by WRF (blue line). The line in the middle of the box is the median, while the boxes represent the upper and lower quartile and the "whiskers" represent the 25th and 75th percentile for 24 February – 8 March 2009 period.

The temporal variations that are linked with the wind direction and speed are in general well reproduced. In the BL, a stagnant wind condition results in high concentration of pollutants. The differences between models and measurements represent in the same time the uncertainty on the stable boundary layer estimation, the uncertainty on the emissions inventories knowledge, the uncertainty of the morning wind field and the subsequent advection and the spatial heterogeneity of these sources. In addition to uncertainties in predicted meteorology (low simulated wind speeds in the BL), another factor which can contribute to the overpredictions for all gaseous compound can be the horizontal resolution of the domain. A 3 km horizontal grid resolution seems to be too coarse to resolve the local emission strengths and distributions needed to reproduce point-wise observations (Zhang et al., 2006).

3.5.2. Aerosol phase chemical species

Contrarily to the gas phase concentrations for which the emission data base had little impacts on the accuracy of the simulation for the PDD, the statistical error analysis shown in Table 3.6 indicates a significantly improvement of the forecast for NO_3 and NH_4 when the MACC emissions database is used.

Table 3.6. Statistics for aerosol chemical composition at PDD site for 24 February – 8 March 2009 period

Parameter/Emissions database	*BIAS (μg/cm^3)		**RMSE (μg/cm^3)		***NMB(%)	
	EMEP	MACC	EMEP	MACC	EMEP	MACC
SO_4	-0.10	-0.60	0.65	0.72	-8.18	-48.78
NO_3	2.85	2.24	2.85	2.24	263.88	207.31
NH_4	0.34	-0.01	0.65	0.58	27.76	-0.94
OC	-1.16	-1.18	1.28	1.29	-68.20	-69.04

Sulfate aerosols are produced by chemical reactions in the atmosphere from gaseous precursors (with the exception of sea salt sulfate and gypsum dust particles). The key controlling variables for the production of sulfate aerosol from its precursors are:

1. the source strength of the precursor substances,
2. the fraction of the precursors removed before conversion to sulfate,
3. the chemical transformation rates along with the gas-phase and aqueous chemical pathways for sulfate formation from SO_2.

The atmospheric burden of the sulfate aerosol is then regulated by the interplay of production, transport and deposition (wet and dry) (IPCC, 2007).

In general, the model underestimates the SO_4 (Fig. 3.11a), although a good agreement between simulations and measurements is reached. In case of EMEP emissions, SO_4 concentrations are underestimated by the model within a factor of 1.08 of observation, while MACC emissions lead to a factor of 1.95 within the observations. This result can be directly due to the SO_2 concentrations, which are also overestimated when using MACC compared to EMEP. SO_2 has a lifetime in the atmosphere of about a day, before being deposited to the surface or oxidized to sulfate (SO_4) aerosol. In the gas phase, SO_2 oxidation occurs by reaction with hydroxyl radicals (OH), to form sulfuric acid (H_2SO_4). Sulfuric acid is hygroscopic, and rapidly condenses, either forming new aerosols, or adding to existing ones. Sulfur dioxide gas also partitions into the aqueous phase (in cloud droplets or pre-existing aerosols), where it reacts with dissolved

hydrogen peroxide (H_2O_2) or ozone (O_3) to form SO_4. The analysis of the diurnal variation of measured and modeled concentrations shows that the underestimation of SO_4 concentrations when using the MACC emission data base is mainly due to the prediction of a lower mid-day peak compared to measurements. The cause of this underestimation could be that (1) BL SO_4 is too low (which is likely since BL SO_2 is underestimated), (2) that vertical transport of BL SO_4 is too weak or (3) photochemistry of the PDD SO_2 is too weak. Because the model underestimation is lower for SO_4 compared to SO_2, a too weak photochemistry of SO_2 at the PDD level is not explaining the underestimation of SO_4.

The inorganic aerosol system has three states, listed in order of increasing NH_4 concentration: (1) acidic, where there is insufficient NH_4 to neutralize the SO_4, (2) NH_4 limited, where all of SO_4 is neutralized, but the formation of NH_4NO_3 is limited by scarce NH_4, and (3) NO_3 limited, where NH_4 is present in excess such that the formation of NH_4NO_3 is limited by scarce HNO_3. Reductions in NO_3 and SO_4 will cause the system to become more NO_3 limited, decreasing the sensitivity of inorganic PM2.5 to NH_3. However, if the aerosol is initially acidic, then reductions in SO_4 can cause some NH_4 to become available for NH_4NO_3 formation, which could increase the sensitivity of PM2.5 to NH_3 emissions (Pinder et al., 2006).

Graphical comparisons between the measured and predicted NH_4 and NO_3 hourly median concentrations are shown in Fig. 3.11b), c). As shown, the NH_4 and particularly NO_3 concentrations are both overestimated.

The model overestimates the NH_4 by a factor of 1.27 for EMEP, but adequately simulates it (overestimated by a factor of 1.01) for MACC emissions. The overestimation of NH_4 concentrations using the EMEP inventory could be linked to the limited and uncertain statistical information on emissions, such as activity levels in fertilizer application and animal population census (Battye et al., 2003). This can be explained by the fact that NH_4 aerosol is primarily a product of NH_3 reacting with acids formed in the atmosphere, such as H_2SO_4, HNO_3, and HCl and the formation of these acids depends on the availability of hydroxyl radical (OH) and O_3 in the atmosphere (Seinfeld, 1986). Higher relative humidity leads to increased concentrations of NH_4 associated with aerosols. Therefore, increased water vapor in the atmosphere near sources of NH_3, lead to higher concentrations of NH_4 (Andersen et al., 1999; Asman, 1994; Warneck, 1988; McMurry et al., 1983). Moreover, at high relative humidity (>62%) ammonium nitrate is less likely to dissociate into HNO_3 and NH_3 (Stelson and Seinfeld, 1982). Wind speed is a

significant parameter in the model. Low wind speeds often coincide with stable conditions and limited dispersion whereas lower concentrations are often characterized by higher wind speeds and increased mixing throughout the boundary layer (Arya, 1999).

The most substantial bias found in our simulations is an overestimation of nitrate aerosol component. The NO_3 concentrations are overestimated within a factor of 3.63 for EMEP, respectively 3.07 for MACC. Winter nitrate concentrations are higher because sulfate levels are lower, temperatures are lower and more ammonia is available (EPA, 1996, 1998; Blanchard and Hidy, 2003). Higher NH_3 and lower SO_2 emissions allow complete neutralization of H_2SO_4, formation of aerosol nitrate depends upon the availability of nitric acid (HNO_3-limitation) and nitrate concentrations are higher than sulfate. These interactions are dynamic and changes of H_2SO_4 due to changes of SO_2 emissions can leave more or less NH_3 to react with HNO_3 and lead to changes in nitrate concentration. The overestimation of the nitrate concentrations (Fig. 3.11b), could be explained by: the model underestimates sulfate and more ammonia is available to form nitrate aerosols, which leads to an overestimation; because NH_3 concentrations are overestimated themselves, even more NH_3 is available to neutralize NO_3 and even more ammonium-nitrate is formed. Other models experience similar problems in simulating aerosol nitrate, for example the Comprehensive Air quality Model with extensions (CAMx)/particulate matter CAMx (PMCAMx) (Aksoyoglu et al., 2011; Andreani et al., 2007) or WRF/Chem (Li et al., 2010). For most measurements methods, nitrate suffers from a strong volatilization artifact during sampling, which is difficult to quantify, which could explain model higher overestimations against measurements in the literature. In the present work however, the volatilization artifact usually encountered during filter sampling did not occur as the measurements are acquired using an on-line mass spectrometer.

Contrarily to most inorganic compounds, the organic carbon (OC) is in generally underestimated by the model (Fig. 3.11d). The OC is underestimated within a factor of 3.14 when EMEP emissions data base are used, and by a factor of 3.23 for MACC emissions. This could be due to errors in the OC emissions (particularly in biomass burning emissions), but also most probably caused by the lack of some secondary organic aerosols formation routes in the model (Heald et al., 2005).

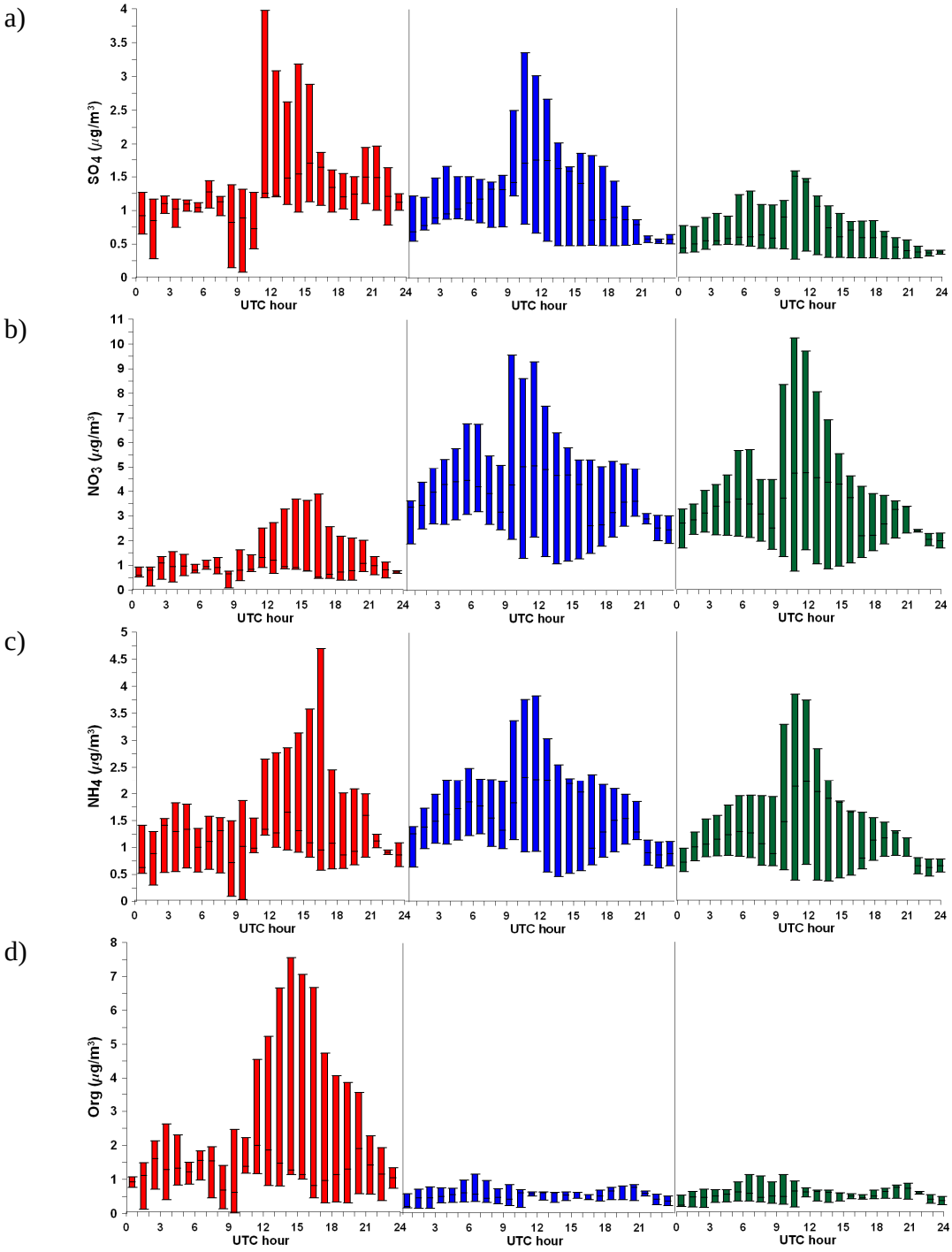

Figure 3.11. Hourly boxplot for SO_4 (a), NO_3 (b), NH_4 (c), and OC (d) for PDD site for the observation (red line) together with calculated values by CHIMERE-EMEP (blue line) and CHIMERE-MACC (green line). The line in the middle of the box is the median, while the boxes represent the upper and lower quartile and the "whiskers" represent the 25th and 75th percentile for 24 February – 8 March 2009 period.

3.6. Conclusion

We evaluated the behavior of the WRF meteorological model at two altitude stations using two different topographical input databases. Simulated diurnal temperature trends are very close to the observations. Temperature shows good agreement with measurements. However, the prediction of the diurnal trends for relative humidity in the model is not as good as temperature. Differences in modeled versus observed relative humidity may also lead to differences in certain aerosol microphysical processes (nucleation, equilibrium partition) and the amount of water associated with aerosols which may affect aerosol physical properties.

We also evaluated the impact of EMEP versus MACC emissions inventories on gas-phase and aerosol concentrations for the period February 24 – March 8, 2009. Generally, the statistical validation shows that the CHIMERE model is able to reproduce the gas-phase, and most aerosol particle concentrations (except organic carbon) at the PDD site. However for the BL stations, CHIMERE is not capable of capturing localized events during the day. The use of MACC emissions database, however, gives us an improvement in the simulation of gas-phase and aerosol composition.

A good prediction of the meteorological parameters and of the SO_2 concentration is necessary because these are the principal contributor factors to the new particle formation. An evaluation of the SO_2 concentrations with measurements shows that modeled SO_2 agreed reasonably with observations.

It was hypothesized that the initial step of new particle formation involved cluster formation by H_2SO_4 and water vapor and that H_2SO_4 is also responsible for the subsequent growth of the clusters. Therefore, the formation of new particles is affected by: the production of condensable vapor precursors, such as H_2SO_4, formed from oxidation of SO_2 (Kulmala et al, 1995); surface area of pre-existing particles; temperature, and relative humidity.

In the next chapter we will asses the model capacity to reproduce new particles formations events.

Chapter 4. Model capacity to reproduce new particle formation at high altitude

4.1. Introduction

The impact of the emissions databases was assessed in the previous chapter, where we saw that the atmospheric abundance of primary particles is essentially determined by the emission strength, while the abundance of nucleated particles responds in complex ways to variations in precursor gases and existing particle concentrations (Gaydos et al., 2005; Spracklen et al., 2006; Jung et al., 2006; Pierce and Adams, 2007; Wang and Penner, 2009) and other environmental factors that are still not completely understood (Lyubovtseva et al., 2005; Sogacheva et al., 2008).

The aim of this chapter is to evaluate the impact of the nucleation schemes and the role of the topography on the new particle formation at high altitudes.

The following section gives a description of these nucleation parameterizations.

4.2. Description of the parameterizations

In practice, the most common parameterization in the one from Kulmala et al. (1998) which involves the formation of nano-particles from a binary mixture of H_2SO_4 - H_2O (Kulmala et al., 1998). It is the default nucleation scheme used in CHIMERE. We decided to evaluate two other nucleation schemes. The first one is another nucleation scheme based on the H_2SO_4 - H_2O binary system (Vehkamaki et al., 2002). We decided to test the parameterization of Vehkamaki because Roth et al. (2003) showed that the use of different binary nucleation parameterizations in models

introduces significant uncertainties in the predicted number, production rates and number concentrations of PM2.5, particularly in the nuclei mode. The work of Vehkamaki et al. (2002) and Noppel et al. (2002) shows that the nucleation rates predicted from Kulmala scheme and Vehkamaki scheme differ, these differences can be attributed to the fact that the parameterization of Kulmala was based on the classical nucleation theory that contains mistakes in the kinetic treatment for hydrate formation and several approximations. The second nucleation scheme used in this study is a recent parameterization involving organics in the nucleation process (Metzger et al., 2010). All parameterizations are detailed below.

4.2.1. Kulmala's parameterization

The Kulmala nucleation scheme (Kulmala et al., 1998) is based on the binary nucleation rate, only dependant on thermodynamical equilibrium and no kinetical limitation. The parameterization depends on the mixture H_2SO_4 - H_2O, and it is highly dependent on the ambient temperature, relative humidity and gas concentration of sulfuric acid. The Kulmala parameterization can be applied for temperatures ranging between -40^o C and +25^o C and relative humidities between 10% and 100%, resulting in nucleation rates between 10^{-5} and 10^5 $cm^{-3}s^{-1}$.
The binary nucleation rate J is written

$$J = \exp(\chi) \tag{4.1}$$

with

$$\chi = 25.1289 N_{sulf} - 4890.8 N_{sulf} / T - 1743.3 / T - 2.2479 \delta N_{sulf} RH + 7643.4 X_{al} / T - 1.9712 X_{al} \delta / RH \tag{4.2}$$

and

$$N_{sulf} = \ln(N_{av} / N_{a,c}) \tag{4.3}$$

$$N_{a,c} = \exp(-14.5125 + 0.1335T - 10.5462 RH + 1985.4 RH / T) \tag{4.4}$$

$$Xal = 1.2233 - \frac{0.0154RA}{RA + RH} + 0.0102 \ln N_{av} - 0.04151 \ln N_{wv} + 0.0016T \quad (4.5)$$

$$\delta = 1 + \frac{T - 273.15}{273.15} \quad (4.6)$$

where:

$N_{a,c}$ - a critical concentration

X_{al} – H_2SO_4 mole fraction in the critical cluster

N_{av} and N_{wv} are sulfuric acid and water vapor concentrations (cm^{-3})

T – temperature in Kelvin

RA and RH – relative acidity and relative humidity divided by 100.

4.2.2. Vehkamaki's parameterization

The Vehkmaki parameterization is an extension of the parameterization of Kulmala. The Vehkamaki parameterization is valid for temperatures between -230.15^o K and 300.15^o K, relative humidities between 0.01% and 100%, and nucleation rates between 10^{-7} and 10^{10} $cm^{-3}s^{-1}$. The mole fraction of sulfuric acid in the critical cluster x* depends on temperature, relative humidity and gas phase concentration of sulfuric acid:

$$\begin{aligned} x^* = {} & 0.740997 - 0.00266379\,T \\ & - 0.00349998 \ln(N_a) + 0.0000504022\,T \ln(N_a) \\ & + 0.00201048 \ln\left(\frac{RH}{100}\right) - 0.000183289\,T \ln\left(\frac{RH}{100}\right) \\ & + 0.00157407 \left[\ln\left(\frac{RH}{100}\right)\right]^2 - 0.000179059\,T \left[\ln\left(\frac{RH}{100}\right)\right]^2 \\ & + 0.000184403 \left[\ln\left(\frac{RH}{100}\right)\right]^3 - 1.50345 \cdot 10^{-6}\,T \left[\ln\left(\frac{RH}{100}\right)\right]^3 \end{aligned} \quad (4.7)$$

The nucleation rate J is given by

$$J\left[1/\left(cm^3 s\right)\right] = \exp\{a(T,x^*) + b(T,x^*)\ln\left(\frac{RH}{100}\right)$$
$$+c(T,x^*)\left[\ln\left(\frac{RH}{100}\right)\right]^2 + d(T,x^*)\left[\ln\left(\frac{RH}{100}\right)\right]^3$$
$$+e(T,x^*)\ln(N_a) + f(T,x^*)\ln\left(\frac{RH}{100}\right)\ln(N_a)$$
$$+g(T,x^*)\left[\ln\left(\frac{RH}{100}\right)\right]^2 \ln(N_a) + h(T,x^*)\left[\ln(N_a)\right]^2$$
$$+i(T,x^*)\ln\left(\frac{RH}{100}\right)\left[\ln(N_a)\right]^2 + j(T,x^*)\left[\ln(N_a)\right]^3\} \quad (4.8)$$

where the coefficients a (T,x^*) … i (T,x^*) are given in Vehkamaki et al., 2002.

In the following we will do some comparisons between the Kulmala and the Vehkamaki parameterizations.

As can be seen in Fig. 4.1, varying the temperature and keeping the H_2SO_4 concentration constant we observe that for a temperature equal with 240 K both parameterizations give almost the same value for nucleation rate, J. The temperature increase leads to a divergent behaviors, the Kulmala parameterization gives higher nucleation rate within 4 orders of magnitude in comparison with the Vehkamaki parameterization. The nucleation rates for temperatures higher than 265 K are negligible.

However, increasing the H_2SO_4 concentration to 1e9 molecules/cm3 we noticed that the nucleation rate is still uncorrelated with the temperature increase, and the differences between the Kulmala and the Vehkamaki parameterization are reduced to 3 orders of magnitude for a temperature around 273.15 K.

The nucleation rates given by the Kulmala parameterization are considerably lower than the ones given by the Vehkamaki parameterization. Note also that the dependence on sulfuric acid concentrations (slopes of the curves differ between the models) as well as relative humidity (the Vehkamaki parameterization curves lie closer together than the parameterization curves) is different between the parameterization. Kulmala and Vehkamaki parameterizations show a strong T-dependence with a negative correlation between nucleation rate and T (i.e., nucleation rates decrease by 14-18 orders of magnitudes when T changes from 240 K to 300 K).

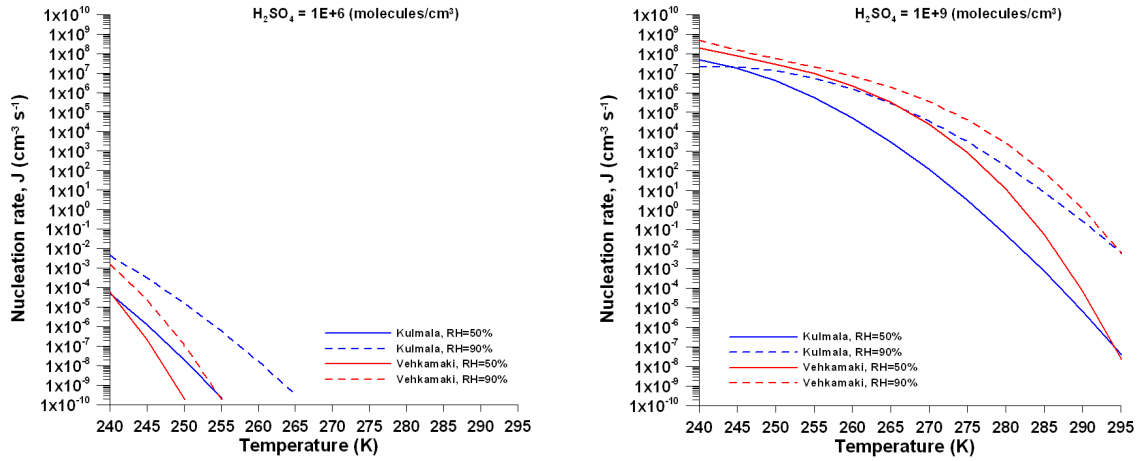

Figure 4.1. The nucleation rate as temperature function keeping constant the sulfuric acid concentration and varying the RH

The sulfuric acid dependence of the parameterizations agrees better in comparison with the previous test (the parameterization curves are almost the same) (see the Fig. 4.2) and the nucleation rate are correlated with the acid sulfuric concentration. Nucleation rates from the parameterization of Vehkamaki is one order of magnitude larger than the calculations of the Kulmala parameterization for H_2SO_4 concentrations ranging between 1e7 molecules/cm3 and 1e9 molecules/cm3 and 3 orders of magnitude lower for H_2SO_4 concentration at 1e6 molecules/cm3. Both parameterizations produce quite a similar relative humidity dependence. For a higher temperature we noticed that the nucleation rates are further from the values compared to the lower values.

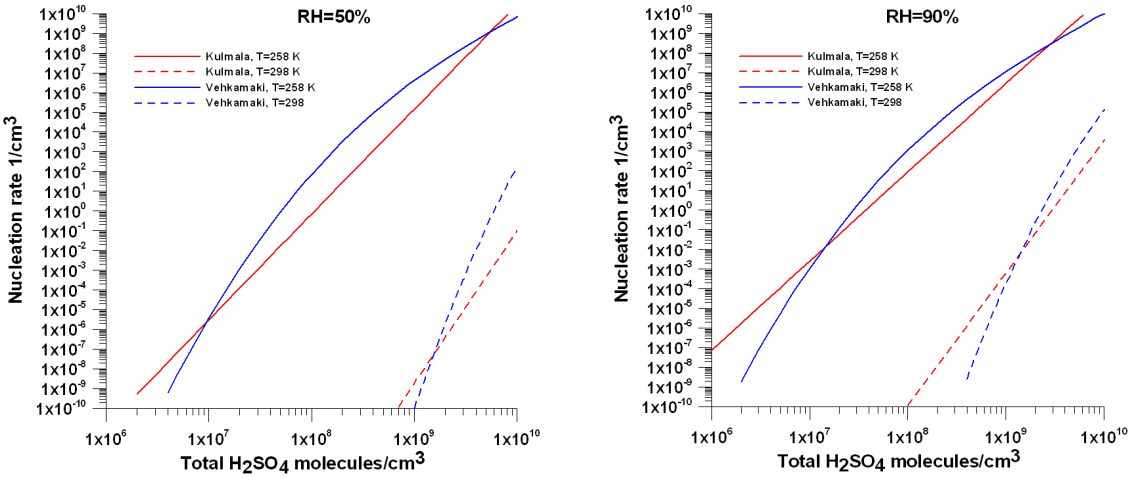

Figure 4.2. The nucleation rate as sulfuric acid concentration function keeping constant the RH and varying the temperature

As can be seen in Fig. 4.3, both parameterizations produce quite similar relative humidity dependence for relative humidities higher than 45 %. For temperatures higher the 298K, the nucleation rates for both schemes are negligible. At lower temperatures, the Vehkamaki parameterization results in 2–5 orders of magnitude too high nucleation rates compared with the Kulmala parameterization.

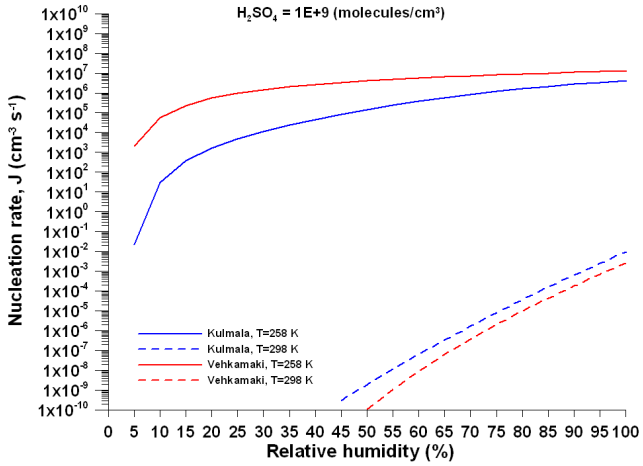

Figure 4.3. The nucleation rate as relative humidity function keeping constant the sulfuric acid concentration and varying RH

4.2.3. The organics parameterization

New particle formation can be modeled with the combined organic and sulfuric acid mechanism of Metzger et al., 2010. This nucleation mechanism is directly proportional to the sulfuric acid concentration and the concentration of low-volatility organic compounds. The parameterizations hence do not directly depend on relative humidity and temperature. The particle formation rate using this scheme can be described by

$$J_{nuc} = k[H_2SO_4][organic], \qquad (4.9)$$

In the present work, we have used k=5x10^{-13} cm^3 s^{-1}, accordingly to the work of Reddington et al., 2011. This value was also successfully used by Spracklen et al, 2010 in a previous comparison for observations at the Puy de Dome. The organics compounds used from the CHIMERE model for this parameterization are organics classified in three different volatility

groups: the group of anthropogenic species of moderate saturation vapor pressure, the group of anthropogenic species of low saturation vapor pressure and the group of biogenic species of moderate saturation vapor pressure.

4.3. The impact of the nucleation scheme on the modeling results of CHIMERE

For the intensive campaign at PDD during February 24 – March 8, 2009 period we calculated the total aerosol number concentration. We noticed that large discrepancies between observations and the WRF-CHIMERE model results when the Kulmala nucleation scheme was applied (see Fig. 4.4). The Kulmala scheme overestimates the observational findings significantly, most of the time about two orders of magnitude. In order to investigate the impact of the nucleation scheme for the model we replaced the Kulmala scheme by the parameterization of Vehkamaki. As can be seen in Fig. 4.4 the overestimation of total particle number concentration is generally reduced in the case of the Vehkamaki scheme, although it particle number concentrations are still highly overestimated.

We investigated the reason for the overestimation of the aerosol number concentration by observing at which size this overestimation occurs. Figure 4.5 presents the results of the comparison obtained for aerosol number size distribution for March 6th, 2009 during the period 06-09 UTC, when nucleation usually occurs at the site (Venzac et al. 2008). While the Vehkamaki scheme reproduces quite well the observations, our test simulation shows that the Kulmala scheme produces unrealistically high particles concentrations in the nucleation mode. Although the results show high temporal variability with occasionally high number concentrations, the Vehkamaki nucleation scheme gives more realistic values in comparison with the observations.

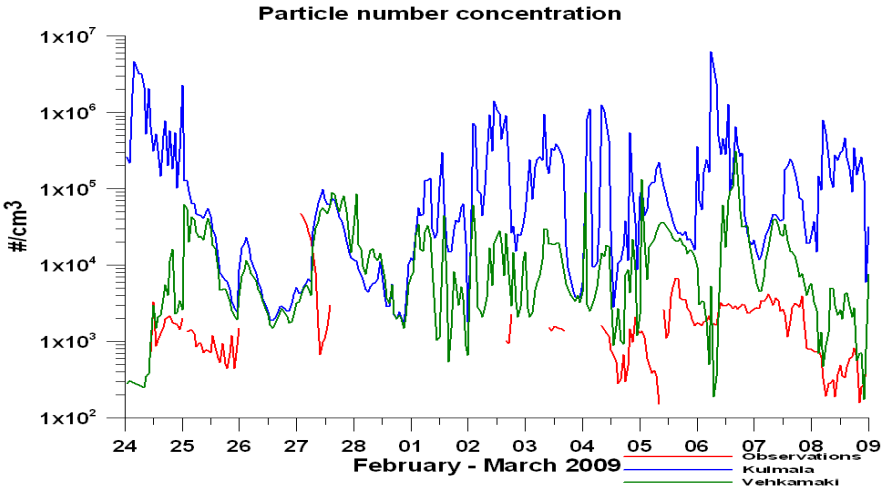

Figure 4.4. Total particle number concentration observed and modeled during the intensive campaign from 24 February to 8 March 2009

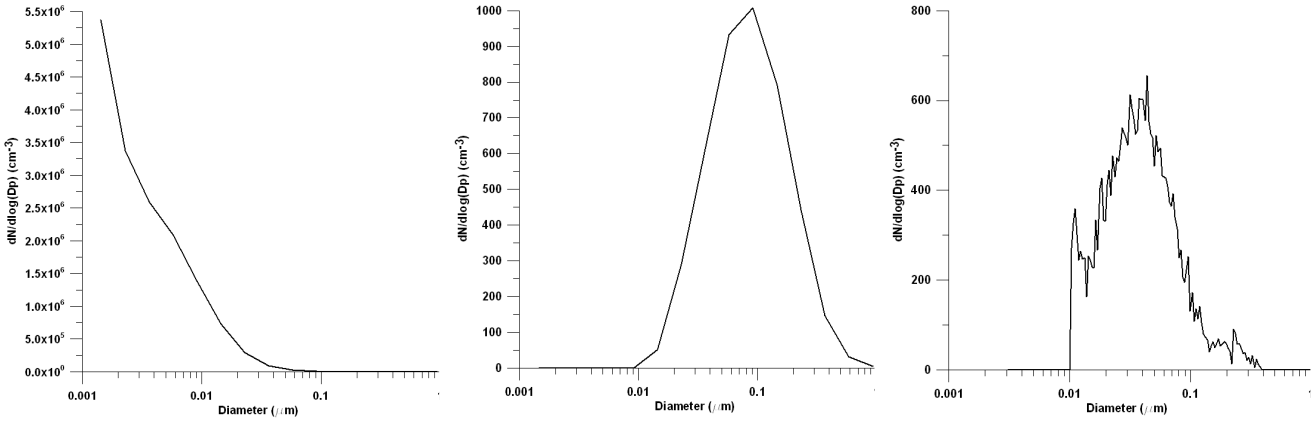

Figure 4.5. Number size distribution average 06-09 UTC at 6th March 2009 for: Kulmala scheme (left panel); Vehkamaki scheme (middle panel); and Observations (right panel).

In order to better understand the behavior of the different nucleation schemes we modeled different cases and compared them with the measurement at PDD. The results will be detailed in section 4.3.

The case studies investigated can be classified into three different categories:

i) days with nucleation events (March 25th, 2011, May 5th, 2011 and 7-8 April, 2008);

ii) days with weak nucleation events (March 26th, 2011 and February 25th, 2009);

iii) days with no nucleation event (March 8th, 2009).

For all cases we analyze the difference between the Kulmala and the Vehkamaki schemes. Due to computational costs, the impact of the organics scheme is analyzed only for two nucleation events (March 25th, 2011 and May 5th, 2011), and the weak nucleation event on March 26th, 2011.

4.3.1 Nucleation event days

4.3.1.1. March 25th, 2011 case

On March 25th, 2011, particles nucleation was registered at Puy de Dome summit. This nucleation event was also captured by the CHIMERE model.

The synoptic situation on 25 March 2011 is depicted in Fig. 4.6. During this day, the weather in Western Europe was mainly influenced by a high-pressure centered over central Europe.

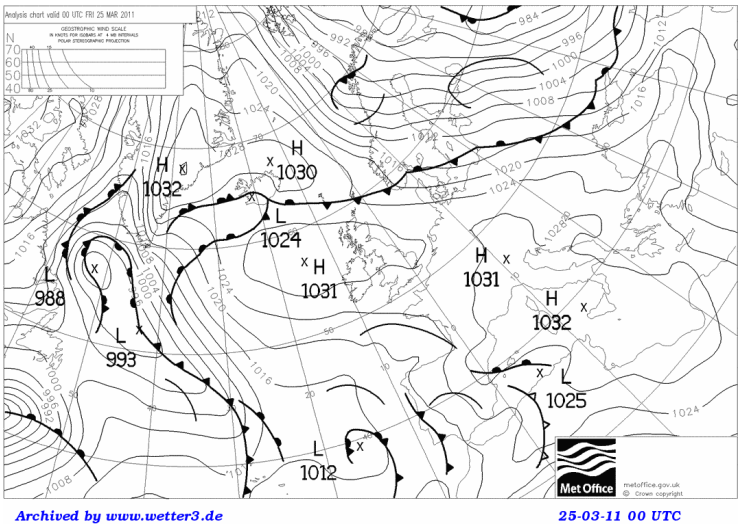

Figure 4.6. Synoptic situation at 25 March 2011, 00 UTC

The modeled temperature using the WRF model was generally weakly underestimated, the relative humidity however was overestimated as illustrated in Fig. 4.7.

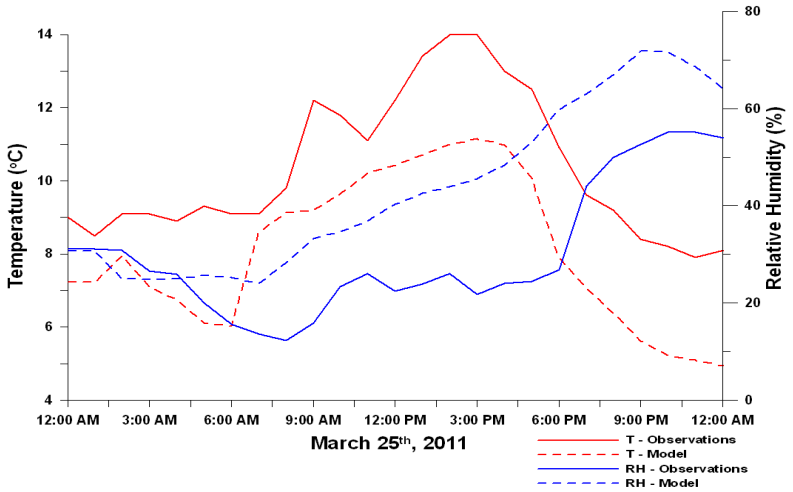

Figure 4.7. RH and T modeled and observed for 25 March 2011

The table 4.1 presents the results for March 25th, 2011, obtained applying the same statistic proposed by Reddington et al., 2011 when using the Kulmala, the Vehkamaki and the organics schemes. Because the secondary particle formation can give a significant contribution to cloud condensation nuclei (CCN) concentration (Spracklen et al, 2008, Makkonen et al, 2009, Merikanto et al, 2009) the summary statistics was made for: a) the total particle number concentration (D_p>10nm; N_{tot}) and b) for the number concentration in two different size ranges typical for CCN: D_p>50nm (N_{50}) and D_p> 100nm (N_{100}).

As can be seen in the Table 4.1 the normalized mean bias (NMB) gives similar values for the Kulmala and the Vehkamaki scheme, that underestimate the total particle number by 35%, while the organics scheme leads to higher underestimation (77%), even more pronounced for particles having the diameter larger than 50 nm (71%). The correlation factor R indicates a poor correlation between modeled and observed total particle number concentration. However the correlation is improved for particles with the diameter larger than 50 nm.

Table 4.1. Summary statistics for total particle number concentration (D_p>10nm; N_{tot}) and number concentration in two size ranges typical for CCN: D_p>50nm (N_{50}) and D_p> 100nm (N_{100}). The normalized mean bias (NMB) and correlation coefficient (R) are calculated between simulated and observed number concentration at PDD on March 25th, 2011

Model experiment	NMB (%)			R		
	N_{tot}	N_{50}	N_{100}	N_{tot}	N_{50}	N_{100}
Kulmala	-35.12	-17.99	-65.40	0.03	0.60	0.94
Vehkamaki	-34.17	-28.43	-68.11	0.01	0.25	0.85
Organics	-76.95	-71.26	-85.51	-0.12	0.51	0.40

The total particle number concentration is thus underestimated by a factor of 1.54 during the entire day for Kulmala scheme, by a factor of 1.51 for the Vehkamaki scheme and by a factor of 4.33 when the organics scheme is used. Again, the diurnal evolution of both simulations and measurements will give further details on when the underestimation occurs.

Figure 4.8 compares the hourly modeled and observed particles number size distribution at the PDD site. Observations show an increase of 10 nm particles at mid-day due to the new particle formation event, which, as usual, grow in size during the afternoon until they reach 20-25 nm at 18 UTC. The WRF-CHIMERE simulations also predict a large increase of 10 nm particles concentrations due to nucleation. The moment of nucleation, however, slightly differs: whilst the first ultrafine particles are detected by the instruments around 12 UTC, the Kulmala and the Vehkamaki schemes predict their appearance at 10 UTC and the organics scheme is not able to predict an increase in particle number in the nucleation mode.

We will investigate the causes for such a time delay in the initiation of the nucleation.

One possible explanation for initiation of the nucleation event can be the growth of PBL and vertical mixing with cleaner air from aloft. Figure 4.8 b), c), and d) shows that during morning hours the maximum modeled concentration occurs in the Aitken mode ranging between 30 and 70 nm. Between 07 and 09 UTC this mode disappears due to the break-up of the stable nocturnal boundary layer, followed by rapid dynamic vertical mixing, prior to the onset of nucleation, and subsequent dilution with cleaner air from higher altitudes (see Fig. 4.9). Therefore, the sink for condensing material and clusters is reduced and new particle formation and subsequent growth can start. We may speculate that mixing processes at the inversion play an important role and initiated the nucleation events.

Hence, the model may predict nucleation and growth of aerosol particles at an earlier time than in the observation, due to the simulation of an increase in BPL height at 09 UTC. Unfortunately, at that time, we did not have information on the PBL height measured with the LIDAR located in Clermont-Ferrand, and thus we can not verify this hypothesis.

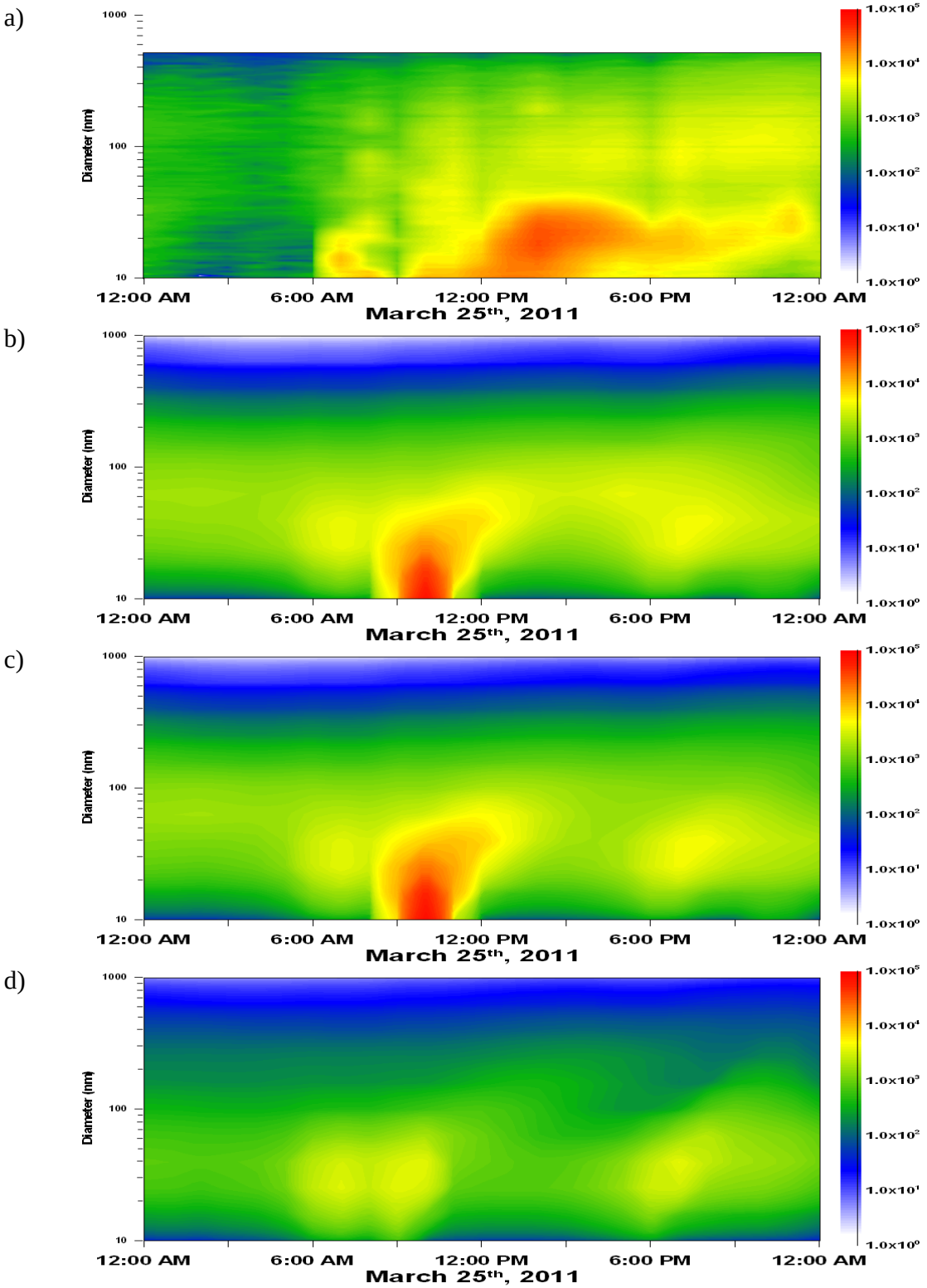

Figure 4.8. Hourly number size distribution: a) Observation; b) Kulmala scheme; c) Vehkamaki scheme; d) Organics scheme.

Another aspect is that the model does not capture very well is the growth of the newly formed particles. If there is a clear formation of nucleation mode particles at the lower limit (10 nm), the mode does not show a very clear growth (Fig. 4.8 b, and c). Instead, the particles disappear as soon as they are formed. This disappearance might be explained by the strong mixing of air masses. Another possible explanation for the continuous growth observed in the measurements but not in the model is related to the fact that the observed growth is taking place in the nocturnal residual layer, and the model can not simulate this residual layer.

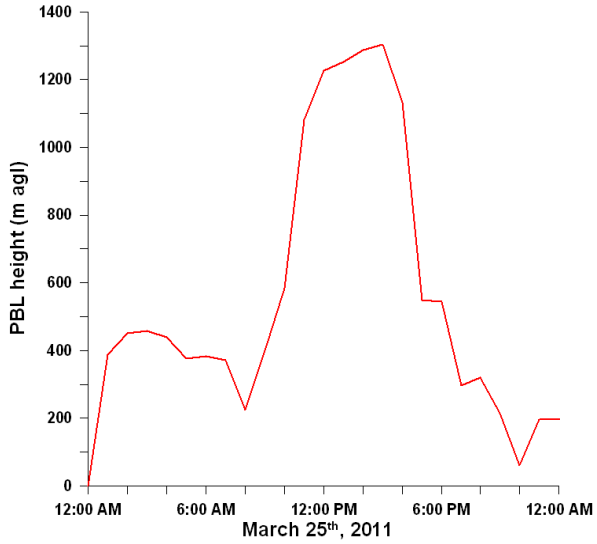

Figure 4.9. Planetary boundary layer predicted with WRF model

The fact that the growth of particles is observed to be continuous through the day at a given point (the Puy de Dome station) indicates that the nucleation and growth is spatially homogeneous over the regional scale. For the 25th of March, a 4 hours duration event indicates that the event occurred more than 150 km away from the PDD summit .To investigate this aspect, backward trajectory plots were generated. Figure 4.10 shows the backward trajectory arriving at PDD at 10 UTC on this day (350 m agl) using the WRF meteorological model for the inner-most domain. This was performed in order to observe the direction and altitude of the air mass prior to the nucleation event. The modeled air mass originated from a remote region in the south, in which a high number of particles had already formed, confirming the spatial scale of nucleation and growth, for an air mass which followed the terrain height, at 500 m about ground level.

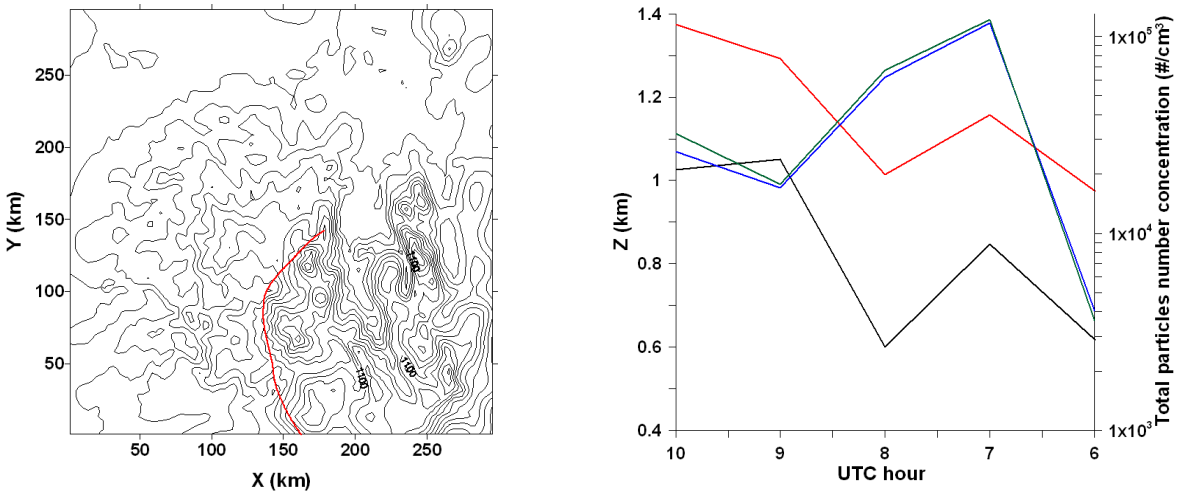

Figure 4.10. Backward trajectory ending at 10 UTC 25 March 2011 (left part) and altitude of the air mass together with total particle number concentration (right part; black line represents the terrain height, red – the air mass altitude, blue – PNC (particle number concentration) for Kulmala scheme, green – PNC for Vehkamaki scheme)

In the following study case, the nucleation event was observed at PDD summit, however all nucleation schemes failed in reproducing the occurrence of the event.

4.3.1.2. May 5th, 2011 case

The synoptic situation on 5 May, 2011 is depicted in Fig. 4.11. During this day, the weather in Western Europe was, as for the previous case, mainly influenced by a high-pressure system centered over central Europe.

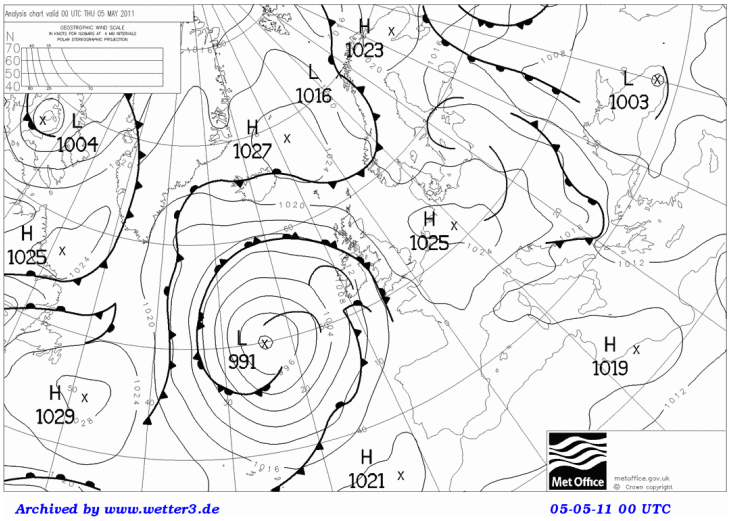

Figure 4.11. Synoptic situation at 5 May 2011, 00 UTC

The modeled temperature using the WRF model was slightly underestimated having a daily bias of -0.38 ^{o}C. Unfortunately, because the relative humidity is not available in the observation chain for this day, we don't have the possibility to asses the model performance for this parameter (see Fig. 4.12).

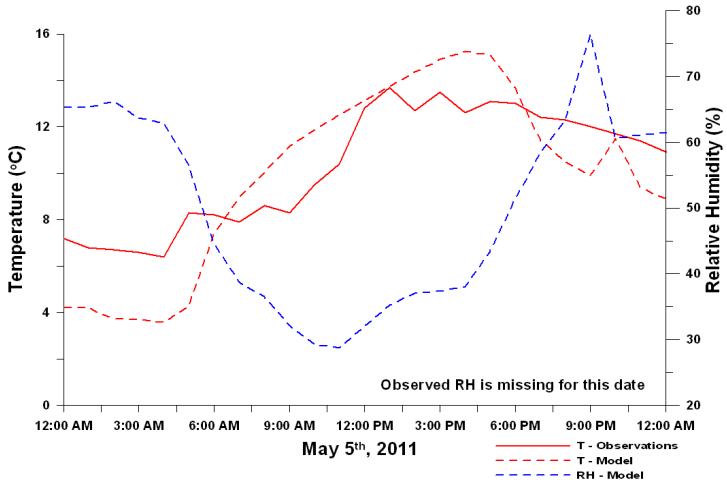

Figure 4.12. RH and T modeled and observed for 25 March 2011

For the case of May 5th, 2011, nucleation and new particle formation was also observed at Puy de Dome summit (Figure 4.13a). Indeed, one can observe that high concentrations of particles appear at the lower end of the diameter size range of the SMPS (10 nm) around 12 UTC and that these particles grow in size in the course of the day, until reaching about 30 nm in the middle of the night. The fact that the growth of particles is observed to be continuous through the day at a given point (the Puy de Dome station) indicates that the nucleation and growth is spatially homogeneous over the regional scale. For the 5th of May, a 12 hours duration event indicates that the event occurred a quit large area of several hundred kilometers in x and y extension. Using different nucleation schemes in the CHIMERE model, we observe that the model fails this time to reproduce the occurrence of the event for all nucleation schemes involved in calculation (Figures 4.13b to 4.13d).

Table 4.2. Same as Table 4.1 on May 5th, 2011

Model	NMB (%)			R		
experiment	N_{tot}	N_{50}	N_{100}	N_{tot}	N_{50}	N_{100}
Kulmala	-50.38	-38.19	-75.52	0.09	0.26	0.42
Vehkamaki	-58.91	-63.46	-58.38	0.17	0.21	0.38
Organics	-69.94	-72.59	-82.19	-0.22	0.24	0.44

The NMB for the total particle concentration gives similar values for the Kulmala and the Vehkamaki scheme, while for the organics scheme the underestimation is more accentuated. This behavior can be observed also in the case of N_{50} and N_{100}. The correlation factor indicates a poor correlation for all sizes ranges, event though the best correlations are achieved for the N100 which represent accumulation mode particles, transported over large distances and more independent from nucleation.

We will investigate here the possible causes for the model not to capture the nucleation and early growth.

New particle formation is believed to be linked to sulfuric acid, hence to the formation of OH radicals via photolysis (e.g. Berresheim et al., 2002; Arakaki et al., 2006). The predicted meteorological parameters as solar radiation, which regulates the intensity of photochemical reactions and the formation of OH in the atmosphere, and low relative humidity (see Fig. 4.14, right part) indicate that the thermo-dynamical conditions to achieve nucleation are fulfilled. However, the modeled total particles number concentration do not show any notable change in the hourly evolution. Because the atmospheric H_2SO_4 particle formation is related to the gas-phase reaction of OH radicals with SO_2, a possible explanation can be related to the low concentration of H_2SO_4. As can be seen in Fig. 4.14 (left part) the modeled SO_2 concentration is largely underestimated during noon time when nucleation took place accordingly to Fig. 4.13a, this implies that the modeled H_2SO_4 concentrations are likely underestimated.

In order to explain why on March 25th, 2011 the model succeeded to capture the observed nucleation event and on May 5th, 2011 failed in reproducing the observed event we calculated the H_2SO_4 proxy proposed by Petaja et al. (2009). Hence,

$$\Pr oxy([H_2SO_4)] = k * \frac{SO_2 * UVB}{CS}, \qquad (4.10)$$

where *UVB* represents a part of the solar radiation, and *CS* is the condensational sink provided by the pre-existing aerosol particle population. Because the observed solar radiation data are missing for this date, we are not able to calculate the H_2SO_4 proxy for PDD from the observation, but we can calculate H_2SO_4 using the proxy on simulated SO_2 and radiation.

As can be seen in Fig. 4.15, around noon when the SMPS detects the ultrafine particles, we can observe that the calculated H_2SO_4 concentrations for May 5^{th}, 2011 is lower by a factor of 2 in comparison with the calculated H_2SO_4 concentrations for March 25^{th}, 2011. A low sulfuric acid concentration would be a major cause for nucleation not to occur in the simulation of May 5^{th}. The differences in the temperature and relative humidity during noon time between these days are not large, so we can conclude that the underestimation of modeled H_2SO_4 concentrations might be a major factor leading to this model behavior.

.

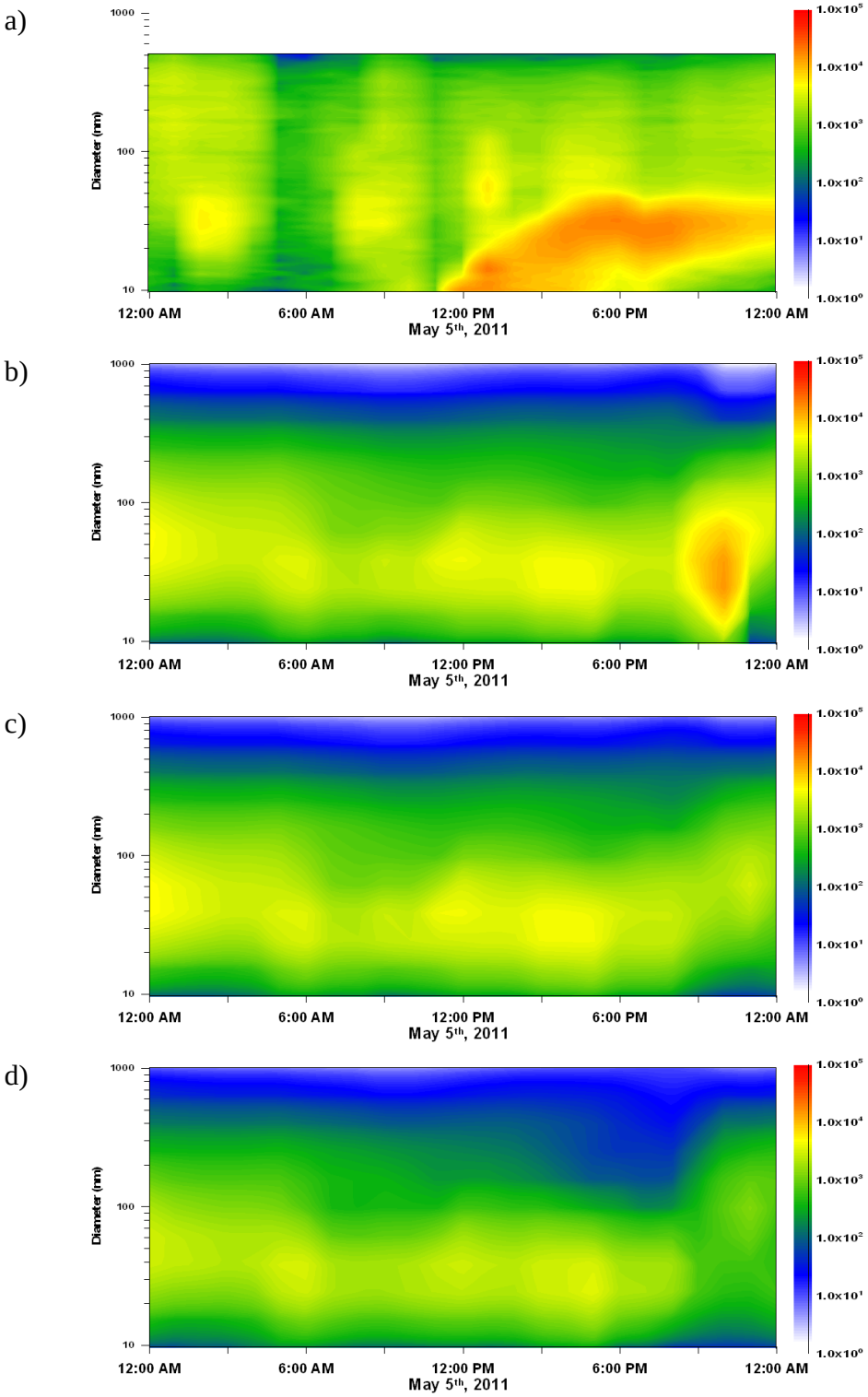

Figure 4.13. Hourly number size distribution: a) Observation; b) Kulmala scheme; c) Vehkamaki scheme; d) Organics scheme.

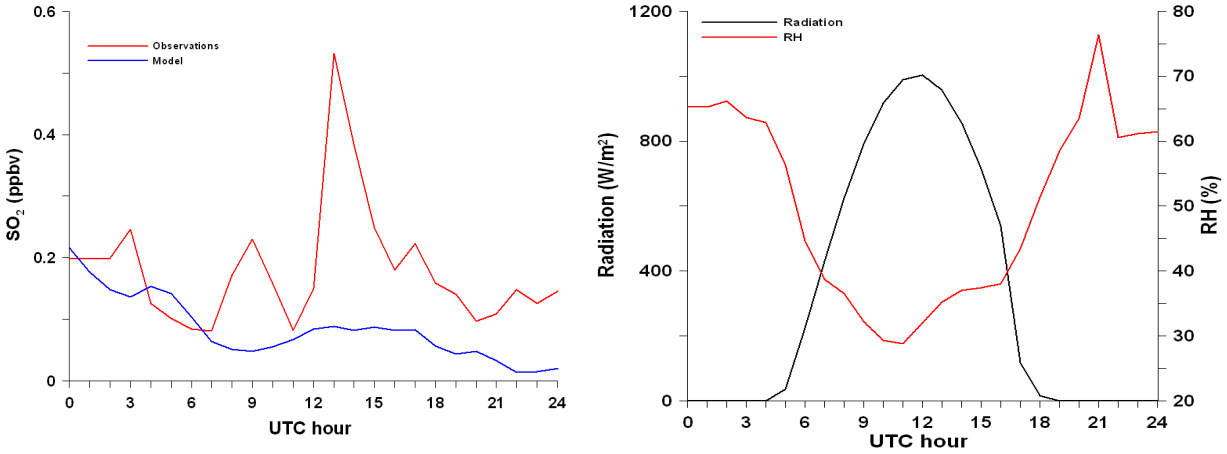

Figure 4.14. Modeled and observed SO_2 concentration (left part) and modeled solar radiation and relative humidity (right part) on May 5th, 2011

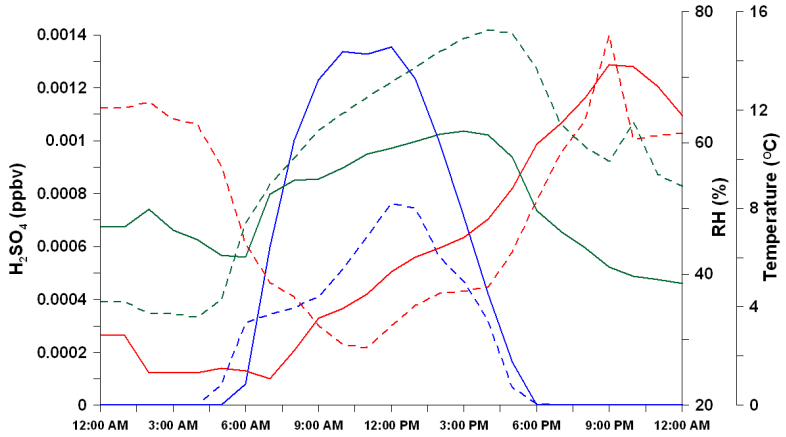

Figure 4.15. Modeled values for H2SO4 (blue line), relative humidity (red line) and temperature (green line) on March 25th, 2011 (solid lines) and May 5th, 2011 (dashed lines).

For the entire 24 h simulation all nucleation schemes work in the same manner, however, at 22 UTC the modeled particles concentration for the Kulmala scheme presents an increase in the Aitken mode which is not captured by the Vehkamaki and the organics scheme. To investigate the possible causes associated with this increase in the number concentration, backward trajectory plots using the WRF meteorological model for the inner-most domain were calculated. Fig. 4.16 (left panel) shows the backward trajectory calculated for PDD arriving at 22 UTC at 350 m agl. The modeled air mass prior to the instant of particle increase detected in Fig. 4.13b comes from southern direction and it is accompanied by a very high particle number concentration when the Kulmala scheme is applied in CHIMERE model. The particle number

concentration transported by CHIMERE using the Vehkamaki scheme however decreases in the same time period (see Fig. 4.16 right panel). The backward trajectories indicate that the air mass did not follow the terrain height this time, but originates from higher altitude back in time. Thus, we can conclude that the presence of the particle concentration peak is associated with the advective transport of particles and the ongoing nucleation processes developed differently at higher altitudes, and might be due to different dependence to the temperature.

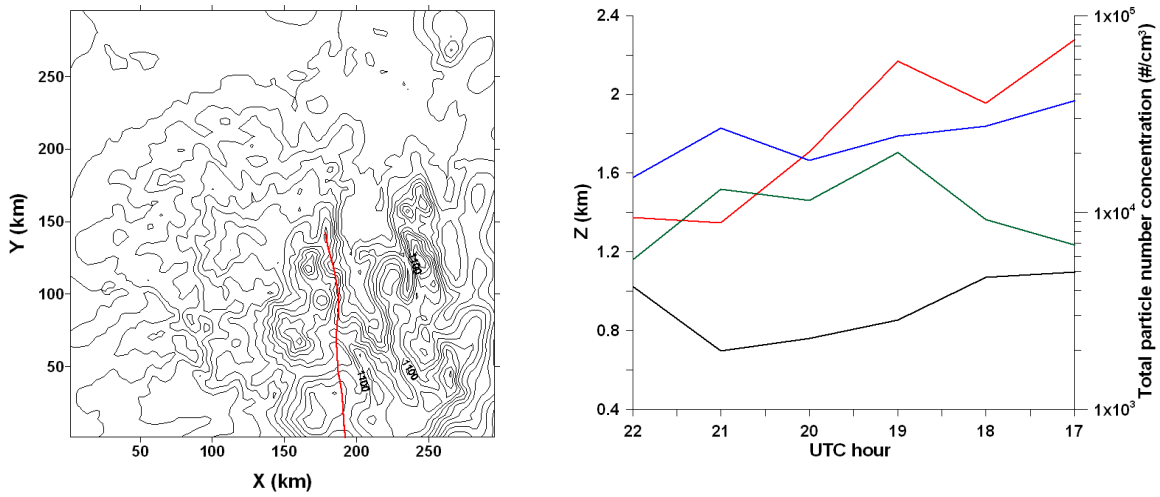

Figure 4.16. Backward trajectory ending at 22 UTC, 5 May 2011 (left part) and altitude of the air mass together with total particle number concentration (right part; black line represents the terrain height, red – the air mass altitude, blue – PNC for Kulmala scheme, green – PNC for Vehkamaki scheme).

4.3.1.3. 7-8 April 2008 case

A third clear nucleation event occurred during the period of study on 7-8 April 2008. The synoptic situation on 7 April 2008 is depicted in Fig. 4.17. During this day, the weather in Western Europe was mainly influenced by a low-pressure system ranging from North Sea over France to the Mediterranean Sea. The Puy de Dome site was influenced by this low-pressure system with its frontal system and moderate winds from southerly directions and cloudy weather prevailed on 7 - 8 March 2008. The temperature was overpredicted by about 3 ^{O}C for the entire day (see Fig. 4.18). The mean observed wind speed was 5.77 m/s and the modeled wind speed was 5.20 m/s, with a correlation factor of 0.67. The correlation factor between observed and

modeled wind direction is 0.87, with a mean observed wind direction of 183.11^{o} and a modeled one of 202.22^{o} C.

The conditions for the atmospheric flow are thus well described by the model.

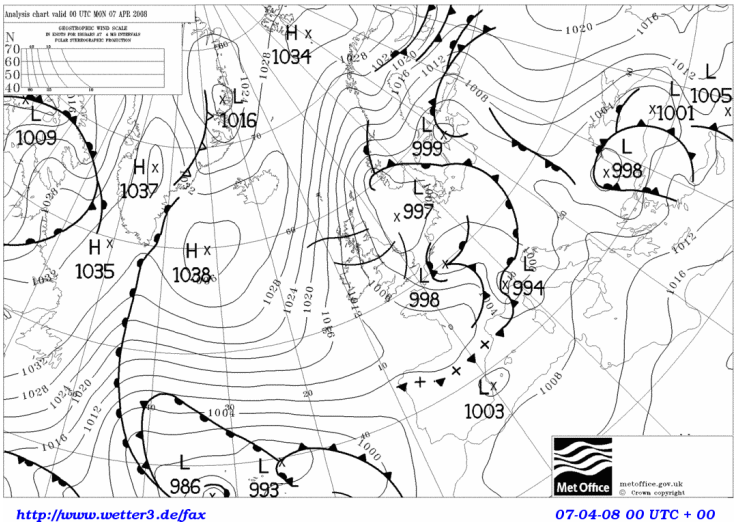

Figure 4.17. The synoptic situation on April 7th, 2008 at 00 UTC

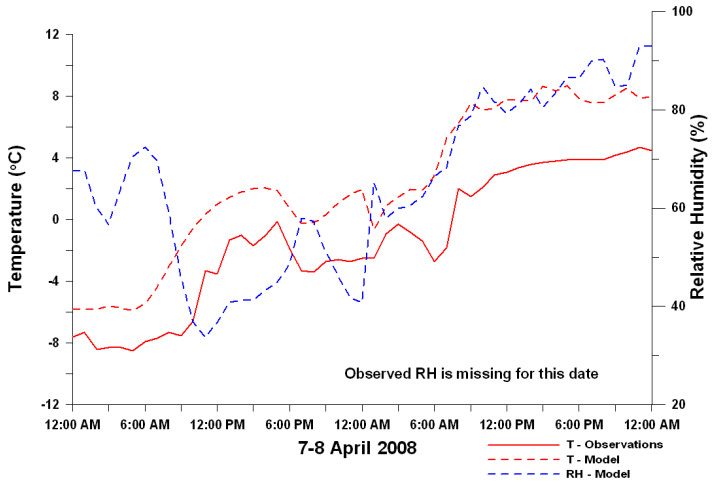

Figure 4.18. RH and T modeled and observed for 7-8 April 2008

The Table 4.3 presents the result for 7-8 April 2008, obtained by applying the same statistics used before. We noticed that the Kulmala scheme leads to high overestimations for N_{tot} and N_{50} (NMB=1451.07%, respectively NMB=229.03%) in comparison with the Vehkamaki scheme

(NMB=620.89%, respectively NMB=131.38%), while for N_{100} both schemes have similar values.

Table 4.3. Same as Table 4.1 on 7-8 April 2008

Model	NMB (%)			R		
experiment	N_{tot}	N_{50}	N_{100}	N_{tot}	N_{50}	N_{100}
Kulmala	1451.07	229.03	-70.88	-0.27	0.32	0.74
Vehkamaki	620.89	131.38	-66.61	-0.11	0.15	0.68

Figure 4.19 compares the hourly modeled and observed number size distribution at PDD site. Both nucleation schemes involved in the calculation of CHIMERE model failed to reproduce the nucleation event observed at Puy de Dome summit. The total particle number concentration is overestimated within a factor of 15.51 for the Kulmala scheme, respectively 7.20 for Vehkamaki scheme.

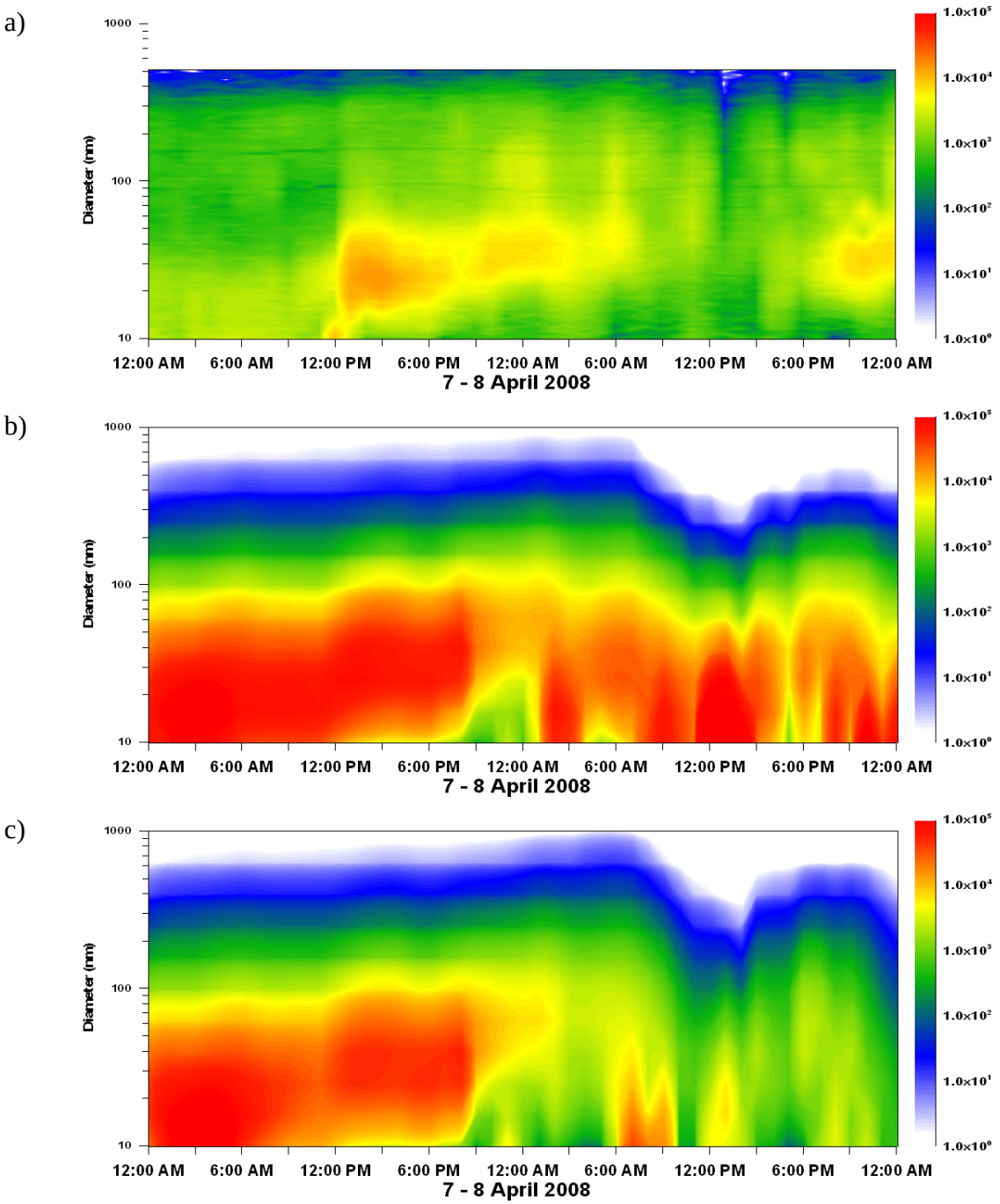

Figure 4.19. Hourly number size distribution: a) Observation; b) Kulmala scheme; c) Vehkamaki scheme.

A possible explanation for the high total particle concentration obtained using the Kulmala scheme compared with the Vehkamaki scheme can be related to the meteorological parameters. Besides precursors gases concentrations, a key parameter that determines if nucleation and

growth occurs or not in the atmosphere is the condensational sink represented by pre-existing particle. The increase of particle number concentration in the nucleation mode for the Kulmala scheme, especially on April 8th, 2008, can be associated with the occurrence of precipitation modeled by the WRF model (see Fig. 4.20). However, the rain was not observed at PDD.

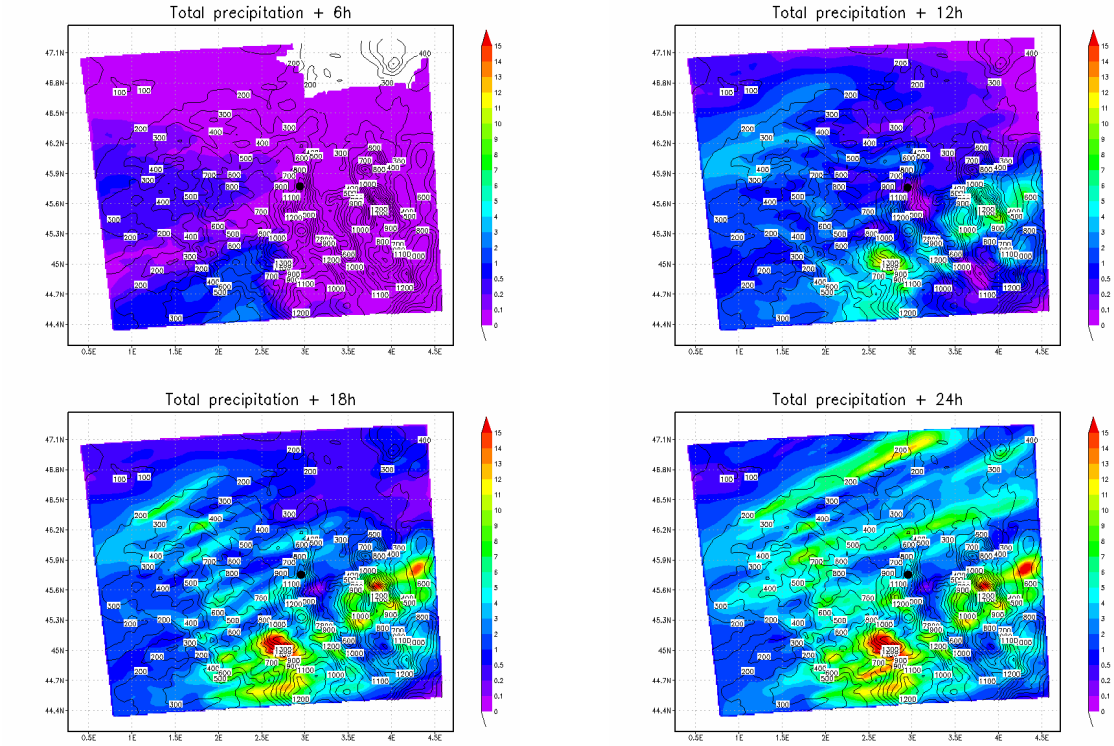

Figure 4.20. Total accumulated precipitations at every 6h for April 8th, 2008. The black point indicates the PDD location

High relative humidity values contribute to the growth of pre-existing particles by condensation of water vapor, and eventually their wet scavenging by cloud droplet activation. This can explain the lack of particle larger than 100 nm (a NMB of -70.88% for the Kulmala scheme, respectively –66.61% for the Vehkamaki scheme) and is sustained by the accumulated precipitation field predicted by the WRF model (see Fig. 4.20). Hence, because the model is overpredicting aerosol scavenging by cloud and rain, it underpredicts the number of large particles, thus the condensational sink. Because the condensational sink is too low in the model, nucleation is predicted unrealistically high.

We are now going to investigate the model behavior for a case study when weak nucleation occurs.

4.3.2. Weak nucleation event days

4.3.2.1. February 25th, 2009 case

On February 25th, 2009, a weak nucleation event was observed at Puy de Dome summit, but the intensity of this phenomenon was much higher when the Kulmala and the Vehkamaki schemes are used.

The synoptic situation on February 25th, 2009 is presented in Fig. 4.21. The weather in France was influenced by a high pressure belt. The relative humidity simulated using the WRF model is underestimated (daily BIAS of 9.33 %). In the first part of the day underestimates the observation of relative humidity up to -28.01 %, but after 12 UTC the model starts to overestimate the observations of relative humidity up to 60.40 % (see Fig. 4.22). This is also reflected in the weak correlation coefficient of 0.46. The modeled temperature has a daily BIAS of -0.74 ^{o}C, with a correlation coefficient of 0.86. As the observations for wind speed and direction are not available for this day, we cannot assess the model performance for these parameters.

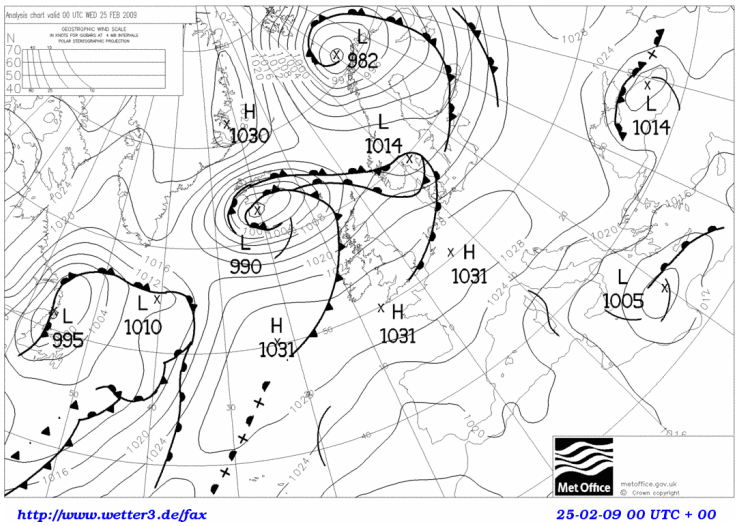

Figure 4.21. The synoptic situation for February 25th, 2009 at 00 UTC

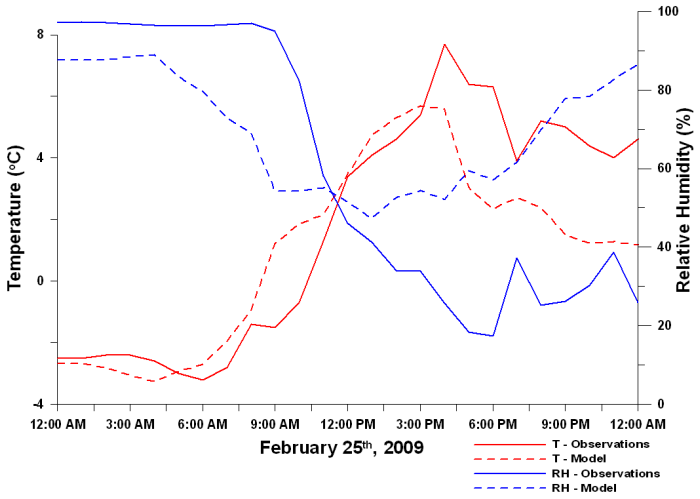

Figure 4.22. RH and T modeled and observed for February 25th, 2009

The NMB for total particle concentration and particles having the diameter larger than 50 nm gives high overestimation especially for the Kulmala scheme, while for the particles having the diameter larger than 100 nm both schemes used in the CHIMERE underestimate the observations (see Table 4.4). The correlation factor shows no correlation for all sizes range, except for N_{tot} in the case of the Kulmala scheme, when a weak negative correlation can be seen.

Table 4.4. Same as Table 4.1 on February 25th, 2009

Model	NMB (%)			R		
experiment	N_{tot}	N_{50}	N_{100}	N_{tot}	N_{50}	N_{100}
Kulmala	910.10	117.05	-73.25	-0.28	0.02	0.12
Vehkamaki	314.71	34.39	-76.06	-0.05	0.14	0.01

On February 25th, 2009, the hourly observed particles number size distribution indicate a weak nucleation event at Puy de Dome summit in the morning hours around 09 UTC and subsequent particle growth until noon. Simulations with the Kulmala and the Vehkamaki schemes predict extremely strong nucleation which starts for Kulmala at 01 UTC and for Vehkamaki just after sunrise (see Fig. 4.23).

The total number concentration is overestimated by the Kulmala scheme by a factor of 10.10 when we compared over the entire observational period and by a factor of 4.14 when the Vehkamaki scheme is used.

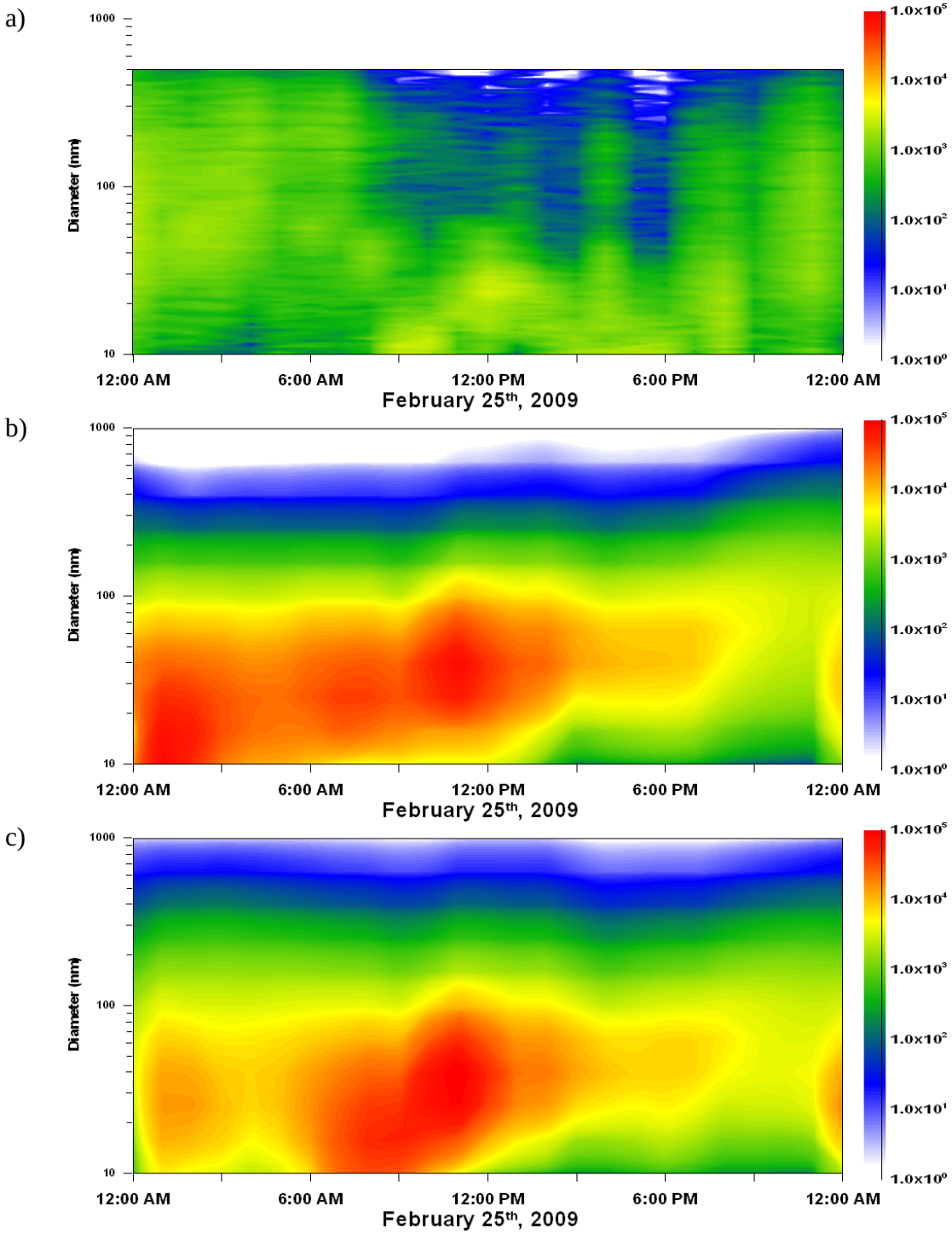

Figure 4.23. Hourly number size distribution: a) Observation; b) Kulmala scheme; c) Vehkamaki scheme.

A possible explanation for the modeling results can be the high amount of SO_2 predicted by the CHIMERE model which contributes significantly to the formation of gaseous H_2SO_4. The

simulated SO_2 concentration is illustrated in the Fig. 4.24 (left panel) and demonstrates a strong overestimation of SO_2 during night until 14 UTC by the simulation.

Also, the high relative humidity predicted for the first part of the day and the nucleation event modeled by the Kulmala scheme suggests, as already observed for the previous case that when cloud scavenging might occur, the use of the Kulmala scheme results in high number of particles in the nucleation mode. The decrease of the relative humidity and increase of the solar radiation modeled by WRF (see Fig. 4.24 right panel) enhance the nucleation predicted by the Vehkamaki scheme. As can be observed from Fig. 4.23 the nucleation onset predicted by Vehkamaki scheme corresponds to the one observed, however the intensity of phenomena leads to an overestimation by a factor of 53.90 within the observation for the particles having the diameter smaller than 50nm.

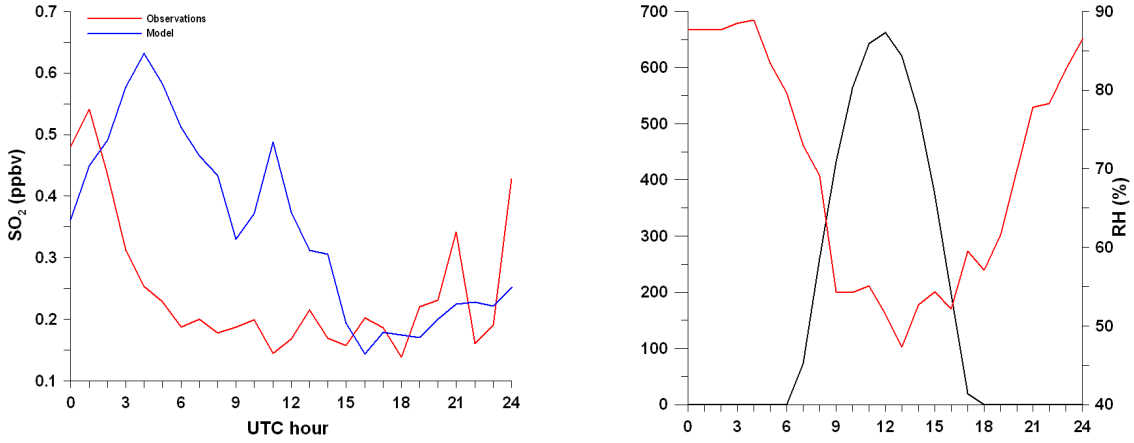

Figure 4.24. Modeled and observed SO_2 concentration (left panel) and modeled solar radiation and relative humidity (right panel) for February 25th, 2009.

4.3.2.2. March 26th, 2011 case

Another case of weak nucleation was observed on March 26th. The meteorological model WRF underestimates the temperature mainly during the night (see Fig. 4.25). The temperature bias for entire period simulation is -1.35 ^{o}C only. The relative humidity is overestimated, with a daily bias of 12 %.

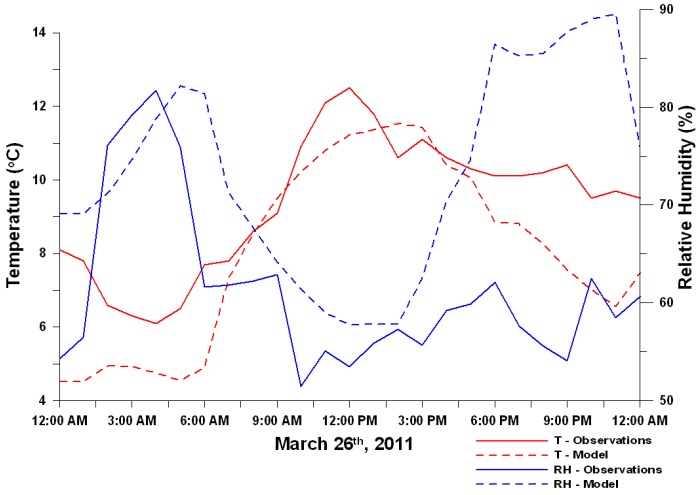

Figure 4.25. RH and T modeled and observed for 26 March 2011

Figure 4.26 compares the hourly modeled and observed particles number size distribution at PDD site. A weak production of ultrafine particles from 11 to 18 UTC can be seen from SMPS measurements. This event is globally reproduced by the Vehkamaki and the organics schemes. Both simulations have a delay in time for prediction of the growth in the Aitken mode due to transport, although the ultrafine particles production is not reproduced by either of the scheme mentioned before. In comparison with the Vehkamaki and the organics schemes, the Kulmala scheme predicts nucleation in the afternoon with a higher intensity. The total particles number concentration during the entire day is overestimated by a factor of 2.66 for Kulmala scheme, while for the Vehkamaki and the organics scheme the modeled results obtained with CHIMERE model gives an underestimation by a factor of 1.61, respectively 3.16.

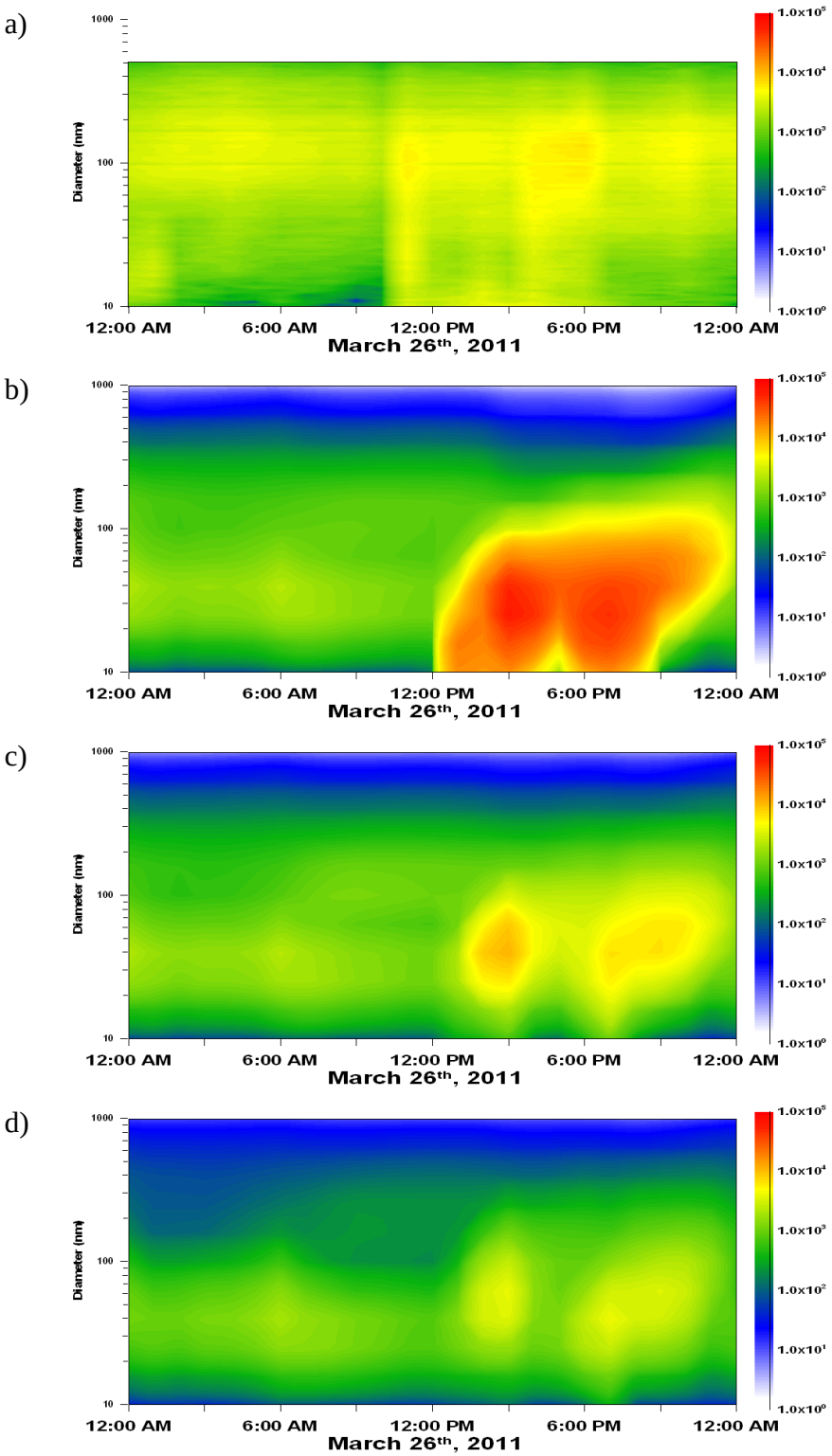

Figure 4.26. Hourly number size distribution: a) Observation; b) Kulmala scheme; c) Vehkamaki scheme; d) Organics scheme.

This can also be seen in the Table 4.5. For particles having a diameter larger than 50 nm we obtain underestimations for all schemes used, more accentuated for the Vehkamaki and the organics scheme, keeping the same trend like for N_{tot}, while NMB for N_{100} gives similar values for all schemes. The correlation factor for N_{tot}, N_{50} and N_{100} shows a poor correlation.

Table 4.5. The same as Table 4.1 on March 26th, 2011

Model experiment	NMB (%)			R		
	N_{tot}	N_{50}	N_{100}	N_{tot}	N_{50}	N_{100}
Kulmala	166.23	-14.09	-81.92	0.48	0.42	-0.05
Vehkamaki	-37.70	-56.89	-81.66	0.30	0.28	0.12
Organics	-68.41	-77.71	-90.12	0.20	0.21	0.27

There is a strong bias of the Kulmala scheme due to the fact that nucleation is predicted while it is not observed, leading to high overestimations of the PNC. We will investigate the possible causes for the wrong prediction of nucleation using this scheme.

Fig. 4.27 and Fig. 4.28, give horizontal cross section for the first model level for modeled mass and number concentrations for particles having the diameter higher than 100 nm. The left column in both figures gives the results using with the Kulmala scheme, the right column those with the Vehkamaki scheme. Strong discrepancies in the number concentration of these particles between both schemes are most prominent at 18 UTC. The analysis of the meteorological situation simulated by WRF shows a large coverage of precipitation (Fig. 4.29), which already started at 12 UTC in the center of the domain. We can thus conclude that high relative humidities were present over large parts of the model domain, especially in the center where the Puy de Dome is located. The meteorological conditions favor the removal of particles larger than 100 nm from the atmosphere mainly by scavenging of raindrops. Due to the low concentration of accumulation mode particle condensation of atmospheric trace gases onto these particles is weak or non-existing. Consequently the prevailing trace gases can favor nucleation of new particles, especially using the Kulmala scheme.

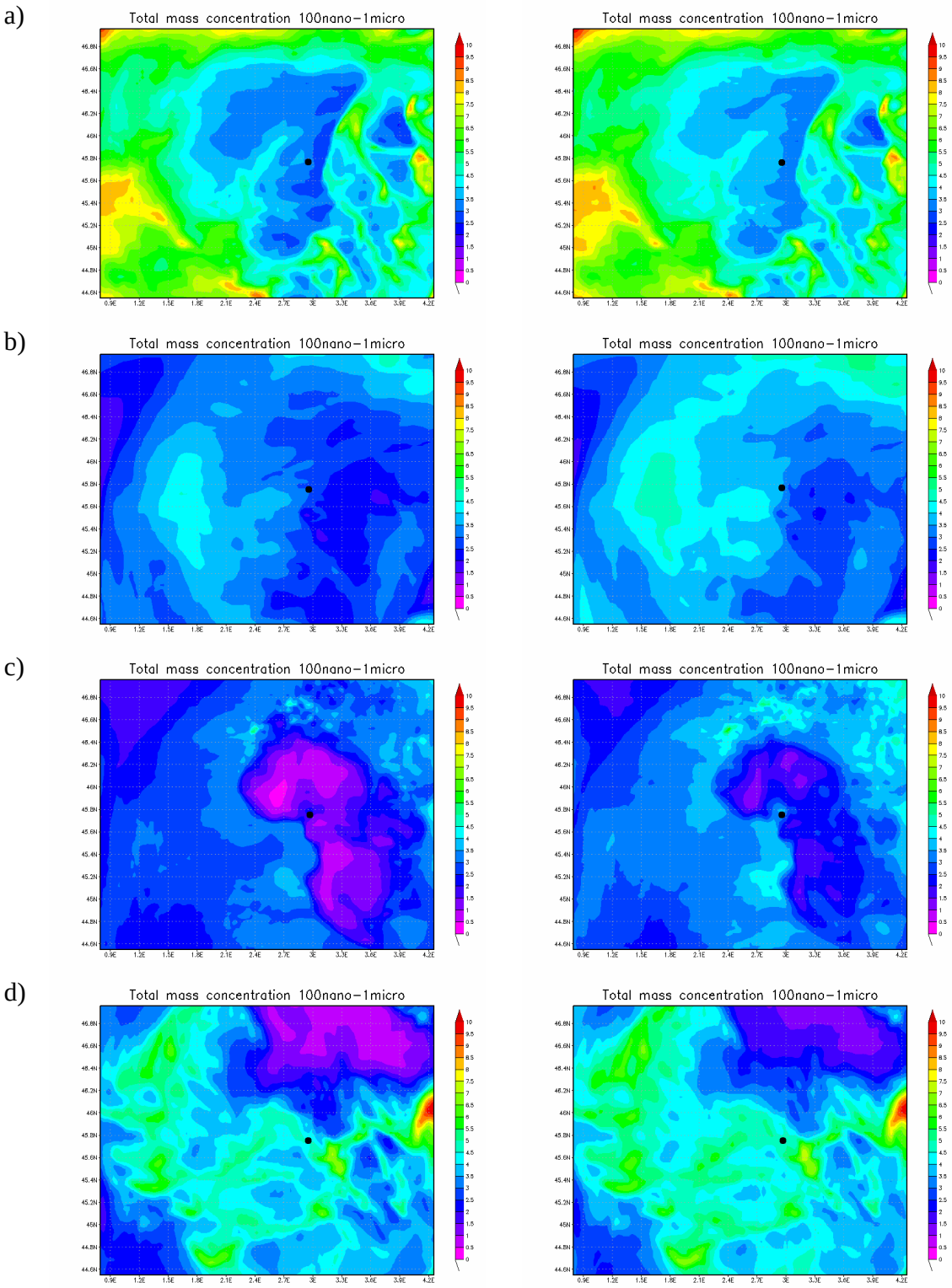

Figure 4.27. Total mass concentration for particles having the diameter larger than 100nm for Kulmala scheme (left part) and Vehkamaki scheme (right part) at every 6 hours for March 26th, 2011: a) 06 UTC; b) 12 UTC; c) 18 UTC; d) 24 UTC

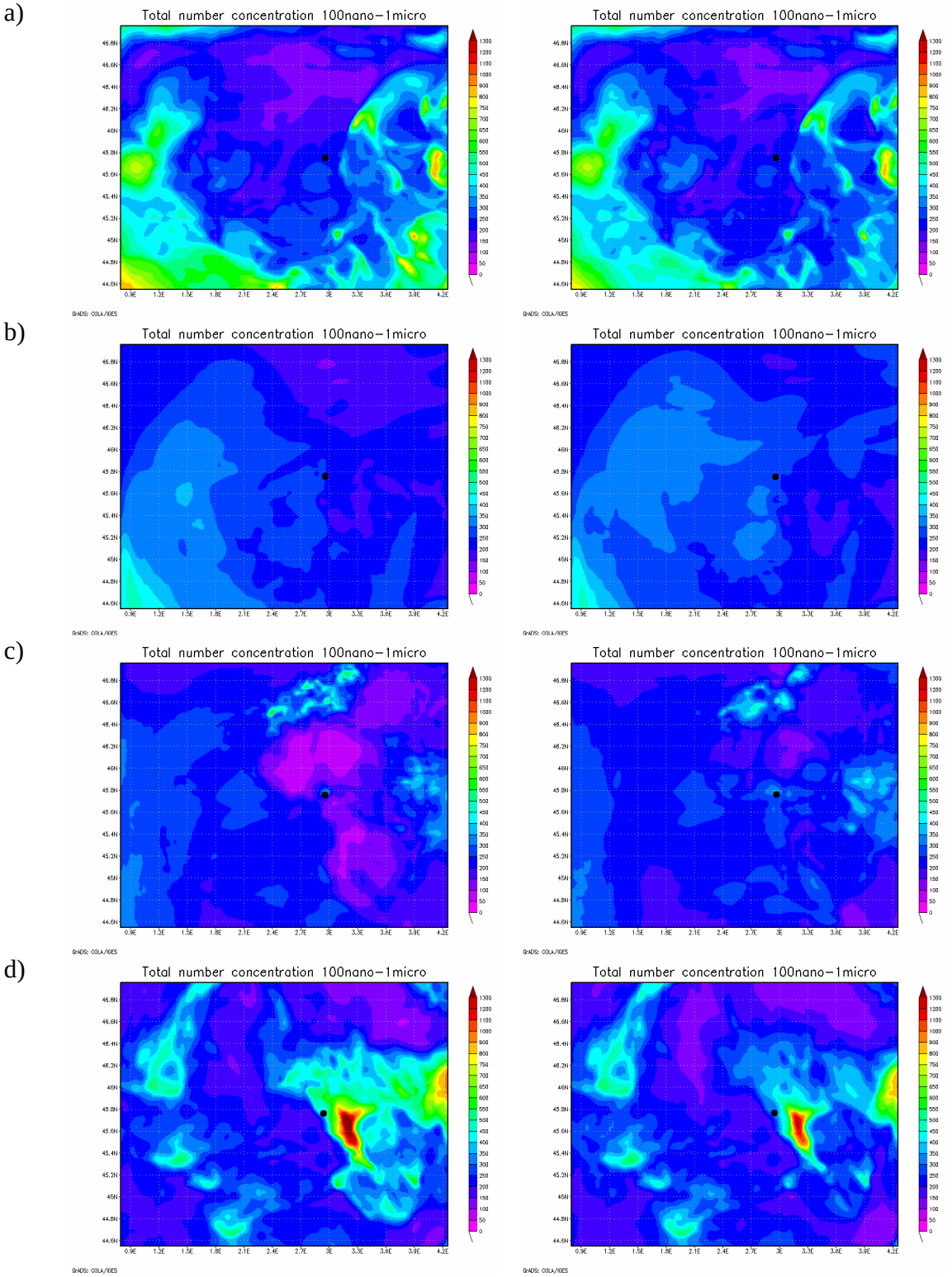

Figure 4.28. Total number concentration for particles having the diameter larger than 100nm for Kulmala scheme (left part) and Vehkamaki scheme (right part) at every 6 hours for March 26th, 2011: a) 06 UTC; b) 12 UTC; c) 18 UTC; d) 24 UTC

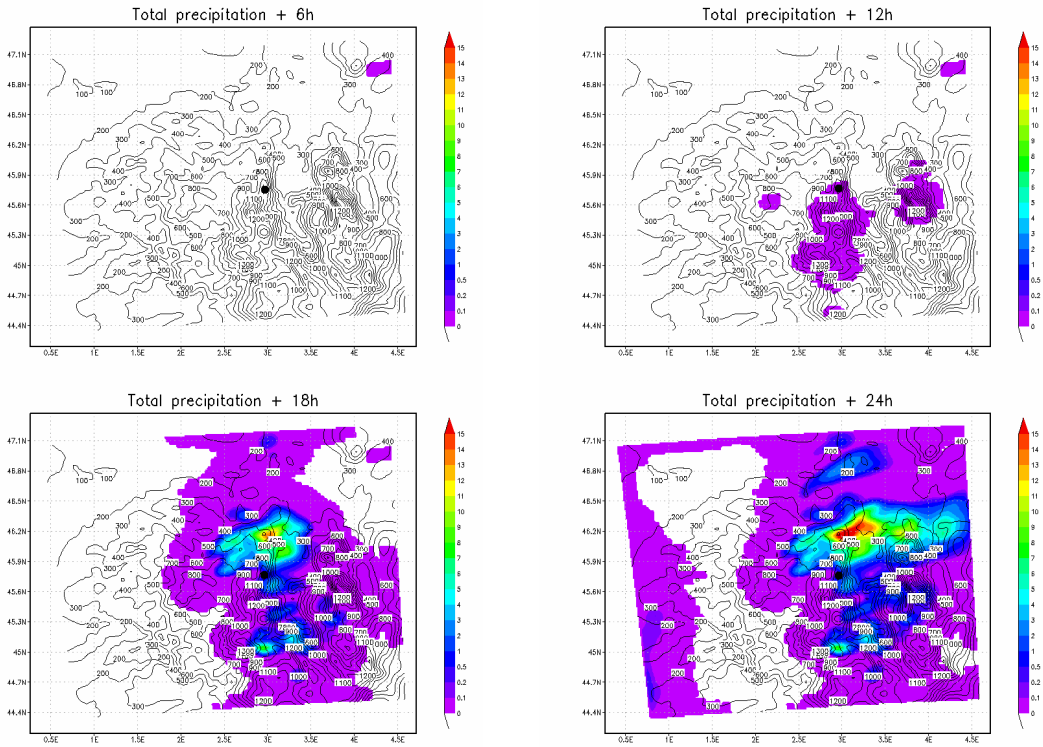

Figure 4.29. Total accumulated precipitations at every 6h for March 26th, 2011. The black point indicates the PDD location

As already mentioned before, and it will be also discussed for 8th March 2009 case (see section 4.3.3), the increase of modeled relative humidity (Fig. 4.25) and the apparition of precipitation (Fig. 4.29) enhance the nucleation modeled with the Kulmala scheme, suggesting that might be a problem for this scheme when high relative humidities and precipitations are predicted.

4.3.3. No nucleation event day

4.3.3.1. March 8th, 2009 case

On March 8th, no nucleation was detected by the instruments at the PDD station. This case was chosen because during the entire intensive campaign the modeled results of total particle number concentration are largely different in comparison with the measurements (3 orders of magnitude for the Kulmala scheme and one order of magnitude for the Vehkamaki scheme). The synoptic situation on 8 March 2009 is depicted in Fig. 4.30. During this day, the weather in Western Europe was mainly influenced by a low-pressure system ranging from Iceland over Great Britain

to the south of the France. This low-pressure system with its frontal system west of the measurement site had influence on the weather at the experimental site. Moderate winds from westerly directions and cloudy weather prevailed on 8 March 2009. The mean observed wind speed was 12.43 m/s and the modeled one was only 7.33 m/s. This difference is certainly due to the coarse grid resolution in WRF which is does not allow to simulate correctly the wind acceleration when the air flows over the PDD summit. The observed western wind direction agrees well with the modeled one.

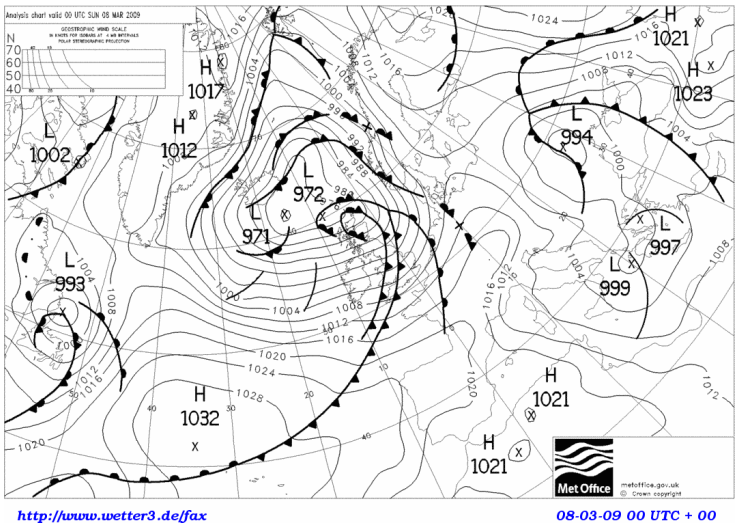

Figure 4.30. The synoptic situation for March 8th, 2009 at 00 UTC

Figure 4.31 compares the hourly modeled and observed number size distribution at the PDD site. The very low number concentrations measured at the site are typical for cloudy conditions and representative of a washed out atmosphere. In the simulations resulting from the CHIMERE model, the Kulmala scheme is giving a high number concentration in the nucleation mode in comparison with the SMPS measurements, while for the Vehkamaki scheme the overestimation is reduced. The total particle number concentration is overestimated within a factor of 216.86 for the Kulmala scheme, whilst the overestimation is reduced to a factor of 5.48 when the Vehkamaki scheme is used. A sensitivity test for this case was made omitting completely the nucleation process in CHIMERE. The result shows an overestimation of total particle number concentration within a factor of 6.51, which is very close to the results obtained using the Vehkamaki scheme. Thus, we can conclude that: i) particle nucleation was not solely the cause of overpredicted particle number concentrations; ii) other processes active in CHIMERE must be

responsible for the appearance of ultrafine particles during several time periods on 8th to 9th March 2009 (see Fig. 4.31c).

The table 4.6 presents the result for March 8th, 2009, obtained applying the same statistic used before.

Table 4.6. The same as Table 4.1 on March 8th, 2009

Model experiment	NMB (%)			R		
	N_{tot}	N_{50}	N_{100}	N_{tot}	N_{50}	N_{100}
Kulmala	21586.06	730.96	-6.26	-0.44	0.62	0.56
Vehkamaki	448.90	76.92	-38.82	-0.04	0.62	0.51
w/o nucleation	551.71	75.95	-52.44	0.06	0.66	0.53

A possible explanation for the high total particle concentration NMB obtained using the Kulmala scheme (21586.06%) compared with the Vehkamaki scheme (448.90%) can be related, again, to the meteorological parameters. The relative humidity modeled using WRF model is weakly underestimated but remains quite close to 100% (see Fig. 4.32). The modeled temperature fits the observations quite well.

As for cases of March 25th, 2011 and 7-8 April 2008, the high relative humidity modeled values contribute to the growth of pre-existing particles by condensation of water vapor, and eventually their wet scavenging by cloud droplet activation. This can explain the lack of particle larger than 100 nm (a NMB of -6.26 for the Kulmala scheme, respectively -38.82 for the Vehkamaki scheme) and is sustained by the accumulated precipitation field predicted by the WRF model (see Fig. 4.33). Again, in the absence of a condensable sink represented by pre-existing accumulation mode particles, nucleation of new particles will be favored, especially using the Kulmala scheme. In the present case compared to the case of March 26th, modeled accumulation mode particles are more strongly depleted by cloud activation of cloud droplets and the scavenging by rain as can be seen in Fig. 4.34, enhancing the formation of ultrafine particles predicted by the Kulmala scheme to a non realistic level.

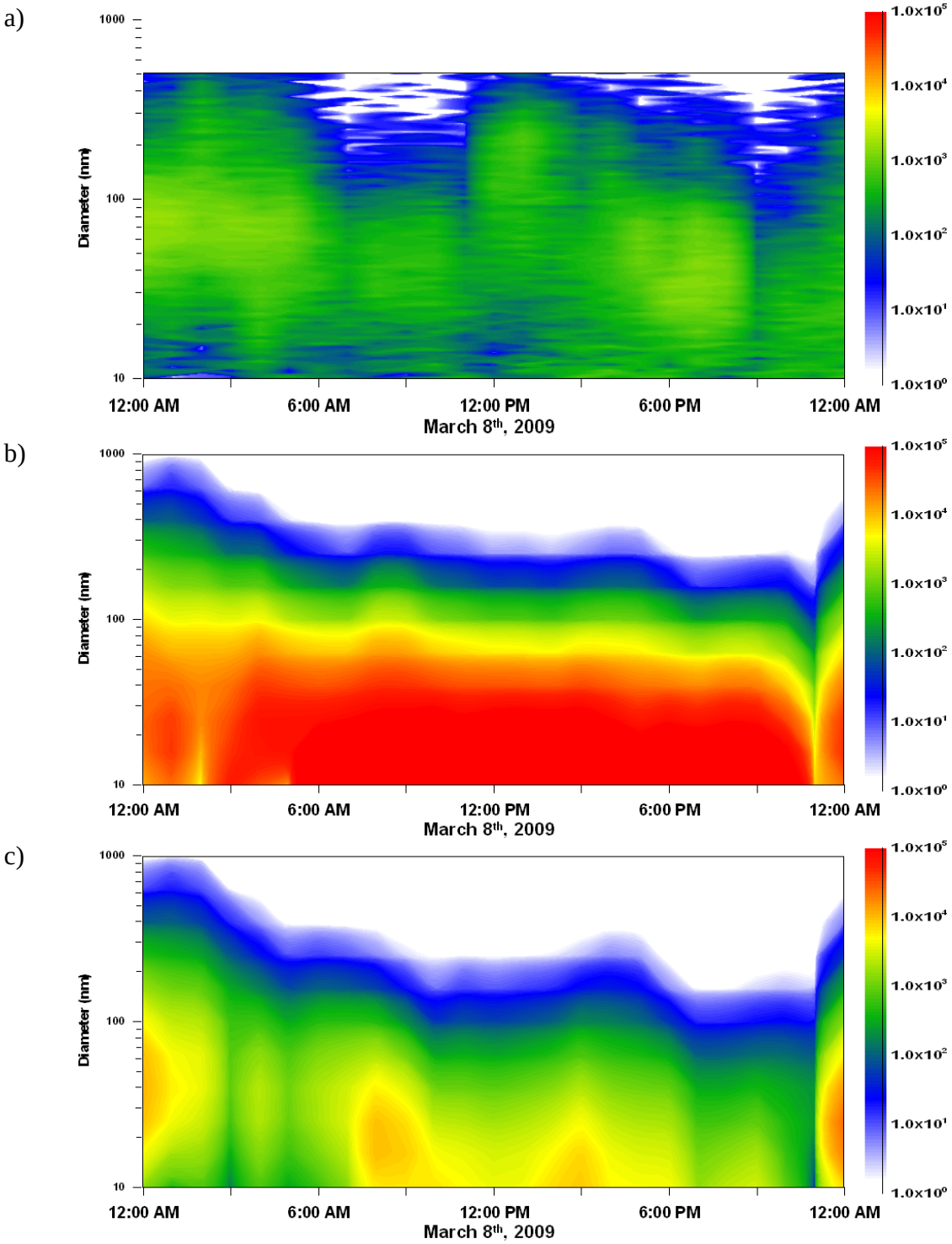

Figure 4.31. Hourly number size distribution: a) Observation; b) Kulmala scheme; c) Vehkamaki scheme.

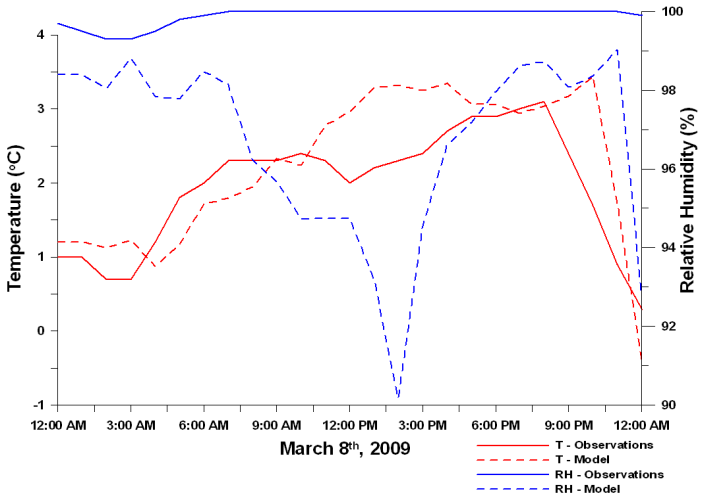

Figure 4.32. RH and T modeled and observed for 8 March 2009

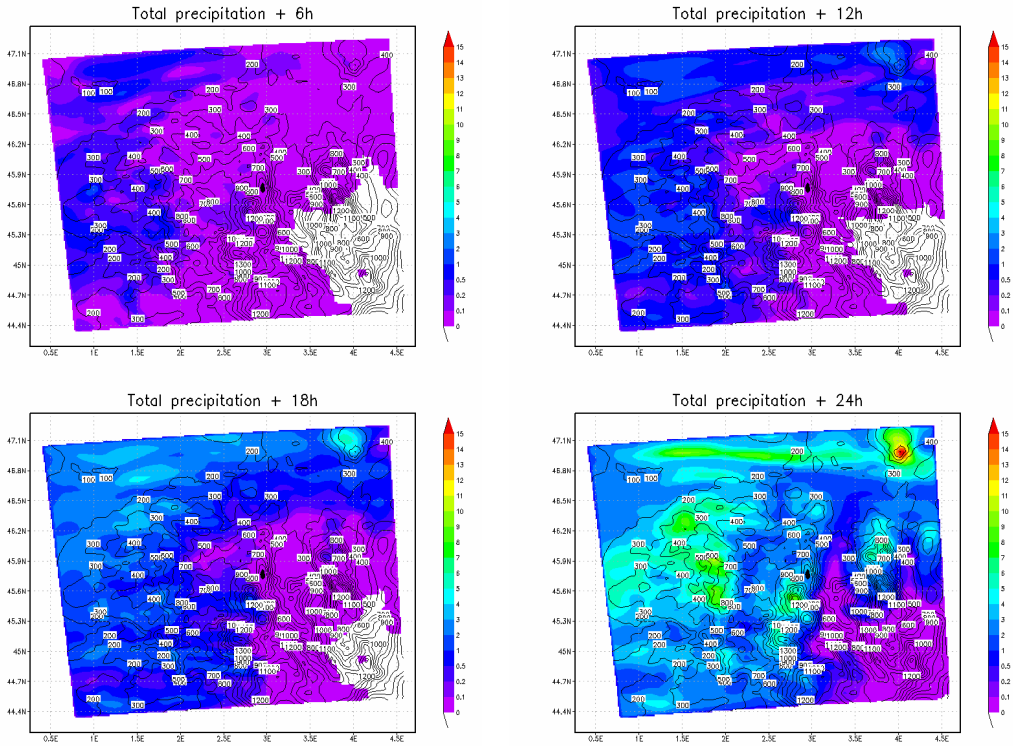

Figure 4.33. Total accumulated precipitations at every 6h for March 8th, 2009. The black point indicates the PDD location

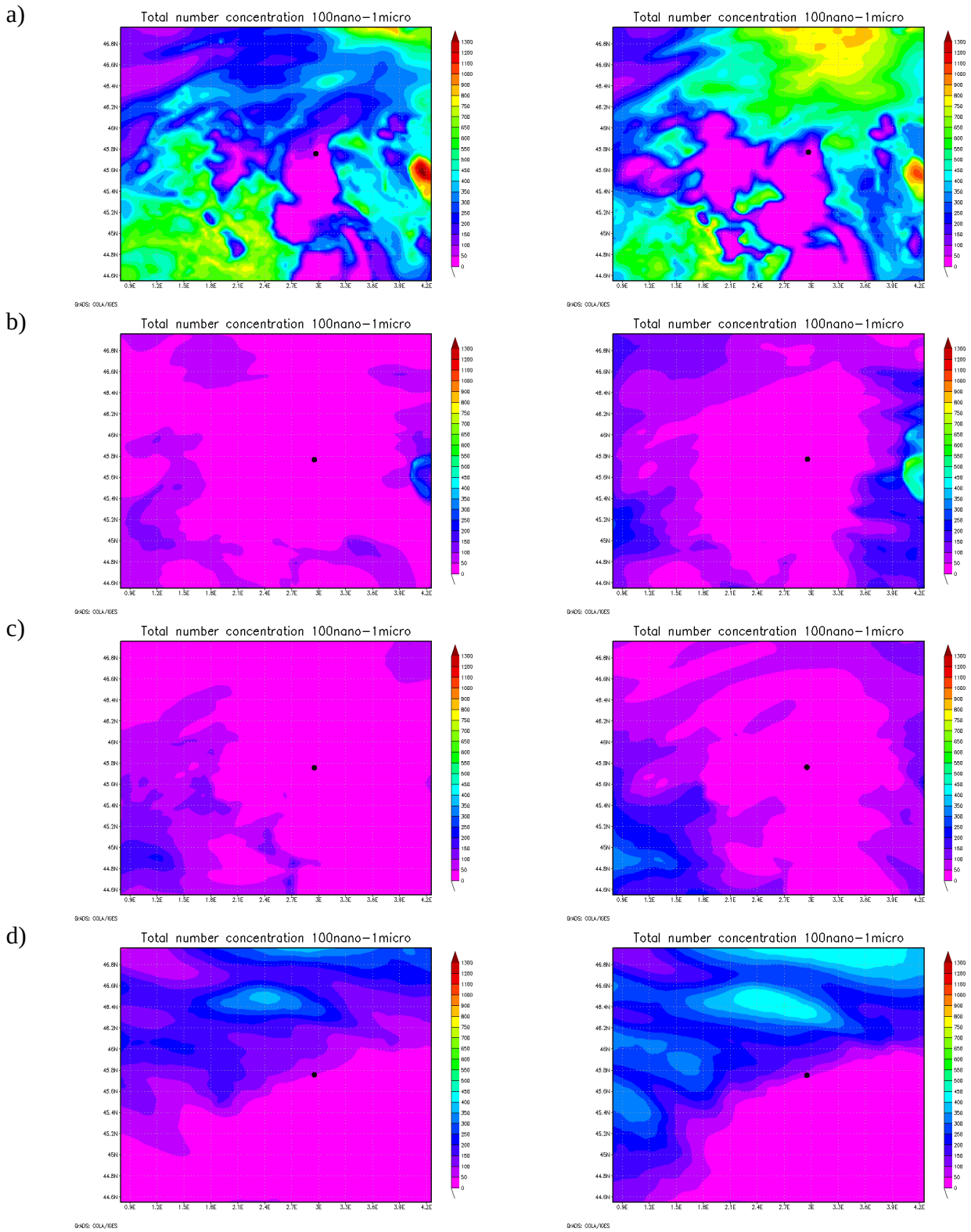

Figure 4.34. Total number concentration for particles having the diameter larger than 100nm for Kulmala scheme (left part) and Vehkamaki scheme (right part) at every 6 hours: a) 06 UTC; b) 12 UTC; c) 18 UTC; d) 24 UTC. The black point indicates the PDD location

4.3.4. Conclusion

We conclude that in general all nucleation schemes involved in the CHIMERE code are not able to correctly reproduce the observed particle number concentrations. On March 25th, 2011, however both schemes, Kulmala and Vehkamaki, are able to reproduce the nucleation events observed at the PDD site. The moment of the onset of nucleation slightly differs. The organics scheme does not capture the increase of particle number in the nucleation mode.
We notice that when the cloud and precipitation favor the removal of particles larger than 100 nm (case of observed nucleation on 7-8 April 2008, weak nucleation event on March 26th, 2011 and non-event on March 8th, 2009) the Kulmala scheme predicts an extremely high number of particles in the nucleation mode, but the Vehkamaki scheme matchs better the observation. For all analyzed cases using the organics scheme we can observe that this scheme is not able to reproduce neither the nucleation events observed on March 25th, 2011 and May 5th, 2011 nor the weak nucleation event observed on March 26th, 2011. The performance of the various parameterizations leads us to the conclusion that the parameterization of Vehkamaki is more suitable for modeling studies on aerosol nucleation in CHIMERE.

We have demonstrated that the lack of accumulation mode particles due to wet scavenging induce the nucleation of large numbers of nanoparticles in the model, especially when the default nucleation scheme (Kulmala's scheme) is used. The pre-existing accumulation mode particles represent a condensation sink which is an essential parameter for the occurrence of the nucleation processes. Hence, it is important that the model reproduces well the pre-existing aerosol size distribution. The size distribution of pre-existing particles is well simulated only if the size of primary particles emitted is right.
In the next section, we will investigate the effect of the choice of different primary particle sizes on the formation of new particles by nucleation.

4.4. The influence of primary emissions size

The aim of this section is to study the sensitivity of the size distribution of primary particles on the aerosol spectra simulated by CHIMERE. For the particle mass concentration a fixed log-normal size distribution is used with the median diameter D and the standard deviation, σ. The emission size distribution is important in the models because they affect the aerosol microphysical processes which are size-dependent.

4.4.1. The model set-up

The simulations made in the previous section 4.3 by means of the Vehkamaki scheme in now called the default set-up, which applied the following modal parameters for the primary aerosol mass distribution. Median diameter and standard deviation of the default case of the previous simulation of section 4.3 are given in Table 4.7.

Table 4.7. Modes of the primary particle mass distribution for the model set-up for the default experiment

Acronym	Median diameter (m)	Standard deviation
PPM_big	2.5e-6	1.3
PPM_coa	4e-6	1.1
PPM_fin	0.11e-6	1.6
OCAR_fin	0.11e-6	1.6
BCAR_fin	0.11e-6	1.6

The acronym PPM represents primary particulate matter, PPM_big refers to particles having the diameter larger than 10 μm, PPM_coa to PM10-PM2.5, PPM_fin to PM2.5, OCAR (primary organic carbon) and BCAR (primary black carbon) are assumed to be in the fine mode.

The following numerical experiment named 50nano has the same median diameter as for the default case, but the median diameter for fine particles is moved to 50 nm instead of 110 nm (see Table 4.8).

Table 4.8. Modes of the primary particle mass distribution for the model set-up for 50nano experiment

Acronym	Median diameter (m)	Standard deviation
PPM_big	2.5e-6	1.3
PPM_coa	4e-6	1.1
PPM_fin	0.05e-6	1.6
OCAR_fin	0.05e-6	1.6
BCAR_fin	0.05e-6	1.6

We will thus analyze the influence of median diameter for the results obtained using the Vehkamaki scheme for the default and 50nano experiments respectively.

4.4.2. Results and discussion

The same statistics applied in section 4.4 are used to asses the model performance for default and the 50nano experiments. In the following section all aerosol number distribution function presented give an average over 24 hours.

First we will analyzed the cases of March 25th, 2011, May 5th, 2011 and 7-8 April 2008, when the nucleation was observed at PDD summit, to see the impact of the different primary particles size on the formation of new particles.

4.4.2.1. March 25th, 2011 case

As can be seen in Table 4.9, for all particles size ranges, the default experiment underestimates the observation and this underestimation is most accentuated for particles larger than 100 nm. The 50nano experiment overestimates the observation for N_{tot} (NMB=96.42%) and the correlation factor is poor (R=0.05), while for N_{50} and N_{100} the NMB indicates an underestimation (NMB=-30.44% for N50, respectively NMB=-72.24% for N100), however, with a visible improvement of the correlation factor.

Table 4.9. Summary statistics for total particle number concentration (D_p>10nm; N_{tot}) and number concentration in two size ranges typical for CCN: D_p>50nm (N_{50}) and D_p> 100nm (N_{100}). The normalized mean bias (NMB) and correlation coefficient (R) are calculated between simulated and observed number concentration at PDD site on March 25th, 2011

Model		NMB (%)			R	
experiment	N_{tot}	N_{50}	N_{100}	N_{tot}	N_{50}	N_{100}
Default	-34.17	-28.43	-68.11	0.01	0.25	0.85
50nano	96.42	-30.44	-72.24	0.05	0.85	0.92

As can be seen in Fig. 4.35, the mean observed particles size distribution shape for nucleation mode particles is better reproduced by the 50nano experiment in comparison with the default experiment; however the total particle number overestimates the observations by a factor of 1.74 within the observations. Hence, also for this case study where nucleation and growth was relatively well predicted using the default primary particle size, using smaller primary particle sizes increases the adequacy between modeled and measured size distributions for all sizes (see Table 4.9).

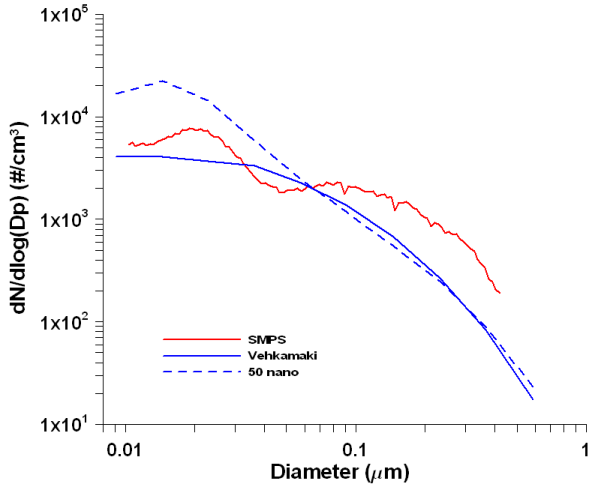

Figure 4.35. Mean simulated and observed total number size distribution for March 25th, 2011

4.4.2.2. May 5th, 2011 case

As can be seen in Table 4.10, comparatively with the default experiment for the N_{tot} the modeled outputs for the 50nano experiment overestimate the observations on May 5th. We can also detect that the prediction of the number concentrations of particles larger than 50 nm is improved in the 50nano experiment. However all the correlation factors are quite weak.

Table 4.10. Same as Table 4.9 on May 5th, 2011

Model experiment	NMB (%)			R		
	N_{tot}	N_{50}	N_{100}	N_{tot}	N_{50}	N_{100}
Default	-58.91	-63.46	-58.38	0.17	0.21	0.38
50nano	103.27	-39.13	-76.08	0.21	0.21	0.35

Figure 4.36 present the number size distribution at PDD for the two scenarios as well the observed one. The size of primary particles influences the concentration of the nucleation mode particles significantly. The general shape of the observed size distribution in the range 30-80 nm is better reproduced by the 50nano experiment. Comparatively with the default experiment, the 50nano experiment overpredicts the particles number in the nucleation mode, while for the accumulation mode all tests give an underestimation, which is also confirmed by the NMB values (see Table 4.10). However, changing the size of primary particles to smaller sizes promotes nucleation, which was not captured with the default model set up. We observe that a stronger particle nucleation is due to the change of the fine mode particles.

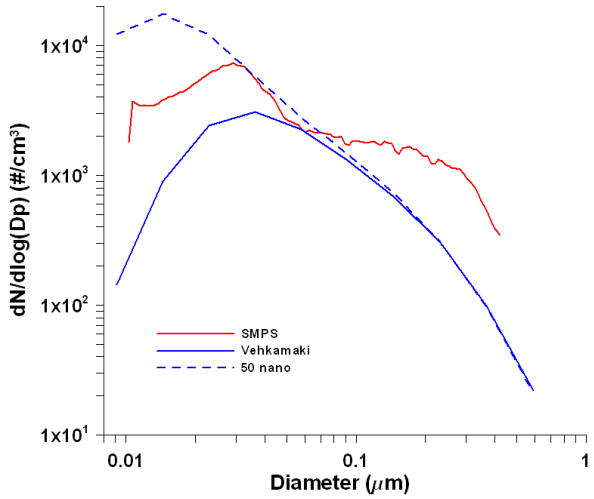

Figure 4.36. Same as Figure 4.32, but for May 5th, 2011

4.4.2.3. 7-8 April, 2008 case

As can be seen in Table 4.11, the modeled nucleation event increases the model bias for N_{tot}. The overprediction of N_{tot} is largely due to the overprediction of number concentrations of smaller particles. The 50nano experiment increases the NMB comparative with the default experiment,

but improves the correlation factor. The N_{50} for the default and 50nano experiments have similar NMB and R values. However, the increase of particles number in the nucleation and Aitken mode lead to a decrease of particles in the accumulation mode, confirmed by the NMB.

Table 4.11. Same as Table 4.9 on 7-8 April 2008

Model		NMB (%)			R	
experiment	Ntot	N50	N100	Ntot	N50	N100
Default	620.89	131.38	-66.61	-0.11	0.15	0.68
50nano	1388.25	124.58	-64.20	0.40	0.15	0.65

The mean observed and modeled size distribution (see Fig. 4.37) shows an increase of the particle number for the 50nano experiment comparative with the default case in the nucleation and the Aitken mode, but the strong lack in the accumulation mode particles remains as also shown in Fig. 4.34 and in the statistics of Table 4.11.

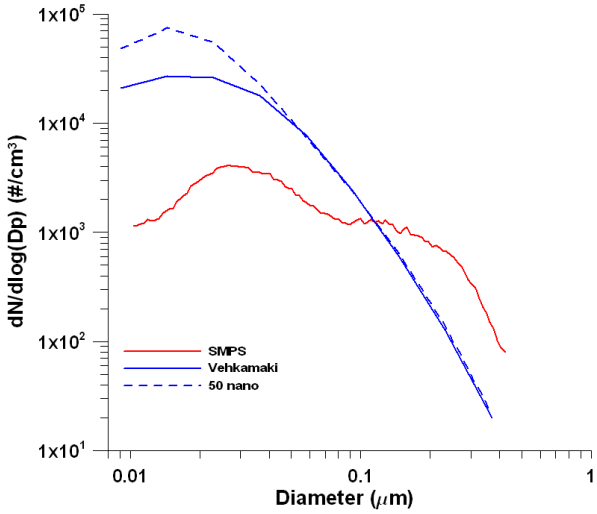

Figure 4.37. Same as Figure 4.32, but for 7-8 April 2008

Now the cases of March 26th, 2011 and February 25th, 2009 when weak nucleation events and the case od March 8th, 2009, with no nucleation at PDD summit will be analyzed in order to verify if a shift for the primary particle will improve the result obtained from the default configuration.

4.4.2.4. March 26th, 2011 case

As can be seen in Table 4.12 comparatively with the default experiment, the 50nano experiment leads to high overestimation of N_{tot}, while the correlation factor is reduced. For N_{50} all experiments have a negative NMB, more accentuated for the default and 50nano experiments, with a comparable correlation factors. For N_{100}, the NMB for all experiments had almost the same values, while the correlation factor is weak for all experiments.

Table 4.12. Same as Table 4.9 on March 26th, 2011

Model	NMB (%)			R		
experiment	N_{tot}	N_{50}	N_{100}	N_{tot}	N_{50}	N_{100}
Default	-37.70	-56.89	-81.66	0.30	0.28	0.12
50nano	80.31	-60.86	-86.59	0.25	0.25	0.28

As can be seen in Fig. 4.38, by reducing the emissions size of the primary particles, the particle number concentrations in the nucleation and the Aitken mode is increased comparatively with the default experiment. For all experiments, the observed number concentration of the particles in the accumulation mode is greater than the modeled one.

Again, as in the case of the 5th of May, the model is wrongly overpredicting nucleation when the size of primary particles in the fine mode was decreased to 50 nm, while is it underpredicting nucleation when the default size of 110 nm is used. Hence, an intermediate size of 75 nm may ameliorate the quality of the prediction of nucleation.

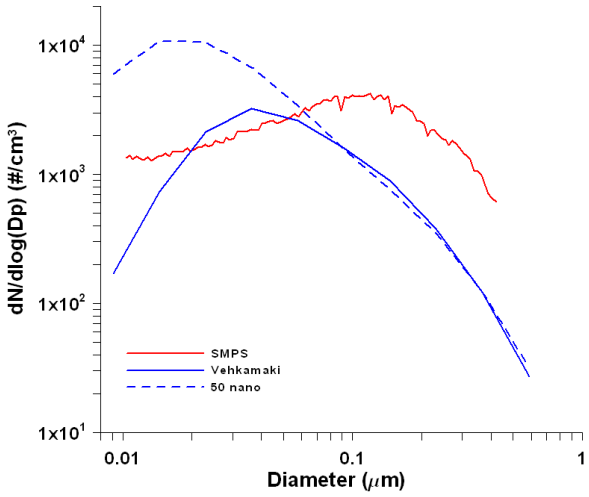

Figure 4.38. Same as Figure 4.32, but for March 26th, 2011

4.4.2.5. February 25th, 2009 case

Comparatively with the default experiment, the 50nano experiment leads to high NMB for the N_{tot} (971.67 %) and N_{50} (301.87 %) (see Table 4.13). However, for the N_{100} the underprediction of the default experiment (NMB=-76.06 %) is reduced for 50nano experiment (NMB=-23.13%). The correlation factor is weak for all tests in all size ranges.

Table 4.13. Same as Table 4.9 on February 25th, 2009

Model		NMB (%)			R	
experiment	Ntot	N50	N100	Ntot	N50	N100
Default	314.71	34.39	-76.06	-0.05	0.14	0.01
50nano	971.67	301.87	-23.13	0.21	0.17	0.12

As can be seen in Fig. 4.39, the 50nano experiment accentuates the increase of the mean modeled particle size distribution in comparison with the default experiment in the 10-70 nm size range, but with the same shape for the particles higher than 70 nm for both experiments.

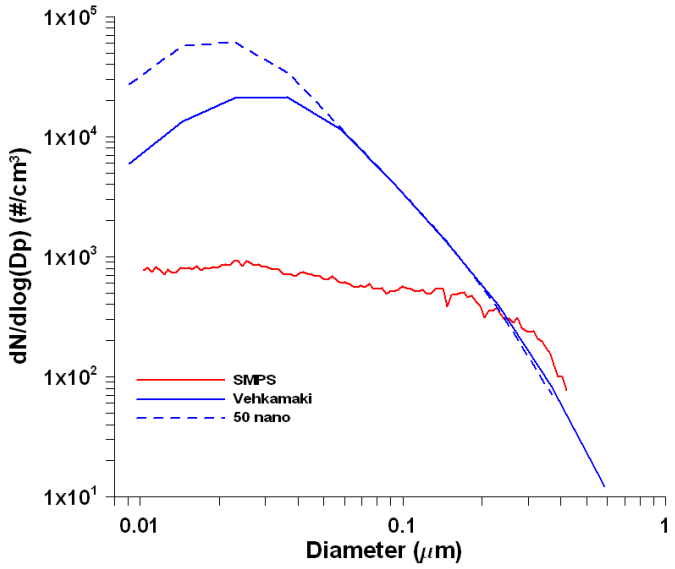

Figure 4.39. Same as Figure 4.32, but for February 25th, 2009

4.4.2.6. March 8th, 2009 case

On March 8th, 2009 nucleation was not observed at PDD summit, and the sensitivity tests made (see section 4.3.3.1) have shown that also the Vehkamaki scheme did not predict nucleation for that day. Furthermore, the impact of the primary particle size distribution will be analyzed in order to see if this improves the particle forecast.

The 50nano experiment leads to an overestimation of N_{tot} with a NMB of 683.58 % (see Table 4.14), and a poor correlation factor. The NMB for N_{50} are comparable for both experiments, and all shown a good correlation. The increase of particles number concentration in the nucleation mode leads to a decrease of particles in the accumulation mode, confirmed by the NMB (-38.82 % for the default experiment and -52.80 % for the 50nano experiment).

Table 4.14. Same as Table 4.9 on March 8th, 2009

Model		NMB (%)			R	
experiment	Ntot	N50	N100	Ntot	N50	N100
Default	448.90	76.92	-38.82	-0.04	0.62	0.51
50nano	683.58	71.95	-52.80	-0.02	0.66	0.53

Figure 4.40 presents the mean modeled and observed particles size number distribution. As it can be seen, the mean modeled particle size number distribution show a large overestimation for particles in the size range from 10 nm to 50 nm, by a factor of 10.06 for the default experiment and by a factor of 13.29 for the 50nano experiment, correlated with an underprediction for the particles higher than 100 nm diameter (by a factor of 1.81 for the default experiment and by a factor of 2.11 for the 50nano experiment).

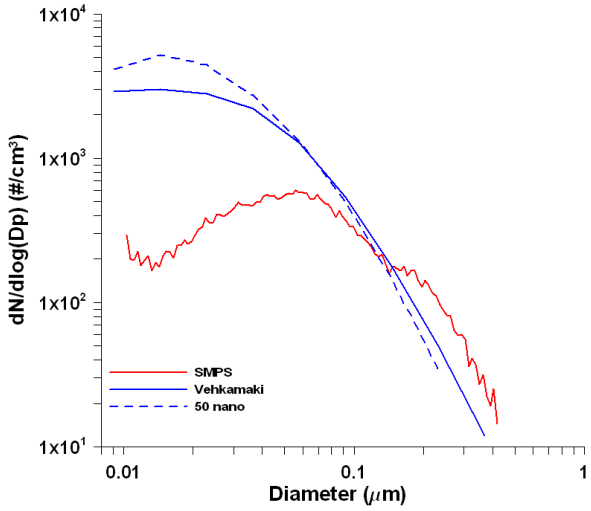

Figure 4.40. Same as Figure 4.32, but for March 8th, 2009

4.4.3. Conclusion

When the NMB for Ntot, N50 and N100 is negative (as for March 25th, 2011 and May 5th, 2011) we noticed that 50nano test scenario gives an improvement of the forecast in comparison with the default test. Other sensitivity tests for the values of the PPM_fin parameter are required for an intermediate value between 50 nm and 110 nm. For the cases when nucleation is overestimated due to a lack of particles in the accumulation which are scavenged by rain, the change in preexisting particle size does not improve the forecast as expected; on the contrary the number of particle in the nucleation mode is increased.

4.5. The changes in the aerosol chemical composition due to the nucleation scheme

A surprising result registered due to the change of the nucleation scheme was the change in the resulting change in the chemical composition of aerosols. We applied for the aerosol chemical species measured during the intensive campaign driven from February 24 to March 8, 2009 at

PDD site the same statistics as previously used in the Chapter 3, using the Kulmala and the Vehkamaki scheme. The statistical error analysis shown in Table 4.15 indicates a significantly changes in the mass of SO_4, NO_3 and NH_4 compounds when the default nucleation scheme is changed to Vehkamaki scheme.

Table 4.15. Statistics for aerosol chemical composition at PDD site for 24 February – 8 March 2009 period

Parameter/Emissions database	*BIAS (μg/cm^3)		**RMSE (μg/cm^3)		***NMB(%)	
	Kulmala	Vehkamaki	Kulmala	Vehkamaki	Kulmala	Vehkamaki
SO_4	0.48	-0.10	1.08	0.65	38.70	-8.18
NO_3	1.42	2.77	1.51	2.77	131.59	256.03
NH_4	0.11	0.34	0.50	0.65	9.50	27.76
OC	-1.16	-1.16	1.28	1.28	-68.20	-68.20

Graphical comparisons between the measured and predicted SO_4, NO_3, NH_4 and OC daily variation of the hourly median concentrations are shown in Fig. 4.41. The model overestimates the SO_4 concentrations when Kulmala scheme is used within a factor of 1.38, while the use of the Vehkamaki scheme leads to an underestimation within a factor of 1.08 (Fig. 4.41a). The diurnal variation of the median sulfate concentration matches better the diurnal variation of the measurements when the Vehkamaki scheme is used. The variability of the sulfate concentration are much higher when the Kulmala scheme is used, most probably due to the high overprediction of nucleation mode particles when low pressure conditions are encountered as described in the previous section.

As shown (Fig. 4.41 b),c), the NH_4 and NO_3 concentrations are both overestimated using the two nucleation schemes. The NO_3 concentrations give a substantial bias in both simulations, leading to overestimations within a factor of 2.31 for the Kulmala scheme and 3.56 for the Vehkamaki scheme. We have little explanations for this large discrepancy between the simulations when the two nucleation schemes are used, since their formulations involve only sulfuric acid. A different consumption of the oxidants such as OH radical in the model would certainly modify the nitrogen cycle though.

The model overestimates the NH_4 by a factor of 1.27 for the Vehkamaki scheme, and this overestimation is reduced to a factor of 1.09 within the observations for the Kulmala scheme.

The differences in the NH_4 mass can be linked to the H_2SO_4 and HNO_3 concentrations. H_2SO_4 and HNO_3, the major acidic gases in the atmosphere, come from oxidation of sulfur dioxide

(SO_2) to H_2SO_4 and oxides of nitrogen (NO_x) to HNO_3, respectively. These acid gases are neutralized in the atmosphere by ammonia (NH_3), the principal gaseous alkaline species. Further, through gas-to-particle conversion processes, the acid gases and NH_3 are involved in fine particulate matter formation (PM2.5) (Meng et al., 1997, Baek et al., 2004). Gas-to-particle conversion can be accomplished by condensation, which adds mass onto pre-existing aerosols, or by direct nucleation from gaseous precursors, forming an aerosol. Gas-to-particle conversion strongly depends on the concentration of acid gases and water vapor in the atmosphere (Stelson and Seinfeld, 1982, Seinfeld and Pandis, 1998). NH_3 reacts with H_2SO_4, and HNO_3 gases to form aerosols such as ammonium sulfate ($(NH_4)_2SO_4$), ammonium bisulfate (NH_4HSO_4), and ammonium nitrate (NH_4NO_3). Ammonium (NH_4) salts formed by these reactions can exist as solid particles or liquid droplets depending on the amount of water vapor in the atmosphere. NH_3 preferentially reacts with H_2SO_4 to form NH_4HSO_4 and $(NH_4)_2SO_4$ through equations (4.11) and (4.12).

$$NH_3(g)+H_2SO_4(l)\rightarrow NH_4HSO_4(l) \quad (4.11)$$

$$NH_3(g)+NH_4HSO_4(aq)\rightarrow (NH_4)_2SO_4(s)or(l) \quad (4.12)$$

NH_3 also can undergo an equilibrium reaction with gas-phase HNO_3 in the atmosphere to form NH_4NO_3 as shown in equation (4.13).

$$NH_3(g)+HNO_3(g)\rightarrow NH_4NO_3(s)or(l) \quad (4.13)$$

The primary source of atmospheric NH_4 is the gas to-particle conversion processes of gaseous NH_3, neutralizing the acid gases (H_2SO_4, HNO_3) produced by the oxidation of SO_2 and NO_2, respectively. The diurnal variation of NH_4 concentrations depends largely on the concentration trends of H_2SO_4 and HNO_3. Thus, the overprediction is related to the differences in H_2SO_4 concentrations due to different treatment of H_2SO_4 involved in these two parameterizations. An important portion of NO_3 can reasonably attributed to NH_4NO_3 presence. The main mechanism of secondary production of SO_4 and NO_3 includes ammonium according to Seinfeld and Pandis (1998).

However, the change of the nucleation scheme does not affect the behavior of the OC (see Fig. 4.41d), for both simulations the OC is underestimated within a factor of 3.14. This would indicate that the nucleation scheme did not affect the oxidant balance, but this hypothesis needs to be confirmed.

Thus we can conclude that CHIMERE-Kulmala leads to better results for NO_3 and NH_4 concentrations, while CHIMERE-Vehkamaki increases the adequacy between observations and model results for SO_4 concentrations. The change of the parameterization scheme does not impact on OC concentrations.

Zhang et al. (2010) advised to take extra cautions in selecting a nucleation parameterization since most parameterization have not been tested for all ranges of ambient conditions and the appropriateness of one parameterization cannot be determined solely based on whether it gives a good agreement with observations. We show that the nucleation scheme is not only influencing the number size distribution, but also the mass concentration and balance of main inorganic compounds in the aerosol, and hence we confirm this advice of caution.

.

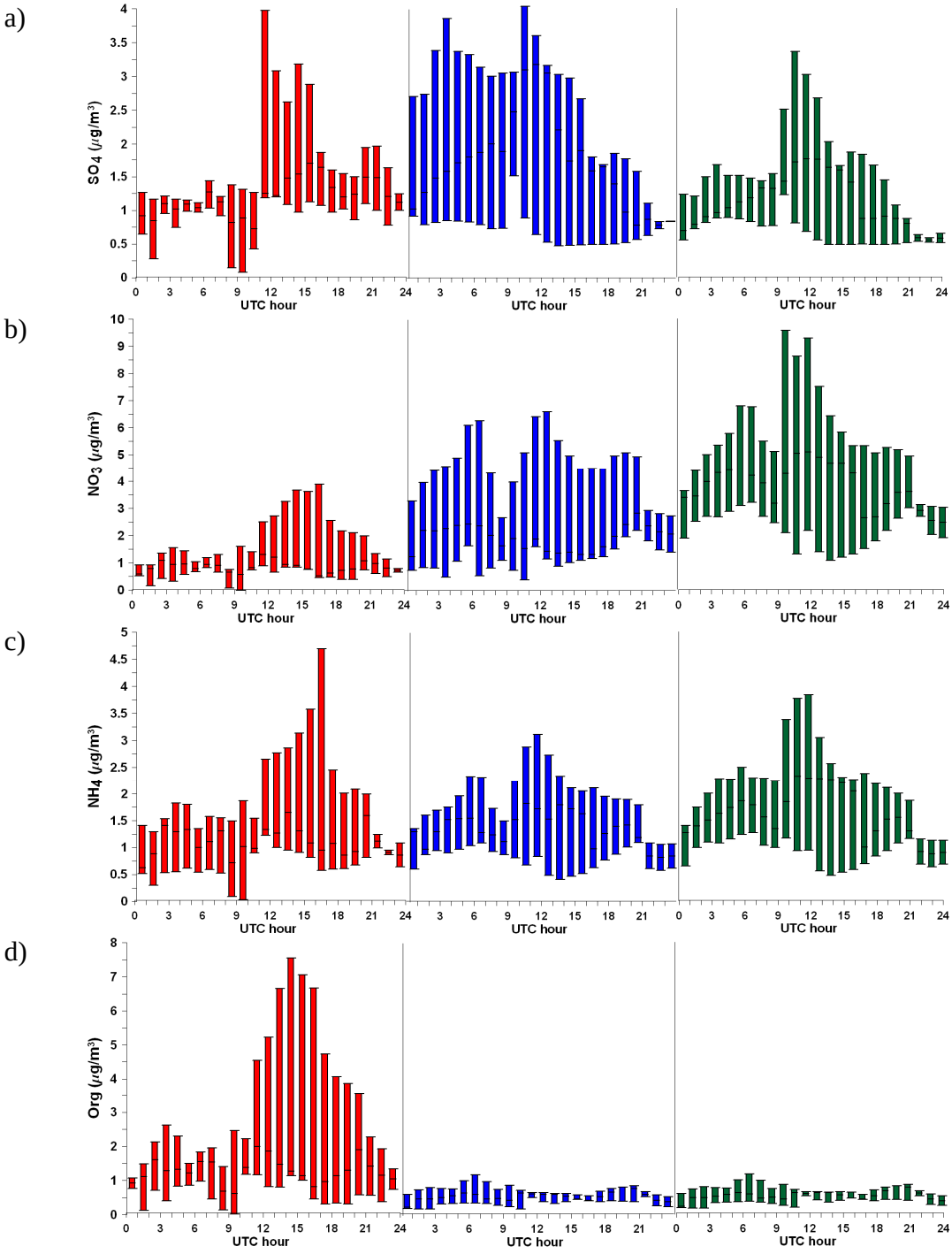

Figure 4.41. Hourly boxplot for SO_4 (a), NO_3 (b), NH_4 (c), and OC (d) for PDD site for the observation (red line) together with calculated values by CHIMERE-Kulmala (blue line) and CHIMERE-Vehkamaki (green line). The line in the middle of the box is the median, while the boxes represent the upper and lower quartile and the "whiskers" represent the 25th and 75th percentile for 24 February – 8 March 2009 period.

4.6. Is nucleation promoted at high altitude and/or promoted by force convection?

The free troposphere and lower stratosphere is a source region for new particle formation (Young et al., 2007, Merikanto et al., 2009). In particular, new particle formation events were associated with vertical motion that may also have brought higher concentrations of water vapor and aerosol precursors (that originate at the ground level) from lower altitudes to higher altitudes where temperatures and surface areas of aerosol particles are lower.

The mixing of the boundary layer air with the free troposphere has been proposed as an efficient mechanism for particle production (Fukuta and Wagner, 1992 and Kulmala and Wagner, 1996). This is caused both by dilution of boundary layer air with clean tropospheric air and by the increased photochemical activity at the boundary layer/freetroposphere interface (Kulmala et al., 2004 and Nilsson et al., 2001). The nucleation of new aerosol particles seems to be controlled by the initial condition and the competition between condensation and coagulation processes (Kulmala, 2003).

In order to investigate the impact of the topographical features in the nucleation process for the May 5th, 2011 case we made a sensitivity test without taking in account the terrain height. For this purpose the static geographical data sets necessary for the WRF model that are interpolated by the geogrid program were defined as being equal to 0. In this case we don't have the air motions over the complex topography associated with the PDD site where strong vertical flows may occur. The nucleation scheme used for this test is the Vehkamaki scheme. In the following this sensitivity test will be named TOPO0.

The comportment of the Vehkamaki scheme in comparison with the observations made at PDD was analyzed in the section 4.4.1.

Figure 4.42 presents again the hourly modeled and observed particles number size distribution at PDD for the default case.

On May 5th, 2011, nucleation and new particle formation was observed at PDD summit (Fig. 4.42a). Using the Vehkamaki scheme in the CHIMERE model, we observe that the model fails to reproduce the occurrence of the event (Fig. 4.42b).

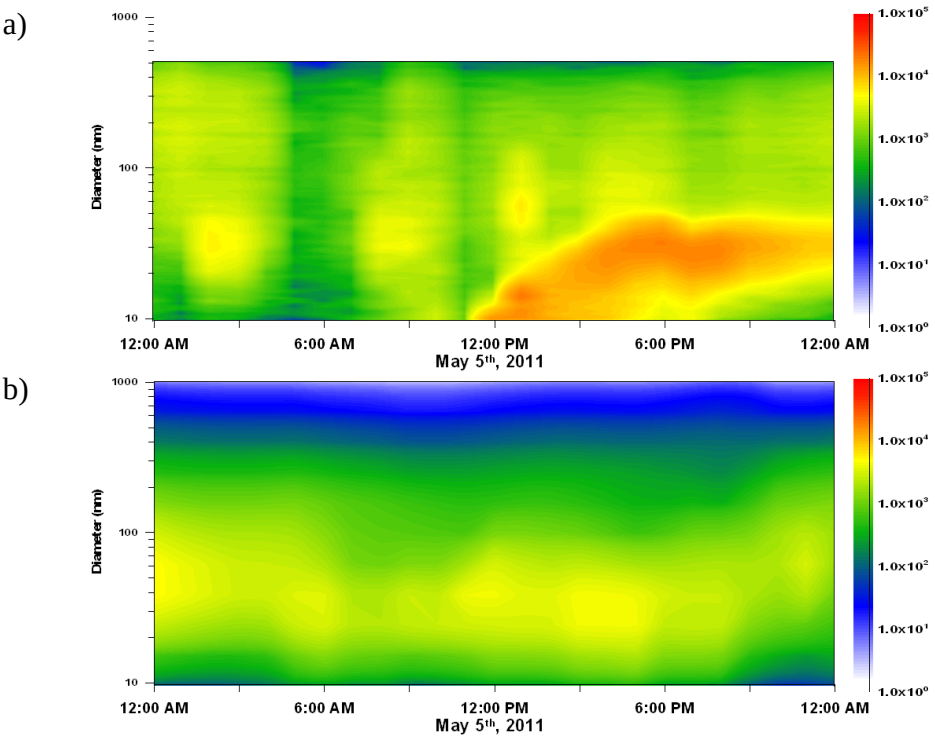

Figure 4.42. Hourly number size distribution for the default case: a) Observation; b) Vehkamaki scheme.

For the TOPO0 experiment we will analyze the hourly particle number distribution for each model level at the x-y location of the PDD.

The hourly particle number size distribution for the level 1 (approximately 40m above sea level), level 2 (approximately 100 m asl) and level 3 (approximately 220 m asl) have almost the same structure as can be seen in Fig. 4.43.

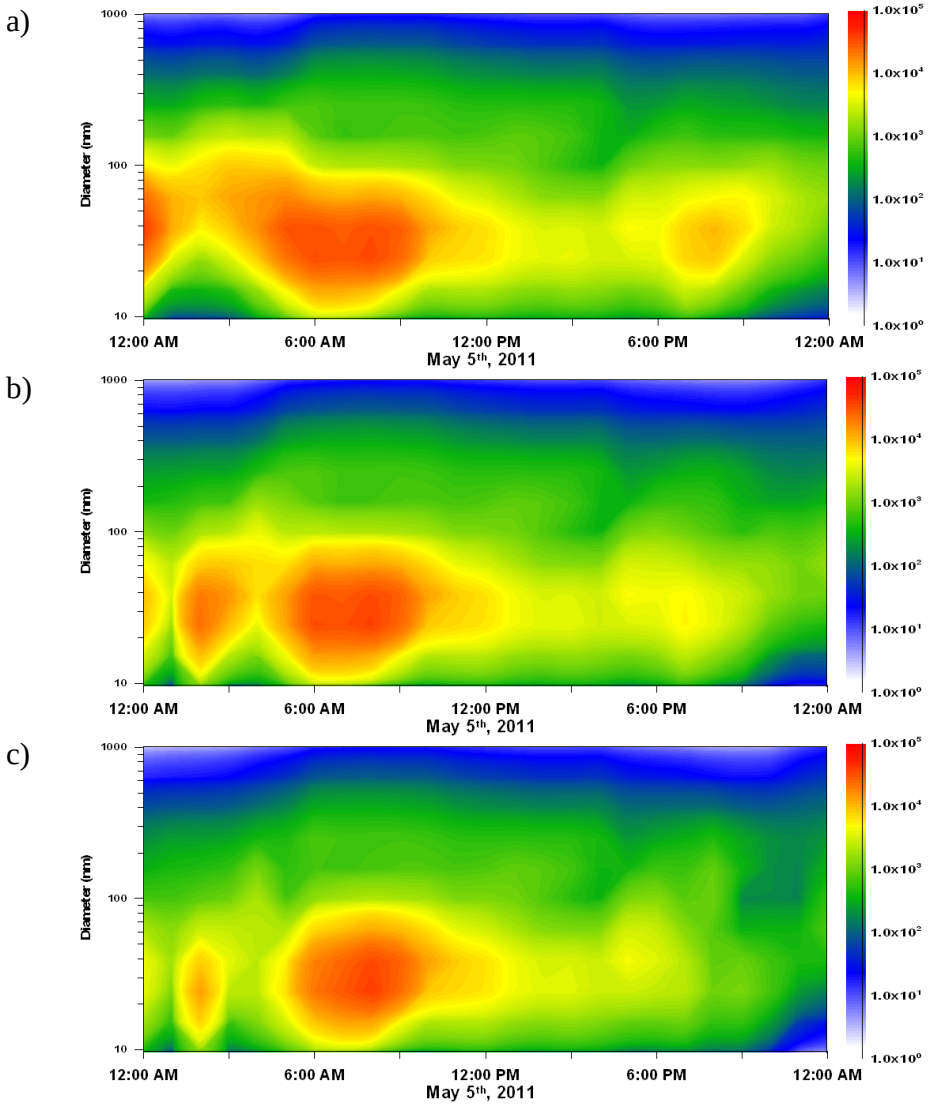

Figure 4.43. Hourly modeled number size distribution without topography at a) ~40 m asl; b) 100 m asl; c) 220 m asl.

A high number of particles are modeled in the first part of day in the Aitken mode, and a second peak of the Aitken mode particles is appearing in the evening. Both peaks are attenuated when going from 40m to 220 m a.s.l. This affirmation is sustained by the mean particle number size distribution for the first three model layers (see Fig. 4.44). This indicates that the sources of these particles are likely ground sources.

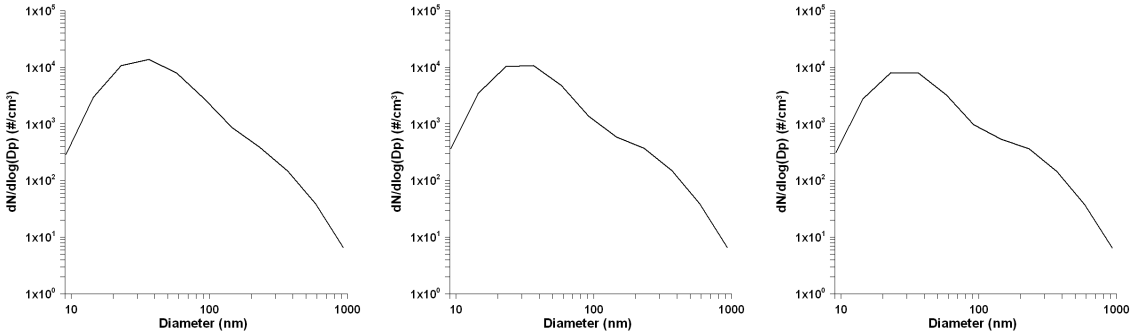

Figure 4.44. Mean particle size distribution at level 1 (left part), level 2 (center) and level 3 (right part).

We can assume that the high number of Aitken mode particles can be due to horizontal transport from long distance. In order to prove this affirmation we will present the map of the Aitken mode particles and will compute using the WRF meteorological model for the inner-most domain the backward trajectory. Figure 4.45 shows the number concentration for particles in the accumulation mode for the third vertical model layer. We can observe on the map the increase in total number concentration at PDD location before noon as the north-eastern wind brings more particles in the Aitken mode.

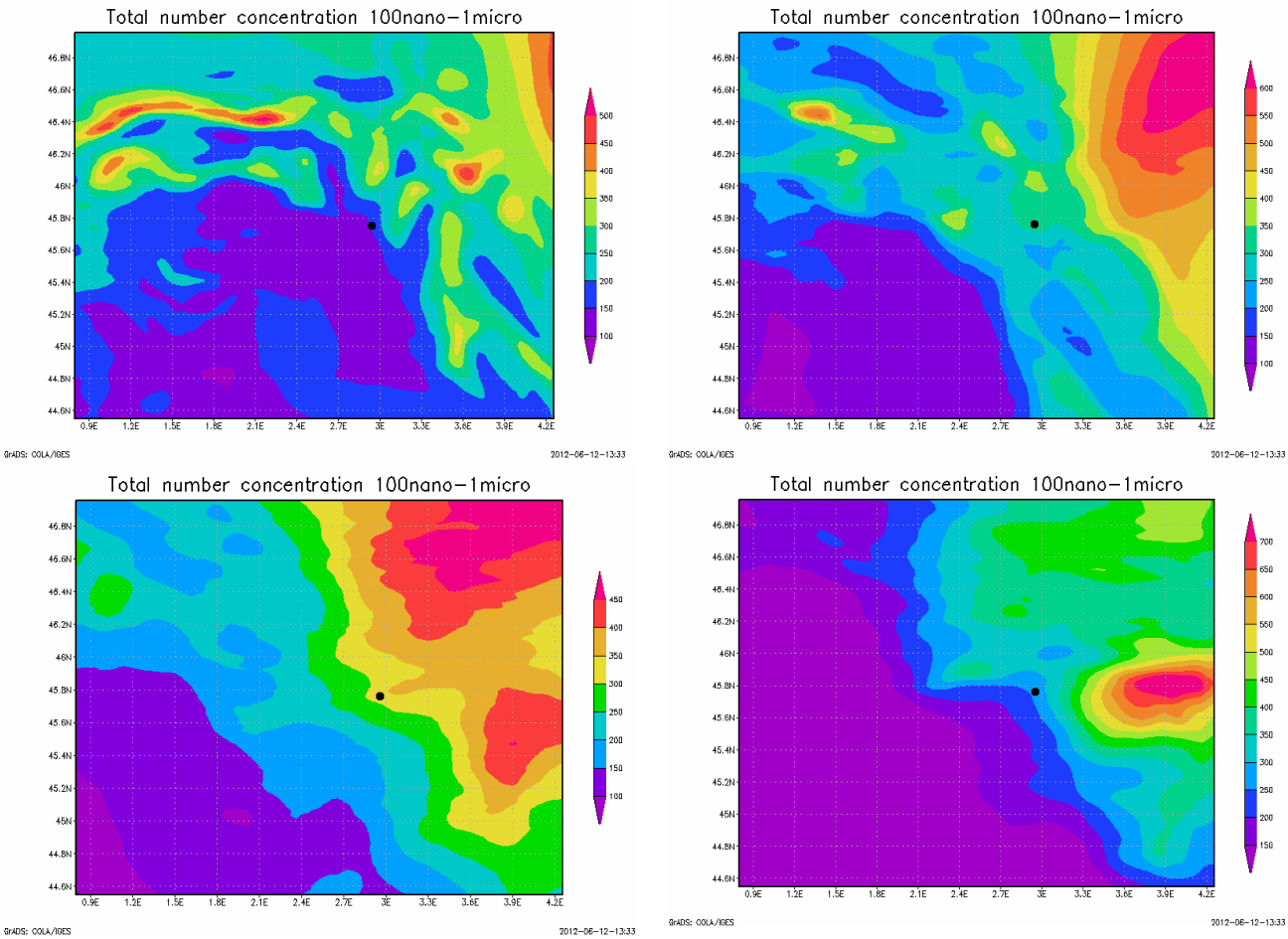

Figure 4.45. Total number concentration for particles in the accumulation mode) at every 3h: 03 UTC (upper left panel); 06 UTC (upper right panel); 09 UTC (lower left panel) and 12 UTC (lower right panel) for the third vertical model layer. The black point indicates the PDD location.

Figure 4.46 shows the backward trajectory calculated for PDD arriving at 07:00 UTC at 250 m asl. This was performed in order to observe the direction and altitude of the air mass prior to the moment when high particles concentrations are modeled for the lowest model layers. The modeled air mass was originated from a remote region, north-east of the PDD. The decrease of the total PNC at 06 UTC (see Fig. 4.46) can be associated with the break-up of the inversion in the entire mixing layer of the PBL. After the break-up we can see the increase of number concentrations (see Fig. 4.47).

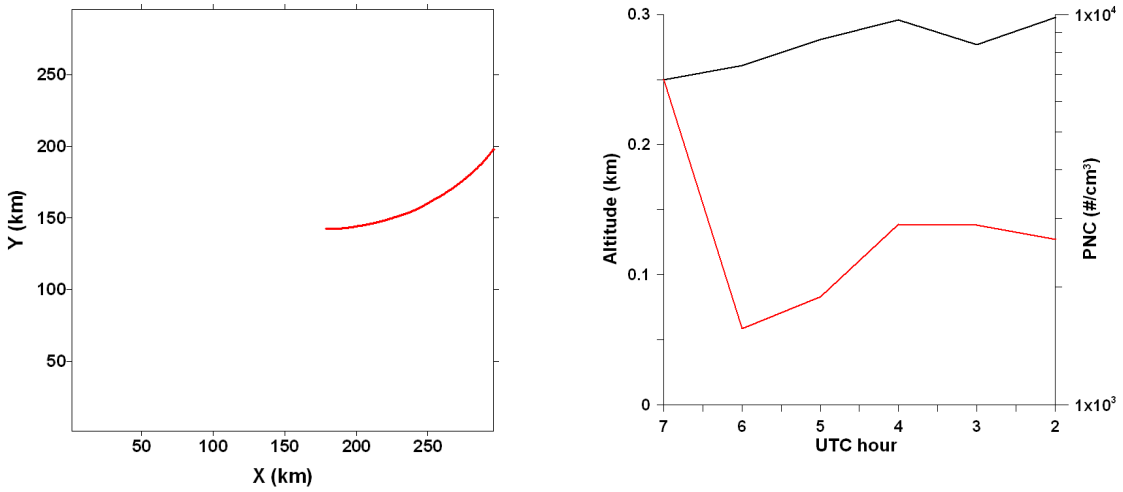

Figure 4.46. Backward trajectory ending at 07 UTC (left part) and altitude of the air mass together with total particle number concentration (right part; black line represents the mass altitude and the red line represents the total particle number concentration)

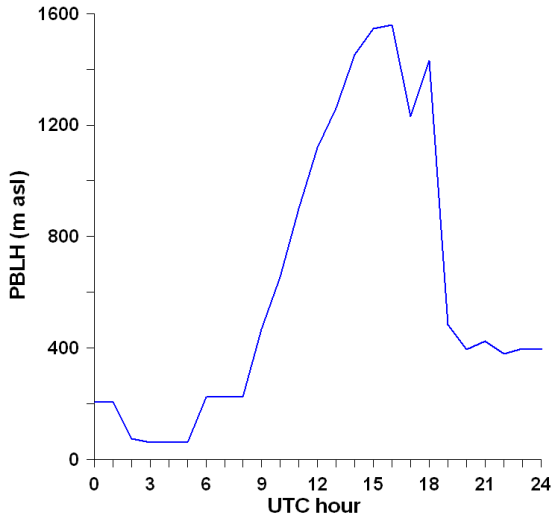

Figure 4.47. PBL height modeled by the WRF model

The increase of the PBL height and the mixing with free tropospheric air is associated with the high number of particles observed at 09 UTC at fourth level of the model (~430 m asl) and at 11 UTC at fifth level of the model (~800 m asl) (see Fig. 4.48).

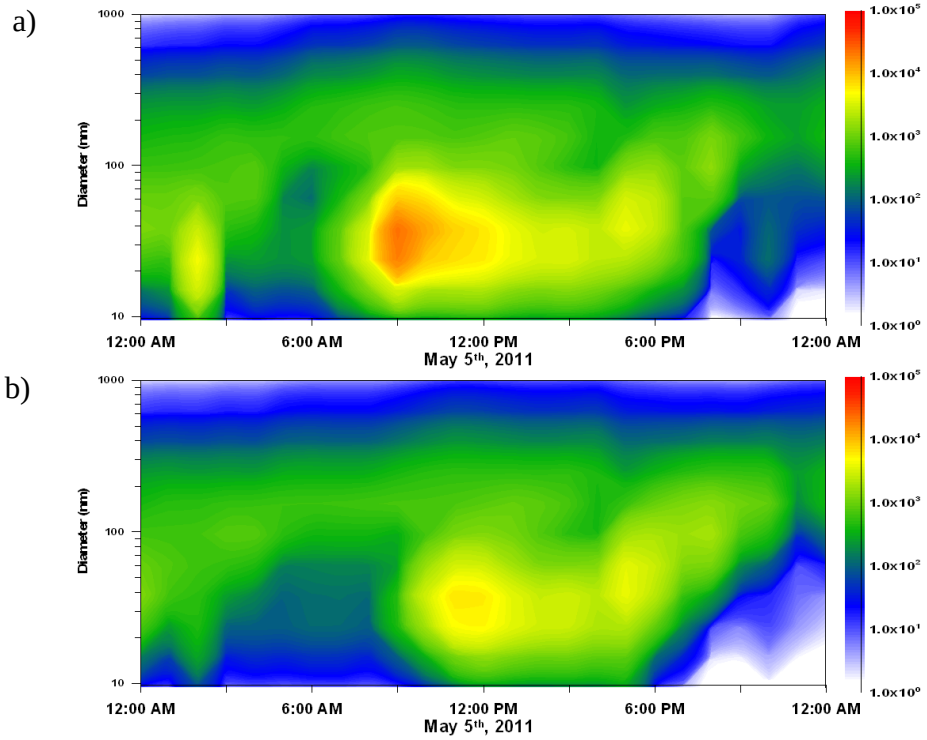

Figure 4.48. Hourly modeled number size distribution at a) ~430 m asl; b) ~800 m asl

When plotting the diurnal variation of the size distribution modeled at higher altitude (Fig. 4.46), we can suggest that some Aitken mode particles are transported by convection around noon at 1400 m a.s.l. (6^{th} model layer), but also the concentration of nucleation mode particles is increased during the afternoon. The increase of nucleation mode particles is even clearer at higher altitudes (7^{th} model layer ~2700m asl) (see Fig. 4.49). Hence, this would indicate that the injection of planetary boundary layer air into the free troposphere during sunny afternoons due to thermal convection is leading to nucleation.

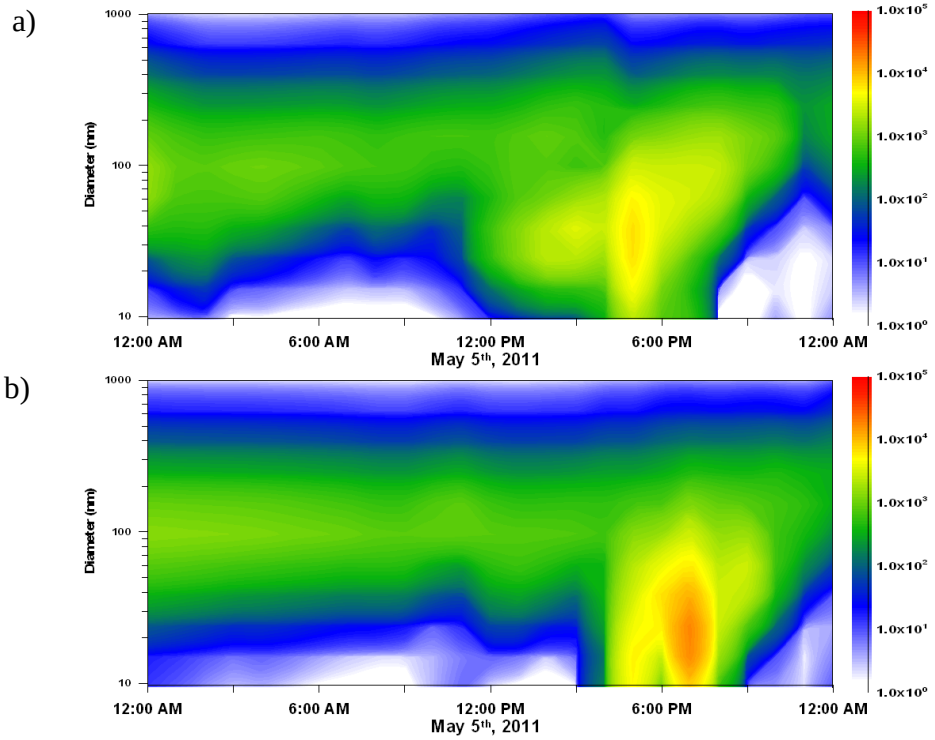

Figure 4.49. Hourly modeled number size distribution at a) ~1400 m asl 6; b) ~2700 m asl.

Thus, the modeled results are in agreement with the observations made in the free troposphere demonstrating that new particle formation can occur at high altitude (e.g. de Reus et al., 1999; Twohy et al., 2002; Benson et al., 2008).

However, when the level 6 (1400 m a.s.l.) is compared to measurements, we observe that nucleation is modeled several hours after it is observed at the Puy de Dome.

A comparison at the same model level between the modeled size distribution when the topography is take into account (Fig 4.42b) and without topography (Fig. 4.43a) and between number concentration for particles in the Aitken mode (Fig. 4.50) shows that the mountain range acts as a barrier to the transport of polluted air and the strong particle number concentration gradient is caused by topography that limits the transport.

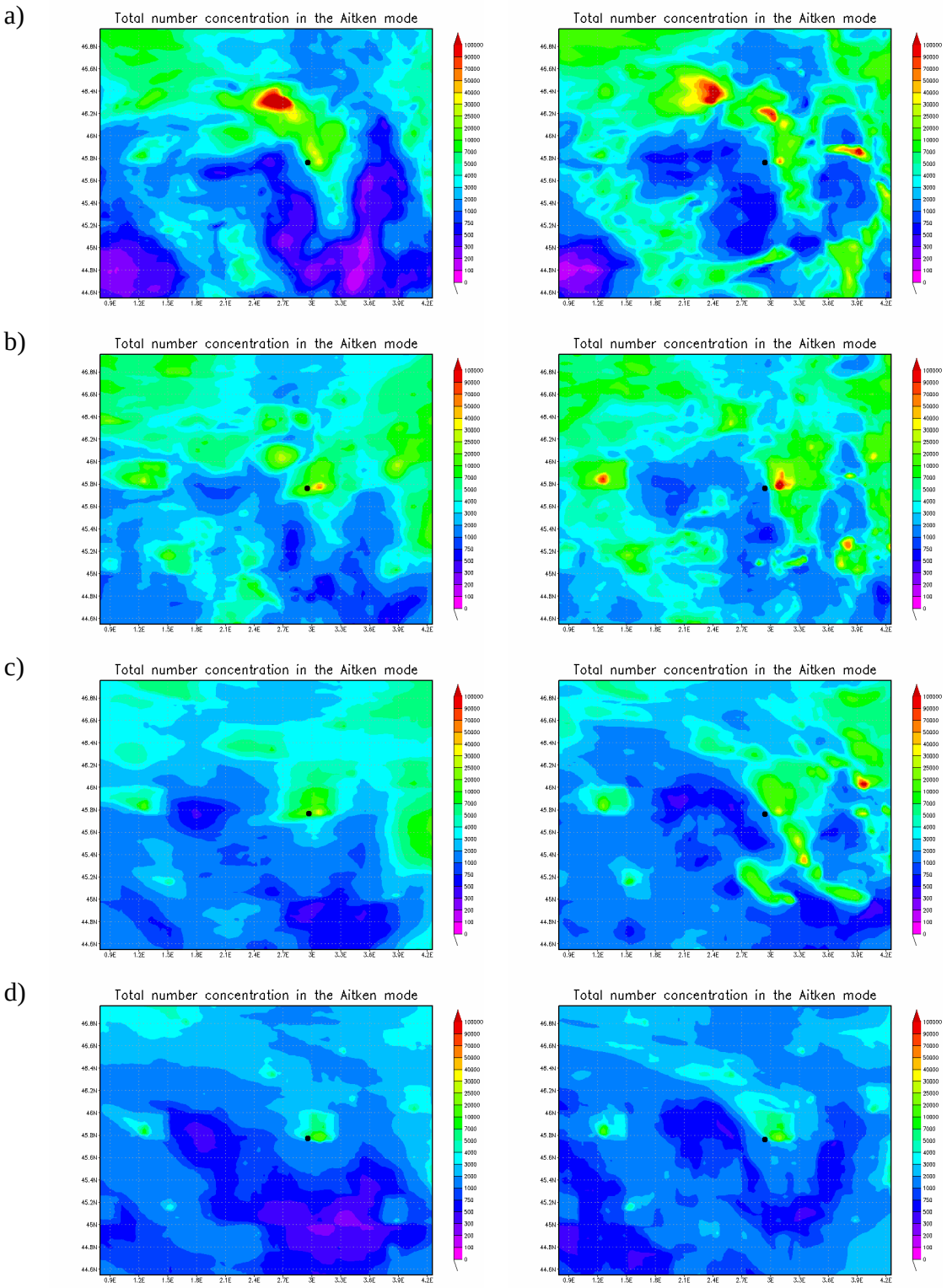

Figure 4.50. Total number concentration for particles in the Aitken mode at a) 03 UTC; b) 06 UTC; c) 09 UTC and d) 12 UTC for without topography case (left part) and with topography case (right part). The black point indicates the PDD location.

4.7. Conclusion

In this chapter we have analyzed the formation of new particles at a high altitude station modeled using three different nucleation schemes. When the synoptic situation is influenced by a high pressure system, and no rain occurs, we noticed that the modeled results are in agreement with the observations (March 25th, 2011, March 26th, 2011, May 5th, 2011 and February 25th, 2009). However, when the pressure is low, clouds and rain can favor the removal of particles larger than 100 nm from the atmosphere mainly by precipitation scavenging. The model is overestimating the concentration of nucleation particles, especially using the Kulmala scheme. The amount of accumulation mode particles simulated by the model is always smaller than the observed numbers. The absence of a condensable sink represented by the preexisting accumulation mode particles favors the nucleation. Overall, we found that the Vekhamaki scheme gives a better agreement between modeled and measured aerosol size distributions. The size of the primary particles directly emitted is influencing nucleation in the model. When conditions are anticyclonic and rain did not wash out the atmosphere prior to the day of study, decreasing the size of primary submicron particles from to 110 nm to 50 nm increases the adequacy between model predictions and measurements. However, when the nucleation is already overestimated due to the high relative humidity during rainy conditions, the decrease of the primary particle size leads to an increase of the particle number in the nucleation mode, hence giving a larger discrepancy between model and measurements.

We also evaluated the impact of Kulmala versus Vehkamaki schemes on aerosol concentrations and total particle number concentrations for the period February 24th – March 8th, 2009. Statistical validation shows that CHIMERE-Kulmala leads to better results for NO_3 and NH_4 concentrations, while CHIMERE-Vehkamaki increase the adequacy between observations and model results for SO_4 concentrations. For the same period we found that the Vekhamaki scheme gives a better agreement between modeled and measured total particle number concentration. We have shown that the nucleation scheme is not only influencing the number size distribution, but also the mass concentration and balance of main organic compounds in the aerosol, and hence we confirm the advice of caution (given by Zhang et al., 2010), in selecting a nucleation parameterization since most parameterization have not been tested for all ranges of ambient

conditions and the appropriateness of one parameterization cannot be determined solely based on whether it gives a good agreement with observations.

When we compare the modeled results with and without topography we see that the mountain acts as a barrier for the transport of polluted air. We also noticed that the new particle formation can occur in the free troposphere due to injection of boundary layer air caused by convective processes.

Summary and outlook

Aerosols play a key role in air quality (health aspects) and climate. In this thesis the atmospheric chemistry transport model CHIMERE was used to simulate the physical-chemical properties of aerosols at high altitude. Uncertainties in the meteorological parameters, the impact of orography on air flow and stability, the emissions of gas and aerosol species in the inventories, all contribute to the uncertainties in gas and aerosol modeling and require high priority in order to better estimate the gas and aerosol concentrations for scientific research and policy making.

The overall objectives of this thesis were to identify and quantify a few key uncertainties related to gas and aerosol modeling at PDD high altitude station. These are: (a) the impact of using two different emission inventories on gas and aerosol calculated concentrations; (b) the impact of using different nucleation scheme on new particle formation.

Because the evaluation of calculated meteorological parameters is a very important step in the validation of gas and aerosols modeling results, for the same period the input topographical data used by WRF meteorological model were changed using the SRTM data which have a horizontal resolution of 3s. The modeled results using the default topography at 30s provided by the WRF model and the SRTM topography at 3s slightly differ, but have no impact on the modeled values obtained using CHIMERE model.

The CHIMERE model was then run to simulate observations acquired during an intensive campaign from February 24 to March 8, 2009 when aerosol particle size and compositions measurements at PDD research station were available. The focus was the performance of the model to predict the aerosol chemical composition. Updating the emissions database to reflect modern mesoscale measurements refines the modeled aerosol concentrations. Using two emission inventories, EMEP and MACC, as described in Chapter 3, substantial differences in calculated gas-phase and primary particle concentrations were found for the BL stations. However, the differences at the high altitude station are not obvious, gaseous compounds have almost the same overestimation, except for SO_2 which is more accentuated when the MACC emission database is used. The CHIMERE model is able to reproduce most aerosol particle

concentrations (except organic carbon) at the PDD site and the results obtained using two different emissions database are quite similar (see Chapter 3).

During this thesis, different parameterizations of aerosol nucleation have been tested in the regional air quality model CHIMERE, leading to improvements in the prediction of aerosol number size distributions. It was also found that nucleation occurs both in boundary layer and free troposphere.

The nucleation mechanism was changed from the default binary homogeneous nucleation parameterization of Kulmala to the binary homogeneous nucleation parameterization of Vehkamaki and also to the nucleation parameterization which includes the organic compounds. Compared with the observed values, the total particles number concentrations are significantly overpredicted by all parameterizations, with the best predictions by Vehkamaki et al. (2002) and the worst predictions by Kulmala et al. (1998). The unmodified CHIMERE (Kulmala scheme) overpredicts total particle number concentrations by 2-3 orders of magnitude. The bias increases progressively for smaller particle sizes. Such a large variation is caused by differences in their theoretical bases, mathematical formulations, and different dependence on T, RH, as well as H_2SO_4 concentration. Despite the better performance of the Vehkamaki scheme, there are remaining issues such as accumulation mode that is too narrow and underpredicted in general, especially when rain has washed out aerosols from the atmosphere.

The changes of particles primary size distribution do not make a noticeable improvement, especially in those situations when the Vehkamaki scheme fails in reproducing the particle size distribution observed at PDD site. It is very likely that our understanding of aerosol pollution, especially in the ultrafine range, is not yet complete.

However, this study shows that after model improvements CHIMERE is able to reproduce number concentrations within one order of magnitude and size distributions with the appropriate major features.

This study raises a number of questions that might be answered by future research. One of them involves the introduction in the model of the aerosol number concentrations as model output because CHIMERE is a mass-based model, while nucleation is a number-based process.

Comparison between modeled values and observations indicates that during cloudy/rainy period, the high relative humidity contributes to the growth of pre-existing particles by condensation of water vapor, and wet scavenging by cloud and rain droplets of aerosol particles can occur. In the

absence of a condensable sink represented by preexisting accumulation mode particles, nucleation of new particles seems to be favored, especially using the Kulmala scheme. Climatology for different weather situation is necessary in order to prove if this affirmation is sustained for all seasons and to look which other meteorological factors can affect the new particle formation. A better treatment of the scavenging and wash-out processes in the model would improve the prediction of particles larger than 100 nm, and as a consequence also the occurrence and intensity of nucleation.

Furthermore simulating accurately particle number concentrations and size distributions remain a major challenge due to:

-the inaccuracies in primary particulate matter (PM) emissions;

-the large uncertainties in the parameterizations of homogeneous nucleation used in air quality models and the numerical algorithms of other important processes in determining PM number and mass concentrations such as coagulation and other gas-to-particle conversion processes (e.g., diffusion, condensation, heterogeneous reactions);

-the uncertainties associated with important model parameters such as initial PM size distribution;

-the lack of measurements of PM and gas precursors of secondary PM at representative sites of various ambient atmospheric meteorological and chemical conditions for model/parameterization validation.

References

Aksoyoglu, S., Keller, J., Barmpadimos, I., Oderbolz, D., Lanz, V. A., Prevot, A. S. H., and Baltensperger, U., 2011: Aerosol modelling in Europe with a focus on Switzerland during summer and winter episodes, Atmos. Chem. Phys., 11, 7355–7373, doi:10.5194/acp-11-7355-2011.

Andersen, H. V., M. F. Hovmand, P. Hummelshoj, and N. O. Jensen, 1999: Measurements of ammonia concentrations, fluxes and dry deposition velocities to a spruce forest 191 – 1995, Atmos. Environ., 33, 1367 – 1383.

Andreani-Aksoyoglu, S., Keller, J., and Prevot, A., 2007: Aerosol Modelling with CAMX4 and PM-CAMX: A Comparison Study, Air Pollution Modeling and Its Application XVII, 247–256.

Ayers, P.P., R.W. Gillett, J.L. Gras, 1980: On the vapor pressure of sulfuric acid, Geophys. Res. Lett. 7, 433–436.

Arakaki, T.,Kuroki,Y., Okada, K., Nakama,Y., Ikota,Y., and co-authors, 2006:. Chemical composition and photochemical formation of hydroxyl radicals in aqueous extracts of aerosol particles collected in Okinawa, Japan. Atmos. Envir. 40(25), 4764–4777

Arakawa, A., C. R. Mechso, and C. S. Konor, 1992: An isentropic vertical coordinate model: Design and application to atmospheric frontogenesis studies. Meteor. Atmos. Phys. 50, 31-45.

Arteta, J, 2005: Etude de l'impact du mecanisme chimique et des taux de photolyse "online" sur les simulation 3D d'episodes de pollution regionale. PhD thesis, Ecole Doctorale des Sciences Fondamentales, Universite Blaise-Pascal, Clermont-Ferrand.

Arya, S. P., 1999: Air Pollution Meteorology and Dispersion, Oxford Univ. Press, New York.

Asman, W. A., 1994: Emission and deposition of ammonia and ammonium, Nova Acta Leopold., 70, 263 – 297.

Asmi A., A. Wiedensohler, P. Laj, A.-M. Fjaeraa, K. Sellegri, W. Birmili, E. Weingartner, U. Baltensperger, V. Zdimal, N. Zikova, J.-P. Putaud, A. Marinoni, P. Tunved, H.-C. Hansson, M. Fiebig, N. Kivekäs, H. Lihavainen, E. Asmi, V. Ulevicius, P. P. Aalto, E. Swietlicki, A. Kristensson, N. Mihalopoulos, N. Kalivitis, I. Kalapov, G. Kiss, G. de Leeuw, B. Henzing, R. M. Harrison, D. Beddows, C. O'Dowd, S. G. Jennings, H. Flentje, K. Weinhold, F. Meinhardt, L. Ries, and M. Kulmala. (2011). Number size distributions and seasonality of submicron particles in Europe 2008–2009, Atmos. Chem. Phys., 11, 5505-5538.

Baek, B.H., Aneja, V.P., Tong Q., 2004: Chemical coupling between ammonia, acid gases, and fine particles, Environmental Pollution 129 (2004) 89–98

Bassett, M., Seinfeld, J. H., 1983: Atmospheric equilibrium model of sulfate and nitrate aerosols. Atmos. Environ., 17, 2237-2252.

Bassett, M., Seinfeld, J. H., 1984: Atmospheric equilibrium model of sulfate and nitrate aerosols-II. Particle size analysis. Atmos. Environ., 18, 1163-1170.

Battye, W., Aneja, V.P., Roelle, P., 2003: Evaluation and improvement of ammonia emissions inventories. Atmospheric Environment 37, 3873–3883.

Bellouin, N., O. Boucher, J. Haywood, M.S. Reddy, 2005: Global estimate of aerosol direct radiative forcing from satellite measurements, Nature 438, 1138–1141.

Benson, D. R., Li-Hao Young, , Shan-Hu Lee, , Campos, T. L., Rogers, D. C., and Jensen, J., 2008: The effects of airmass history on new particle formation in the free troposphere: case studies, Atmos. Chem. Phys., 8, 3015–3024

Berresheim, H., Elste, T., Tremmel, H. G., Allen, A. G., Hansson, H.-C., and co-authors, 2002: Gas-aerosol relationships of H2SO4, MSA and OH: observations in the coastal marine boundary layer at Mace Head, Ireland. J. Geophys. Res. 107(D19), 8100, doi:10.1029/2000JD000229.

Bernstein JA, Alexis N, Barnes C, Bernstein IL, Bernstein JA, Nel A, Peden D, Diaz-Sanchez D, Tarlo SM, Williams PB., 2004: Health effects of air pollution. J Allergy. Clin. Immunol. Nov;114(5):1116-23.

Bessagnet, B., Khvorostayanov, L., Menut, K., Monge, J. L., and Vautard, R., 2009: Documentation of the chemistry-transport model, CHIMERE. Institute Pierre Simon Laplace, INERIS, LISA, June 2009 edition, p. 158.

Bessagnet, B., Hodzic, A., Vautard, R., Beekmann, M., Cheinet, S., Honore, C., Liousse, C., and Rouil, L., 2004: Aerosol modeling with CHIMERE – preliminary evaluation at the continental scale, Atmos. Environ., 38, 2803–2817.

Bey, I., D. J. Jacob, R. M. Yantosca, J. A. Logan, B. D. Field, A. M. Fiore, Q. Li, H. Y. Liu, L. J. Mickley, and M. G. Schultz, 2001: Global modeling of tropospheric chemistry with assimilated meteorology: Model description and evaluation, J. Geophys. Res., 106(D19), 23,073–23,095, doi:10.1029/2001JD000807

Binkowski, F.S. and U. Shankar, 1995: The regional particulate matter model. 1: Model description and preliminary results, J. Geophys. Res., 100, 26191-26209

Blanchard, C.L., and G.M. Hidy, Effects of changes in sulfate, ammonia and nitric acid on particulate nitrate concentrations in the southeastern United States, J. Air & Waste Manage. Ass., 53, 283-290, 2003.

Briggs, G.A., 1965: A plume rise model compared with observations J.Air Poll. Control Association 15:433

Bond, T.C., D.G. Streets, K.F.Yarber, S.M. Nelson, J.-H. Woo, and Z. Klimont, 2004: A technologybased global inventory of black and organic carbon emissions from combustion, J. Geophys. Res., 109, D14203, doi:10.1029/2003JD003697

Bosanquet, C.H., 1936: The Spread of Smoke and Gas from Chimmneys. Trans. Faraday Soc. 32:1249

Boulon J., K. Sellegri, M. Hervo, D. Picard, J.-M. Pichon, P. Freville, and P. Laj, 2011: Investigation of nucleation events vertical extent: a long term study at two different altitude sites, Atmos. Chem. Phys., 11, 5625-5639

Byun D. W., A. Hanna, C. J. Coats, and D. Hwang, 1995: Models-3 Air Quality Model Prototype Science and Computational Concept Development. Trans. TR-24 Regional Photochemical Measurement and Modeling Studies, San Diego, CA, of Air & Waste Management Association, 197-212

Byun, D. W., 1999a: Dynamically consistent formulations in meteorological and air quality models for multiscale atmospheric applications: I.Governing equations in a generalized coordinate system. J. Atmos. Sci., 56, 3789-3807

Byun, D. W., 1999b: Fundamentals of one-atmosphere dynamics for multiscale air quality modeling, EPA/600/R-99/030

Clegg, S.L., P. Brimblecombe and A.S. Wexler, 1998a: A thermodynamic model of the system H^+ -NH_4^+ -Na^+ -SO_4^{2-} -NO_3^- -Cl^- -H_2O at 298.15 K, J. Phys. Chem., 102, 2155-2171.

Clegg, S.L., P. Brimblecombe and A.S. Wexler, 1998b: A thermodynamic model of the system H^+ -NH_4^+ -Na^+ -SO_4^{2-} -NO_3^- -Cl^- -H_2O at tropospheric temperatures, J. Phys. Chem., 102, 2137-2154.

Coffman, D.J., D.A. Hegg, 1995: A preliminary-study of the effect of ammonia on particle nucleation in the marine boundary-layer, J. Geophys. Res.-Atmospheres 100, 7147–7160.

Cooke, W.F., C. Liousse, H. Cachier, and J. Feichter, 1999: Construction of a 1º × 1º fossil fuel emission data set for carbonaceous aerosol and implementation and radiative impact in the ECHAM4 model, J. Geophys. Res., 104, 22,137-22,162.

Cooke, W.F., and J.J.N. Wilson, 1996: A global black carbon aerosol model, J. Geophys. Res., 101, 19,395-19,409.

Curtius, J., 2006: Nucleation of atmospheric aerosol particles, C. R. Physique 7 (2006) 1027–1045

Dávila I, Mullol J, Bartra J, Del Cuvillo A, Ferrer M, Jáuregui I, Montoro J, Sastre J, Valero A., 2007: Effect of pollutants upon patients with respiratory allergies. J. Investig. Allergol. Clin. Immunol.;17 Suppl 2:9-20.

de Reus,M., Strom, J., Hoor, P., Lelieveld, J., and Schiller, C., 1999: Particle production in the lowermost stratosphere by convective lifting of the tropopause, J. Geophys. Res., 104, 23935–23940,

Deardorff, J.W., and Willis, G.E., 1975: A parameterization of diffusion into the mixed layer J. Appl. Met 14:1451

Dusek, U., G.P. Frank, L. Hildebrandt, J. Curtius, J. Schneider, S. Walter, D. Chand, F. Drewnick, S. Hings, D. Jung, S. Borrmann, M.O. Andreae, 2006: Size matters more than chemistry for cloud-nucleating ability of aerosol particles, Science 312, 1375–1378.

Egan, B.A., Rao, K.S., and Bass, A., 1976: A three dimensional advective-diffusive model for long-range sulfate transport and transformation 7 th ITM, 697, Airlie House.

Eichkorn, S., K.H. Wohlfrom, F. Arnold, R. Busen: 2002: Massive positive and negative chemiions in the exhaust of an aircraft jet engine at ground-level: mass distribution measurements and implications for aerosol formation, Atmos. Environ. 36, 1821–1825.

Eliassen, A., and Saltbones, J., 1975: Decay and transformation rates of SO2 as estimated from mission data, trajectories and measured air concentrations Atm. Env. 9:425.

EPA, 1996, Air quality criteria for particulate matter, Research Triangle Park, NC: National Center for Environmental Assessment-RTP Office; report nos. EPA/600/P- 95/001aF-cF. 3v. 23

EPA, 1998, Particulate matter research need for human health risk assessment to support future reviews of the national ambient air quality standards for particulate matter. Research Triangle Park, NC: National Center for Environmental Assessment-RTP Office; report nos. EPA/600/R-97/123F

Eschenroeder, A.Q. and J.R. Martinez, 1970: Mathematical Modeling of Photochemical Smog, American Institute Aeronautics and Astronautics (Proceedings), Eight Aerospace Sciences Meeting, New York, Jan 19-21.

Faust. C.B, 1994: Photochemistry of Clouds, Fogs, and Aerosols**,** Environ. Sci. Technol., 1994, 28 (5), pp 216A–222A, DOI: 10.1021/es00054a001

Fisher, B.E.A., 1975: The long-range transport of sulfur dioxide, Atm.Env. 9,: 1063

Fitzgerald, J.W., W.A. Hoppel, and F. Gelbard, 1998: A one-dimensional sectional model to simulate multicomponent aerosol dynamics in the marine boundary layer. 1. Modal description, J. Geophys. Res., 103, 16085-16102.

Friedlander, S.K. and J.H. Seinfeld, 1969: A Dynamic Model of Photochemical Smog, Environ., Science Technol., 3, 1175

Fuchs, N.A, 1964: The Mechanics of Aerosols. Pergamon Press, Oxford

Fuchs, N.A., 1959: Evaporation and droplet growth in guseous media, Pergamon, Tarrytown, New York, pp 72

Fukuta, N., P.E. Wagner, 1992: Nucleation and Atmospheric Aerosol A. Deeak Publishing, Hampton, VA

Gaydos, T. M., Stanier, C. O., and Pandis, S. N., 2005: Modeling of in situ ultrafine atmospheric particle formation in the eastern United States, J. Geophys. Res., 110, D07S12, doi:10.1029/2004JD004683

Gillette, D., and R. Passi, 1988: Modeling dust emission caused by wind erosion, J. Geophys. Res., 3(D11), 14,233–14,242.

Guenther, A., Karl, T., Harley, P., Wiedinmyer, C., Palmer, P. I., and Geron, C., 2006: Estimates of global terrestrial isoprene emissions using MEGAN (Model of Emissions of Gases and Aerosols from Nature). Atmos. Chem. Phys., 6:3181–3210.

Hanson, D.R., E.R. Lovejoy, 2006: Measurement of the thermodynamics of the hydrated dimer and trimer of sulfuric acid, J. Phys. Chem. A 110, 9525–9528

Harrington, D. Y., and S. M. Kreidenweis, 1998: Simulation of Sulfate Aerosol Dynamics. I. Model Description. Atmos. Environ., 32, 1691-1700.

Heald, Colette L., Daniel J. Jacob, Rokjin J. Park, Lynn M. Russell, Barry J. Huebert, John H. Seinfeld, Hong Liao, and Rodney J. Weber, 2005: A large organic aerosol source in the free troposphere missing from current models. Geophysical Research Letters 32: L18809. doi:10.1029/2005GL023831

Hogstrom, U., 1964: An experimental study on atmospheric diffusion Tellus, 16:205.

Holzworth, G.C., 1967: Mixing depth, wind speed and air pollution potential for selected locations in the U.S.A., J.Appl.Met. 6:1039.

Hoppel, W. A., G. M. Frick, and J. W. Fitzgerald, 2002: Surface source function for sea-salt aerosol and aerosol dry deposition to the ocean surface, J. Geophys. Res., 107(D19), 4382, doi:10.1029/2001JD002014.

Isaksen, I.S.A., and Rohde, H., 1978: A two-dimensional model for the global distribution of gases and aerosol particles in the troposphere Rep. AC-47, Dep. of Meteor. Univ Stockholm, Sweden.

IPCC, 2007: Intergovernmental Panel on Climate Change. Fourth Assessment Report. Cambridge University Press, Cambridge, Section 2.2. 37 p.

Jacobson, M.Z., 1999: Studying the effects of calcium and magnesium on size-distributed nitrate and ammonium with EQUISOLV II, Atmos. Environ., 33, 3635-3649

Jacobson, M.Z., Tabazadeh, A., Turco, R.P., 1996: Simulating equilibrium within aerosols and nonequilibrium between gases and aerosols. J. Geophys. Res., 101, 9079-9091.

Jaecker-Voirol, A. and P. Mirabel, 1989: Heteromolecular Nucleation in the Sulfuric Acid-Water System. Atmos. Environ. 23:2033-2057.

Johnson, W.B., 1980: Interregional exchange of air pollution: model types and applications 10 th ITM, 3, Amsterdam

Jung, J, Adams, P. J., and Pandis, S. N., 2006: Simulating the size distribution and chemical composition of ultrafine particles during nucleation events, Atmos. Environ., 40, 2248–2259

Kazil, J., Lovejoy, E.R., 2004: Tropospheric ionization and aerosol production: A model study, J. Geophys. Res.—Atmospheres 109, D19206, doi:10.1029/2004JD004852

Kerminen, V.M., 1993: The effects of particle interaction forces on Brownian coagulation in tropospheric conditions. Report Series in Aerosol Science, 22, University of Helsinki, Finland.

Kim, Y.P., Seinfeld J.H., Saxena, P., 1993: Atmopsheric gas-aerosol equilibrium I. Thermodynamic model. Aerosol Sci. Technol., 19, 157-181.

Kim, Y.P. and J.H. Seinfeld, 1995: Atmospheric gas-aerosol equilibrium III: thermo-dynamics of crustal elements Ca^{2+}, K^{+}, and Mg^{2+}, Aerosol Sci. Technol., 22, 93-110.

Klug, W., 1968: Diffusion in the atmospheric surface layer: comparison of similarity theory with observations Quart. J.R. Met.Soc. 94:555.

P. Korhonen, M. Kulmala, A. Laaksonen, Y. Viisanen, R. McGraw, J.H. Seinfeld, 1999: Ternary nucleation of H2SO4, NH3, and H2O in the atmosphere, J. Geophys. Res.—Atmospheres 104, 26349–26353

Kuenen, J., van der Gon, H.D., Visschedijk, A., van der Brugh, H., van Gijllswijk, R., 2011: MACC European emission inventory for the years 2003-2007, TNO report, TNO-060-UT-2011-00588.

Kulmala, M.; Kerminen, V. M.; Laaksonen, A., 1995: Simulations on the effect of sulphuric acid formation on atmospheric aerosol concentrations. Atmos. Environ., 29, 377–382.

Kulmala M., A. Laaksonen, and L. Pirjola, 1998: Parameterizations for sulphuric acid/water nucleation rates, J. Geophys. Res., 103, 8301-8308

Kulmala M., 2003: How Particles Nucleate and Grow. Science, 302 (2003), pp. 1000–1001 DOI:10.1126/science.1090848

Kulmala, M.,Wagner, P. E., 1996: Nucleation and Atmospheric Aerosol Elsevier Science, Oxford, UK

Kulmala, M., H. Vehkamaki, T. Petaja, M. Dal Maso, A. Lauri, V.-M. Kerminen, W. Birmili, P.H. McMurry, 2004: Formation and growth rates of ultrafine atmospheric particles: A review of observations J. Aerosol Sci., 35 (2), pp. 143–176

Laakso, L., J.M. Makela, L. Pirjola, M. Kulmala, 2002: Model studies on ion-induced nucleation in the atmosphere, J. Geophys. Res.-Atmospheres 107, 4427, doi:10.1029/2002JD002140.

Lee, S.H., et al., 2004: New particle formation observed in the tropical/subtropical cirrus clouds, J. Geophys. Res.—Atmospheres 109, D20209, doi:10.1029/2004JD005033.

Li, G., Lei, W., Zavala, M., Volkamer, R., Dusanter, S., Stevens, P., and Molina, L. T., 2010: Impacts of HONO sources on the photochemistry in Mexico City during the MCMA-2006/MILAGO Campaign, Atmos. Chem. Phys., 10, 6551–6567, doi:10.5194/acp-10-6551-2010.

Liepert, B.G., and I. Tegen, 2002: Multidecadal solar radiation trends in the United States and Germany and direct tropospheric aerosol forcing. J. Geophys. Res., 107, doi:10.1029/2001JD000760.

Liousse, C., J.E. Penner, C. Chuang, J.J. Walton, H. Eddleman, and H. Cachier, 1996: A global threedimensional model study of carbonaceous aerosols, J. Geophys. Res., 101, 19,411-19,432

Liu, M.K. and J.H. Seinfeld, 1974: On the Validity of Grid and Trajectory Models of Urban Air Pollution, Atmos. Environ., Vol. 9, pp. 555-574.

Lyubovtseva, Y. S., Sogacheva, L., Dal Maso, M., Bonn, B., Keronen, P., and Kulmala, M., 2005: Seasonal variations of trace gases, meteorological parameters, and formation of aerosols in boreal forest, Bor. Environ. Res., 10, 493–510

Lovejoy, E.R., Curtius, J., Froyd, K.D., 2004: Atmospheric ion-induced nucleation of sulfuric acid and water, J. Geophys. Res.-Atmospheres 109, D08204, doi:10.1029/2003JD004460

Makkonen, R., Asmi, A., Korhonen, H., Kokkola, H., Jarvenoja, S.,Raisanen, P., Lehtinen, K. E. J., Laaksonen, A., Kerminen, V.-M., Jarvinen, H., Lohmann, U., Bennartz, R., Feichter, J., and Kulmala, M., 2009: Sensitivity of aerosol concentrations and cloud properties to nucleation and secondary organic distribution in ECHAM5-HAM global circulation model, Atmos. Chem. Phys., 9, 1747–1766, doi:10.5194/acp-9-1747-2009

Marti, J.J., A. Jefferson, X.P. Cai, C. Richert, P.H. McMurry, F. Eisele, 1997: H_2SO_4 vapor pressure of sulfuric acid and ammonium sulfate solutions, J. Geophys. Res.—Atmospheres 102, 3725–3735.

Marticorena, B., and G. Bergametti, 1995: Modeling the atmospheric dust cycle: 1-design of a soil derived dust production scheme, J. Geophys. Res., 100, 16,415–16,430

Mazurek, M., M. C. Masonjones, H. D. Masonjones, L. G. Salmon, G. R. Cass, K. A. Hallock, and M. Leach, 1997: Visibility-reducing organic aerosols in the vicinity of Grand Canyon National Park: Properties observed by high-resolution gas chromatography. J. Geophys. Res., 102, 3779-3793.

McMurry, P.H., and S.K. Friedlander, 1979: New particle formation in the presence of an aerosol, Atmos. Environ., 13, 1635-1651.

McMurry, P. H., H. Takano, and G. R. Anderson, 1983: Study of the ammonia (gas) – sulphuric acid (aerosol) reaction rate, Environ. Sci. Technol., 17, 347 – 352.

Meng, Z., Dabdub, H., Seinfeld, J.H, 1997: Chemical Coupling between Atmospheric Ozone and Particulate Matter; Science 1997, 277, 116-119

Meng, Z., J.H. Seinfeld, P. Saxena and Y.P. Kim, 1995: Atmospheric gas-aerosol equilibrium, IV: thermodynamics of carbonates, Aerosol Sci. Technol., 23, 131-154

Merikanto, J., Spracklen, D. V., Mann, G. W., Pickering, S. J., and Carslaw, K. S., 2009: Impact of nucleation on global CCN, Atmos. Chem. Phys., 9, 8601–8616, doi:10.5194/acp-9-8601-2009

Metzger, A., Verheggen, B., Dommen, J., Duplissy, J., Prevot, A.S.H., Weingartner, E., Riipinen, I., Kulmala, M., Spracklen, Carslaw, K.S., Baltensperger, U., 2010: Evidence for the role of organics

in aerosol particle particle formation under atmospheric conditions, Proc. Nat. Acad. Sci., 107, pp. 6646-6651, doi:10.1073/pnas.0911330107

Middleton, P., Stockwell, W. R., and Carter, W. P., 1990: Agregation and analysis of volatile organic compound emissions for regional modelling. Atmos. Environ., 24:1107–1133.

M.S. Modgil, S. Kumar, S.N. Tripathi, E.R. Lovejoy, 2005: A parameterization of ion-induced nucleation of sulphuric acid and water for atmospheric conditions, J. Geophys. Res.—Atmospheres 110, D19205, doi:10.1029/12004JD005475.

Monahan, E. C., 1986: In The Role of Air-Sea Exchange in Geochemical Cycling, chapter The ocean as a source of atmospheric particles, pages 129–163. Kluwer Academic Publishers, Dordrecht, Holland.

Moore, D.J., 1967: Physical aspects of plume models Atm.Env. 1:411.

Napari, I., M. Kulmala, and H. Vehkamaki, 2002a: Ternary nucleation of inorganic acids, ammonia, and water. J. Chem. Phys., 117, 8418-8425.

Napari, I., M, Noppel, H. Vehkamaki, and M. Kulmala, 2002b: Parameterization of ternary nucleation rates for H2SO4-NH3-H2O vapors. J. Geophys. Res., 107, 4381.

Nenes A., Pilinis C., Pandis S.N., 1998: ISORROPIA: A new thermodynamic model for inorganic multicomponent atmospheric aerosols. Aquatic Geochem., 4, 123-152.

Nenes, A., C. Pilinis and S.N. Pandis, 1999: Continued development and testing of a new thermodynamic aerosol module for urban and regional air quality models, Atmos. Environ., 33, 1553-1560.

Nilsson, E.D., U. Rannik, G. Buzorius, M. Kulmala, C. O'Dowd, 2001: Effects of the continental boundary layer evolution, convection, turbulence and entrainment on aerosol formation, Tellus, 53B, pp. 441–461

Niyogi, D., et al., 2004: Direct observations of the effects of aerosol loading on net ecosystem CO_2 exchanges over different landscapes. Geophys. Res. Lett., 31, L20506, doi:10.1029/2004GL020915.

Noppel, M. H. Vehkamaki, M. Kulmala, 2002: An improved model for hydrate formation in sulfuric acid–water nucleation, J. Chem. Phys. 116, 218–228.

Pandis, S.N., L.M. Russell, and J.H. Seinfeld, 1994: The relationship between DMS flux and CCN concentration in remote marine regions, J. Geophys. Res., 99, 16945-16957

Penner, J.E., H. Eddleman, and T. Novakov., 1993: Towards the development of a global inventory for black carbon emissions, Atmos. Environ., 27, 1277-1295

Petaja, T., R. L. Mauldin, E. Kosciuch, J. McGrath, T. Nieminen, P. Paasonen, M. Boy, A. Adamov, T. Kotiaho, and M. Kulmala, 2009: Sulfuric acid and OH concentrations in a boreal forest site, Atmos. Chem. Phys., 9, 7435–7448, 2009

Peters, L.K., and Jouvanis, A.A., 1979: Numerical simulation of the transport and chemistry of CH4 and CO in the troposphere, Atm.Env. 13:1443.

Pierce, J. R. and Adams, P. J., 2006: Global evaluation of CCN formation by direct emission of sea salt and growth of ultrafine sea salt, J. Geophys. Res.-Atmos., 111, D06203, doi:10.1029/2005JD006186

Pinder, R., A. Gilliland, R. L. Dennis, 2006: The impact of winter NH3 emission reductions on inorganic particulate matter under present and future regulated conditions. Presented at Workshop on Agricultural Air Quality: State of the Science, Potomac, MD, June 05 - 08, 2006.

Pirjola, L. K.E.J. Lehtinen, H.C. Hansson, M. Kulmala, 2004: How important is nucleation in regional/global modeling, Geophys. Res. Lett. 31, L12109, doi:10.1029/2004GL019525.

Pirjola, L., M. Kulmala, M. Wilck, A. Bischoff, F. Stratmann, E. Otto, 1999: Formation of sulphuric acid aerosols and cloud condensation nuclei: An expression for significant nucleation and model comparison, J. Aerosol Sci. 30, 1079–1094.

Pio, C. A., C. A. Alves, and A. C. Duarte, 2001: Identification, abundance and origin of atmospheric organic particulate matter in a Portuguese rural area. Atmos. Env., 35, 1365-1375.

Plinis, C. and J.H. Seinfeld, 1987: Continued development of a general equilibrium model for inorganic multicomponent atmopsheric aerosols, Atmos Environ., 32, 2453-2466

Poschl, U., 2005: Atmospheric Aerosols: Composition, Transformation, Climate and Health Effects. Angew. Chem. Int. Ed., 44, 7520 – 7540.

Putaud, J., F. Raes, R. Van Dingenen, E. Brüggemann, M. Facchini, S. Decesari, S. Fuzzi, R. Gehrig, C. Hüglin, P. Laj, G. Lorbeer, W. Maenhaut, N. Mihalopoulos, K. Müller, X. Querol, S. Rodriguez, J. Schneider, G. Spindler, H. ten Brink, K. Tørseth, and A. Wiedensohler, 2004: An European aerosol phenomenology-2: Chemical characteristics of particulate matter at kerbside, urban, rural and background sites in Europe. Atmos. Environ. 38, 2579–2595.

Reddington, C. L., Carslaw, K. S., Spracklen, D. V., Frontoso, M. G., Collins, L., Merikanto, J., Minikin, A., Hamburger, T., Coe, H., Kulmala, M., Aalto, P., Flentje, H., Plass-Dülmer, C., Birmili, W., Wiedensohler, A., Wehner, B., Tuch, T., Sonntag, A., O'Dowd, C. D., Jennings, S. G., Dupuy, R., Baltensperger, U., Weingartner, E., Hansson, H.-C., Tunved, P., Laj, P., Sellegri, K., Boulon, J., Putaud, J.-P., Gruening, C., Swietlicki, E., Roldin, P., Henzing, J. S., Moerman, M., Mihalopoulos, N., Kouvarakis, G., Ždímal, V., Zíková, N., Marinoni, A., Bonasoni, P., and Duchi, R., 2011: Primary versus secondary contributions to particle number concentrations in the European boundary layer, Atmos. Chem. Phys., 11, 12007-12036, doi:10.5194/acp-11-12007-2011

Remer, L. A., Chin, M., DeCola, P., Feingold, G., Halthore, R., Kahn, R.A., Quinn, P.K., Rind, D., Schwartz, S.E., Streets, D.G., Yu, H., 2009: Atmospheric Aerosol Properties and Climate Impacts, U.S. Climate Change Science Program Synthesis and Assessment, Product 2.3

Reynolds, S., Roth, P., and Seinfeld, J., 1973: Mathematical modeling of photochemical air pollution Atm.Env. 7

Rohde, H., 1972: A study of the sulfur budget for the atmosphere over northern Europe Tellus, 4:128.

Rohde, H., 1974: Some aspects of the use of air trajectories for the computation of large scale dispersion and fallout patterns Adv. in Geophysics 18B: 95, academic press.

Roth H., W. Jiang, D. Yin and E. Giroux, 2003: CMAQ nucleation algorithms and their impact on PM modeling results in the lower Fraser valley, presented at the 2003 CMAS Models-3 User's Workshop: One Atmosphere, One Community, One Modeling System: Models-3. Research Triangle Park, NC, October 27-29

Saxena, P., Hudischewsky, A.B., Seigneur, C., Seinfeld, J.H., 1986: A comparative study of equilibrium approaches to the chemical characterization of secondary aerosols. Atmos. Environ., 20, 1471-1483

Seinfeld, J. H., and S. Pandis, 1998: Atmospheric Chemistry and Physics from Air Pollution to Climate Change, John Wileyand Sons, New York, pp 1326.

Seinfeld, J. H., 1986: Atmospheric Chemistry and Physics of Air Pollution, John Wiley, New York.

Shao, Y., 2004: Simplification of dust emission scheme and comparison with data, J. Geophys.Res. 109, D10202, doi:10.1029/2003JD004372

Shao Y., M.R. Raupach and J. F. Leys, 1996: A model for predicting Aeolian sand drift and dust entrainment on scales from paddock to region, Aust. J. Soil Res. 34, 309-342

Shiraiwa M, Selzle K, Pöschl U, 2012: Hazardous components and health effects of atmospheric aerosol particles: reactive oxygen species, soot, polycyclic aromatic compounds and allergenic proteins. Free Radic Res. 2012 Aug;46(8):927-39. Epub 2012 Apr 23.

Shir, C.C. and L.J. Shieh, 1974: A generalized urban air pollution model and its application to the study of SO2-distribution in the St. Louis Metropolitan area, J. Appl. Met. 19, 185-204

Skamarock, W. C., Klemp, J. B., Dudhia, J., Gill, D.O., Barker, D. M., Duda, M.G., Huang X.Y., Wang, W., Powers, J.G., 2008: A Description of the Advanced Research WRF Version 3, NCAR/TN–475+STR, NCAR TECHNICAL NOTE

Sklarew, R.C. et al., 1971: A particle-in-cell method for numerical solution of the atmospheric diffusion equation and application to air pollution problems; Systems, Science and Software, Ca-Reg 35R-844, Vol I.

Society, E. I., 1994: Generation of European Emission Data for Episodes (GENEMIS) project, EUROTRAC annual report 1993, part 5. Technical report, EUROTRAC, Garmish-Partenkirchen, Germany.

Sogacheva, L., Saukkonen, L., Nilsson, E. D., Dal Maso, M., Schultz, D. M., De Leeuw, G., and Kulmala, M., 2008: New aerosol particle formation in different synoptic situations at Hyytiala, Southern Finland, Tellus, 60(4), 485–494

Solomon, S., Qin, D., Manning, M., Alley, R. B., Berntsen, T., Bindo_, N. L., Chen, Z., Chidthaisong, A., Gregory, J. M., Hegerl, G. C., Heimann, M., Hewitson, B., Hoskins, B. J., Joos, F., Jouzel, J., Kattsov, V., LohmannU., Matsuno, T., Molina, M., Nicholls, N., Overpeck, J., Raga, G., Ramaswamy, V., Ren, J., Rusticucci, M., Somerville, R., Stocker, T. F., Whetton, P., Wood, R. A., and Wratt, D., 2007: Technical Summary. In: Climate Change 2007: The Physical Science Basis. Contribution of Working Group I to the Fourth Assessment Report of the Intergovernmental Panel on Climate Change, Cambridge University Press, Cambridge, UK and New York, USA

Stern, D.I., 2005: Global sulfur emissions from 1850 to 2000, Chemosphere 58, 163–175.

Spracklen, D. V., Carslaw, K. S., Kulmala, M., Kerminen, V.-M., Mann, G. W., and Sihto, S.-L., 2006: The contribution of boundary layer nucleation events to total particle concentrations on regional and global scales, Atmos. Chem. Phys., 6, 5631–5648

Spracklen, D. V., Carslaw, K. S., Kulmala, M., Kerminen, V.-M., Sihto, S.-L., Riipinen, I., Merikanto, J., Mann, G. W., Chipperfield,M. P., Wiedensohler, A., Birmili, W., and Lihavainen, H., 2008: Contribution of particle formation to global cloud condensation nuclei concentrations, Geophys. Res. Lett., 35, L06808, doi:10.1029/2007GL033038

Stelson, A.W. Seinfeld, J.H., 1982: Relative Humidity and pH Dependence of the Vapor Pressure of Ammonium Nitrate-Nitric Acid and Solutions at 25 Degree Celsius; Atmos. Environ. 1982, 16, 993-1000

Stern, R., Builtjes, P., Schaap, M., Timmermans, R., Vautard, R., Hodzic, A., Memmesheimer, M., Feldmann, H., Renner, E., Wolke, R., Kerschbaumer, A., 2008: A model inter-comparison study focussing on episodes with elevated PM10 concentrations. Atmos. Environ. doi:10.1016/j.atmosenv.2008.01. 068.

Sutton O.G., 1932: A theory of Eddy Diffusion in the Atmosphere. Proc. Roy. Soc. A, 135:143.

Taylor, G.I., 1915: Eddy motion in the atmosphere Phil. Transactions of the Royal Soc. of London.Series A, 215:1.

Taylor, G.I., 1921: Diffusion by continuous movements proc. London Math. soc. 20:196.

Textor, C., et al., 2006: Analysis and quantification of the diversities of aerosol life cycles within AeroCom, Atmos. Chem. Phys., 6, 1777–1813, doi:10.5194/acp-6-1777-2006.

Tsapakis, M., E. Lagoudaki, E. G. Stephanou, I. G. Kavouras, P. Koutrakis, P. Oyola, and D. von Baer, 2002: The composition and sources of PM2.5 organic aerosol in two urban areas of Chile. Atmos. Env., 36, 3851-3863.

Turco, R.P., O.B. Toon, R.C. Whitten, J.B. Pollack, and P. Hamill, 1983: The global cycle of particulate elemental carbon: a theoretical assessment, in Precipitation Scavenging, Dry Deposition, and Resuspension, ed. H.R. Pruppacher et al., pp. 1337-1351, Elsevier Science, New York

Turner, D.B., 1964: A diffusion model for an urban area J.Appl. Met. 3:83.

Twohy, C. H., Clement, C. F., Gandrud, B. W., Weinheimer, A. J., Campos, T. L., Baumgardner, D., Brune, W. H., Faloona, I., Sachse, G. W., Vay, S. A., and Tan, D., 2002: Deep convection as a source of new particles in the midlatitude upper troposphere, J. Geophys. Res., 107, 4560, doi:10.1029/2001JD000323

Uno, I., H. Amano, S. Emori, K. Kinoshita, I. Matsui, and N. Sugimoto, 2001: Trans-Pacific yellow sand transport observed in April 1998: A numerical simulation, J. Geophys. Res., 106(D16), 18,331-18,334

Vehkamaki, H., M. Kulmala, I. Napari, K.E.J. Lehtinen, C. Timmreck, M. Noppel and A. Laaksonen, 2002: An improved parameterization for sulfuric acid-water nucleation rates for tropospheric and stratospheric conditions, J. Geophys. Res., 107, 4622, doi:10.1029/2002JD002184.

Venzac, H., Sellegri, K., Villani, P., Picard, D., and Laj, P., 2009: Seasonal variation of aerosol size distributions in the free troposphere and residual layer at the puy de Dome station, France, Atmos. Chem. Phys., 9, 1465-1478, doi:10.5194/acp-9-1465-2009

Vestreng, V., 2003: EMEP/MSC-W Technical report. Review and Revision. Emission data reported to CLRTAP. MSC-W Status Report 2003. EMEP/MSC-W Note 1/2003. ISSN 0804-2446.

Vignatti, E., 1999: Modelling Interactions between Aerosols and Gaseous Compounds in the Polluted Marine Atmosphere, PhD thesis, University of Copenhagen, Faculty of Science, Department of Geophysics

Vogel, B., F. Fiedler, and H. Vogel, 1995: Influence of topography and biogenic volatile organic compounds emission in the state of Baden-Wurttemberg on ozone concentrations during episodes of high air temperatures. J. Geophys. Res., 100, 22,907-22, 928.

Wang, M. and Penner, J. E., 2009: Aerosol indirect forcing in a global model with particle nucleation, Atmos. Chem. Phys., 9, 239–260

Warneck, P., Chemistry of the Natural Atmosphere, Academic, San Diego, Calif., 1988.

Warren, D. R., 1986: Nucleation and growth of aerosols. Thesis of the California Institute of Technology. Pasadena.

R.J.Weber, J.J. Marti, P.H. McMurry, F.L. Eisele, D.J. Tanner, A. Jefferson, 1996: Measured atmospheric new particle formation rates: Implications for nucleation mechanisms, Chem. Engrg. Commun. 151, 53–64.

Wexler A. S. and J. H. Seinfeld, 1990: The distribution of ammonium salts among a size and composition dispersed aerosol. Atmos. Environ. 24A:1231-1246.

Wexler, A.S. and Seinfeld, J.H., 1991: Second-generation inorganic aerosol model. Atmos. Environ. 12, 2731-2748

Wexler, A. S., F. W. Lurmann, and J. H. Seinfeld, 1994: Modeling Urban and Regional Aerosols. I. Model Development. Atmos. Environ. 28, 531-546.

World Health Organization (WHO) Regional Office for Europe, Copenhagen, 2000: Air Quality Guidelines for Europe, WHO Regional Publications, European Series, No. 91, Second Edition, ISBN 92 890 1358 3

Whitby, K. T. and B. Cantrell, 1976: Fine particles. International Conference of Environmental Sensing and Assessment, Las Vegas, NV, Institute of Electrical and Electronic Engineers.

Whitby, E. R. and P. H. McMurry, 1997: Modal aerosol dynamics modeling. Aerosol Sci. Technol. 27, 673–688.

Yamartino, R. J., 1977: A new Method for computing pollutant concentrations in the presence of limited vertical mixing. APCA Note Book 27(5):467

Young, L.-H., Benson, D. R., Montanaro, W. M., Lee, S.-H., Pan, L. L., Rogers, D. C., Jensen, J., Stith, J. L., Davis, C. A., Campos, T. L., Bowman, K. P., Cooper, W. A., and Lait, L. R., 2007: Enhanced new particle formation observed in the Northern Hemisphere midlatitude tropopause region, J. Geophys. Res., 112, D10218, doi:10.1029/2006JD008109

Yu, F.Q., 2006: Binary H_2SO_4–H_2O homogeneous nucleation based on kinetic quasi-unary nucleation model: Look-up tables, J. Geophys. Res.—Atmospheres 111, D04201, doi:10.1029/2005JD006358.

Yu, F.Q., 2006: Effect of ammonia on new particle formation: A kinetic H2SO4–H2O–NH3 nucleation model constrained by laboratory measurements, J. Geophys. Res.—Atmospheres 111, D01204, doi:10.1029/2005JD005968.

Yu, F.Q., Turco, R.P., 2001: From molecular clusters to nanoparticles: Role of ambient ionization in tropospheric aerosol formation, J. Geophys. Res.—Atmospheres 106, 4797–4814.

Yu, H. et al., 2006: A review of measurement-based assessments of the aerosol direct radiative effect and forcing, Atmos. Chem. Phys., 613–666.

Zhang, Y., R. Easter, S. Ghan, and H. Abdul-Razzak, 2002: Impact of aerosol size representations on modeling aerosol-cloud interactions. J. Geophys. Res. 107, doi:1029/2001JD001549.

Zhang, Y., C. Seigneur, J. H. Seinfeld, M. Z. Jacobson, and F. Binkowski, 1999: Simulation of aerosol dynamics: A comparative review of algorithms used in air quality models. Aerosol Sci. Technol. 31, 487–514.

Zhang, R., I. Suh, J. Zhao, D. Zhang, E. C. Fortner, X. Tie, L. T. Molina, and M. J. Molina, 2004: Atmospheric new particle formation enhanced by organic acids, Science, 304, 1487–1490.

Zhang, Y, P. Liu, X.-H. Liu, M.Z. Jacobson, P. McMurry, F. Yu, S.-C. Yu, and K. Schere, 2010: A Comparative Study of Homogeneous Nucleation Parameterizations, Part II. 3-D Model Application and Evaluation, J. Geophys. Res., 115, D20213, doi:10.1029/2010JD014151

Zhang, Y., P. Liu, B. Pun, and C. Seigneur, 2006: A comprehensive performance evaluation of MM5-CMAQ for summer 1999 southern oxidants study episode, Part III. Diagnostic and mechanistic evaluations, Atmos. Environ., 40, 4856–4873, doi:10.1016/j.atmosenv.2005.12.046.

Zimmermann, P.H., 1988: Moguntia: a handy global tracer model 17 th ITM. 593, Cambridge